Radboud University Nijmegen

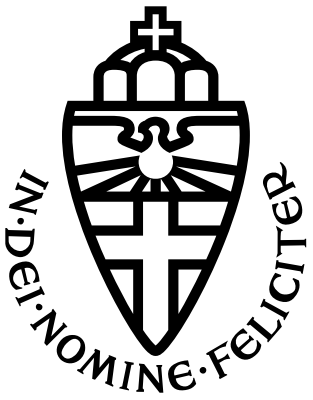

Faculty of Science

Tidal resonances in extreme mass ratio inspirals

A framework for studying stationary and dynamic tidal resonances

Thesis MSc Physics & Astronomy

Author:
Bart Peters

Supervisor:
dr. Béatrice Bonga

Second reader:
prof. dr. Gijs Nelemans

July 2023

Abstract

We live in exciting times for gravitational wave astronomy. Since the LIGO detectors first observed a gravitational wave signal in 2015, the ground-based detectors of the LIGO-VIRGO-Kagra collaboration have been very successful in observing gravitational waves originating from the merging of neutron stars and black holes. A new era will emerge when the Laser Interferometer Space Antenna (LISA) will become operational in about a decade from now. LISA will be able to detect gravitational wave signals in the low frequency ($\sim$ mHz) range, which makes it well-suited for probing the dynamics of binaries in the strong gravitational regime. One of LISA's prime target sources is extreme mass ratio inspirals, which are binaries characterized by their extremely small mass ratio. Stellar massive objects living in the vicinity of these inspirals may impact the orbit of the binary's smaller mass, thereby leaving an imprint on the gravitational waves emitted by the binary system. If such a scenario arises, we say that the orbit has encountered a tidal resonance. When LISA provides us with data of an extreme mass ratio inspiral, wrong parameters of the system may be inferred if we do not model for these resonances correctly. In the worst case scenario, we may even conclude that the theory of general relativity is wrong. However, if we can identify tidal resonances from LISA's data, we may learn about the tidal environment near supermassive black holes. As this is very difficult to achieve from electromagnetic observations, tidal resonances have the potential to serve as a new tool in astronomy. In this thesis we will set up a semi-analytical framework to study tidal resonance effects in extreme mass ratio inspirals. We will discuss a stationary and a dynamic model, where the tidal perturber is taken to be respectively stationary or dynamic across a tidal resonance. We will subsequently calculate the size of the tidally induced 'jumps' in the orbital constants of motion using both models. These jump sizes can then serve as input for the gravitational waveform modeling community, in order to construct accurate waveform templates for LISA.

Acknowledgements

At first, I would like to thank my supervisor Béatrice Bonga for her enthusiasm and guidance during my internship. Our conversations were never boring, and I could always give my own input on this project. This really made last year a lot of fun for me. Secondly, I would like to thank Priti Gupta for explaining the methods used in previous research on tidal resonances by Béatrice and her. We had very fruitful discussions, and you were always able to answer my questions. Thirdly, I would like to thank Gijs Nelemans for agreeing to be the second corrector of my thesis. I hope that you will enjoy reading this work. Lastly, I would like to thank my family, friends and Dominique for their full support throughout the year.

Contents

1 Introduction

1.1 Gravitational wave astronomy

For several hundreds of years we have only been able to study the Universe through measurements of electromagnetic radiation. This drastically changed in September 2015, when the LIGO observatories detected the first direct signal of a gravitational wave (GW) [2]. GWs are ripples through the fabric of spacetime and were first predicted by Albert Einstein's theory of general relativity (GR), which he published in 1915. Having withstood all tests so far, GR is the most accepted theory of gravity to date. GWs are caused by gravitationally intense events like the explosion of stars and the merging of black holes (BHs). They encode details of these violent events and therefore serve as a tool to explore the Universe in regimes where the gravitational field is strong and dynamic. In the years following the first GW detection, the ground based detectors of the LIGO-VIRGO-Kagra collaboration observed about a hundred subsequent GW signals in the frequency range between 10 Hz and 1 kHz [3]. This frequency band will be expanded with the next generation of detectors, including the ground-based Einstein telescope and the space-borne Taiji, TianQuin and Laser Interferometer Space Antenna (LISA). LISA will become operational in the early 2030s and will be able to detect GWs in the mHz frequency range [8].

Information can be extracted from a GW signal by matching it with a waveform template. These templates predict the functional form of a GW's strain for the relevant parameter space of the system radiating the waves. Environmental effects on these systems may invoke changes in the gravitational waveform. Matched filtering techniques, which are extensively used in GW observations, heavily depend on the GW's phase. Therefore, accurate waveform modeling is necessary. Because LISA will have a higher sensitivity compared to the ground-based detectors, it is expected that the space-borne interferometer will detect several hundreds to thousands overlapping GW signals at the same time [4]. In order to distinguish these signals, strong theoretical input for the waveform models is needed. In this work we will focus on tidal effects exerted on extreme mass ratio inspirals (EMRIs), which is one of LISA's main targets.

1.2 Extreme mass ratio inspirals

An EMRI is a binary system where a stellar-mass object of mass $\mu \sim 1 - 100 M_\odot$ spirals into a supermassive BH of mass $10^5 - 10^7 M_\odot$. This inspiral causes both masses to dissipate energy through the emission of GWs [26]. EMRIs can spend $10^4 - 10^5$ cycles in LISA's observational band, which corresponds to several years. Therefore they accommodate a unique possibility to probe the spacetimes of massive BHs and can serve as a tool to perform high precision tests of GR. It is of great importance that we accurately model for the EMRI's evolution, since it is expected that LISA can detect about $1 - 1000$ EMRI signals during a four-year mission [6]. We can then infer the correct parameters of the EMRI's spacetime, and we can perform these high-precision tests [53].

An EMRI is characterized by its small mass ratio $\eta = \frac{\mu}{M} \sim 10^{-4} - 10^{-7}$, which allows for a perturbative treatment of the EMRI's dynamics. To lowest order, the secondary mass is well-approximated by a test particle on a bound orbit around the central BH. Consequently, the orbital motion can be formulated in terms of the geodesics equations in the Kerr spacetime. Such relativistic orbits possess three orbital frequencies, being the radial ω_r, polar ω_θ and azimuthal ω_ϕ frequencies [10]. At next-to-lowest order, the gravitational field of the secondary mass is taken into account, which results in a leading perturbative term in the expansion known as the 'self-force'. This force consists of a dissipative and a conservative piece. The dissipative piece drives the inspiral, causing the dissipation of energy through the 'radiation reaction'. This reaction is most often modeled for in the so-called 'adiabatic approximation' [27], which only comprises the prolonged dynamics of the self-force. The conservative piece of the self-force can cause shifts in the orbital

frequencies. These shifts occur when a so-called 'self-force resonance' is encountered. This happens when the polar and azimuthal frequencies become commensurate, such that $n\omega_r + k\omega_\theta = 0$ for some integers n and k [17]. The EMRI's orbital evolution is altered after a self-force resonance is crossed. This changes the amount of energy dissipated by the binary system, which ultimately impacts the EMRI's parameter estimation through the detection of its GWs [7, 31].

1.3 Tidal resonances

In general, EMRIs are not isolated systems. They can be accompanied by other nearby astrophysical objects like stars or smaller BHs. These objects exert a tidal force on the EMRI, which changes the EMRI's orbital dynamics. At the same time, this effect can be neglected through most of the inspiral, as it is of a periodic nature. Therefore, the net tidal force will evaluate to zero when averaged over many orbits. This is not true, however, when a so-called 'tidal resonance' occurs in the EMRI's inspiral [22]. During a tidal resonance, the gravitational potential of a tidal perturber can effect the orbit of the EMRI's smaller mass by causing a 'jump' in the orbital constants of motion. An example of tidally induced jumps in an orbit's axial angular momentum (L_z) and Carter constant (Q) is displayed in Fig. 1. The orbital evolution is altered after a tidal resonance is crossed, which in turn modifies the GWs radiated by the EMRI. A tidal resonance occurs when all three orbital frequencies of the EMRI's secondary mass become commensurate, so when, in the simplest case, $n\omega_r + k\omega_\theta + m\omega_\phi = 0$ for integers n, k and m. In contrast to self-force resonances, the azimuthal frequency has to be taken account in the resonance condition, because the introduction of the tidal perturber breaks the axial symmetry in the EMRI's spacetime. Tidal resonances with $m = 0$ also differ from self-force resonances, because they both arise from a different force. The effect of both types of resonances is the same, in the sense that they both complicate EMRI parameter estimation [9].

On the other hand, tidal resonances, when identified correctly, can be used to map out the total spacetime of the EMRI. In particular, it is possible to infer details of the stellar distribution close to the supermassive BH, which is significantly more difficult to obtain through observations of electromagnetic waves. Furthermore, both tidal and self-force resonances can be used as precision tests of GR. When these resonances are not modeled for correctly, one may falsely draw the conclusion that GR fails in the strong gravitational regime. But if tidal and self-force resonance effects are properly taken into account, the theory of GR may be tested to high precision [5].

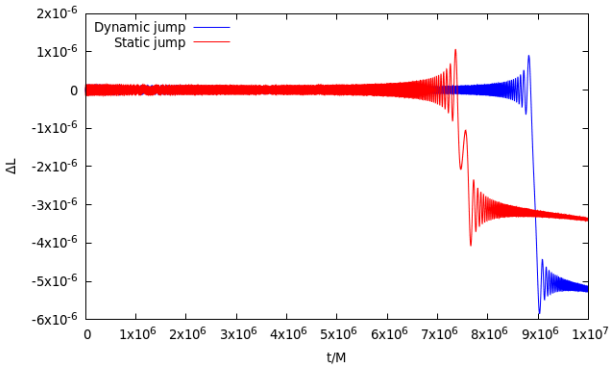

(a) The difference in L_z caused by a tidal perturber.

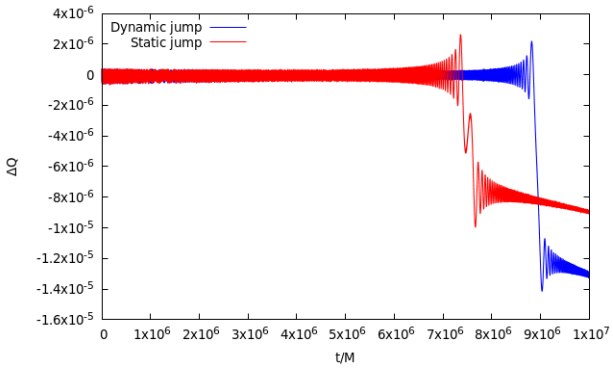

(b) The difference in Q caused by a tidal perturber.

Figure 1: The effect on an EMRI's orbital constants L_z and Q caused by a tidal perturber with mass $M_* = 30M_\odot$ at a distance $b = 10\,\mathrm{AU}$ from the EMRI's central BH with mass $M = 4\times10^6 M_\odot$. The orbit's initial conditions are given by $\{a, p, e, x\} = \{0.9M, 9M, 0.7, \cos 50°\}$ and the EMRI's mass ratio corresponds to $\eta = 7.5 \times 10^{-6}$. The orbit crosses the $(3, 0, -2)$-tidal resonance. This leads to 'jumps' in L_z and Q, which can be analyzed using a stationary and a dynamic model.

1.4 Goals of this thesis

In this thesis we will construct a theoretical framework to study tidal resonance effects in EMRIs. We will primarily focus on the semi-analytical calculation of the tidally induced jump sizes in the EMRI's orbital constants of motion, which thereafter alter the EMRI's orbital evolution and subsequently cause a phase shift in the radiated GWs. This work is based on earlier research [9, 22, 24], where the tidally induced jumps were computed using a model considering a stationary tidal field at the time of resonance. The research performed in this thesis complements this research in several ways. Firstly, we will reproduce the results of previous research in more computationally inexpensive ways. We will therefore consult to Schwarzschild perturbation theory instead of its Kerr counterpart, and we will study a faster integration method to determine the amplitude of the tidally induced jumps. Secondly, we will construct a dynamic model to study tidal resonance effects. In this model, the tidal perturber is allowed to move in a circular orbit around the EMRI system. We will compare the results of this model with the stationary model and discuss the impact on the gravitational waveform. Lastly, we will give a more complete analysis on the position of the tidal perturber in both the stationary and dynamic model. In contrast to previous research, where this analysis was performed through numerical fits, we will use a full analytical treatment of the perturber's position. The theoretical framework developed in this thesis can be used to determine more realistic tidally induced jumps in an EMRI's orbital constants of motion at low computational costs. The jump sizes can subsequently be used by the EMRI waveform modeling community [13, 24, 28] in the construction of more realistic EMRI waveform templates.

1.5 Outline of this work

We will calculate the tidally induced jumps in the constants of motion (ΔC) based on the flow diagram presented in Fig. 2. We will first determine the jump's amplitudes ($\frac{dC}{dt}$). The full calculation of these amplitudes can be divided in three theoretical branches, being the metric perturbation, Kerr geodesics and action-angle variables. After the jump's amplitudes have been obtained, we can determine the jump size as sketched by the flowchart in Fig. 9. We will now discuss the calculations performed in each branch in more detail.

At first we will calculate the perturbation in the metric arising from the presence of the tidal perturber. The roadmap of this calculation is sketched in Fig. 4. We will determine the functional form of the metric perturbation in the framework of Schwarzschild perturbation theory, which will be described in section 2.1. This is a major difference from the methods used in previous research [22, 24], where the metric perturbation was calculated in the framework of Kerr perturbation theory. We motivate this choice in section 2.1.1. The nature of the tidal perturber is incorporated in so-called tidal quadrupole moments. Generally, these moments are time dependent, which makes them well-suited for studying resonance effects induced by a dynamic tidal perturber. We will also construct the tidal moments for a stationary perturber, thereby setting-up the stationary tidal resonance model. In section 2.1.3 we formulate a metric ansatz of a tidally perturbed Schwarzschild BH based on the tidal quadrupole moments. This metric will subsequently be matched with a post-Newtonian metric to find the full functional form of the tidal moments.

An EMRI is characterized by its small mass ratio. Therefore the motion of the EMRI's smaller mass is well-approximated by geodesic motion plus a perturbative term known as the self-force. In section 2.2, we will focus on the geodesic motion only. We will formulate this motion in terms of the geodesics equations in Kerr spacetime, since we will treat the EMRI's larger mass as a Kerr BH again. We will parametrize the equations of motion with respect to Mino time, which will allow us to use fully analytical solutions for bound timelike orbits. The equations of motion, as well as its solutions, serve as input for the tidal force, as can be noted from the flowchart in Fig. 9. Since the solutions of the equations of motion are periodic in Mino time, the EMRI's orbital

motion can also be described by the so-called fundamental orbital frequencies, which are key to study tidal resonance effects. The flowchart leading to the orbital frequencies is given in Fig. 6.

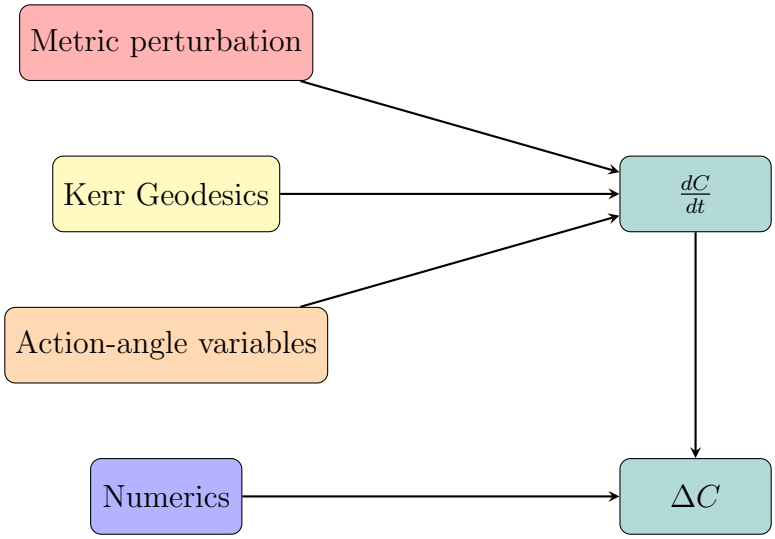

Figure 2: A flowchart describing the steps leading to the tidally induced jump size ΔC for $C \in \{L_z, Q\}$. Each process leading to the jump's amplitudes $\frac{dC}{dt}$ is discussed individually in the flowcharts presented in Figs. 4, 6 and 8. The full calculation of ΔC is presented in the flowchart in Fig. 9.

The last theoretical pillar needed to find the tidally induced jump's amplitudes is the framework of action-angle variables, which will be presented in section 2.3. This framework is well-suited to model for the EMRI's smaller mass' motion, as both the self-force and the tidal force can be taken into account perturbatively. We will neglect the self-force in our studies, because we are only interested in tidal resonances. In order to find the rate of change in the orbital constants of motion due to a tidal resonance, we will first perform a Fourier decomposition of the tidal force. Thereafter, we will make an adiabatic approximation, allowing us to find the resonance condition as well as the resonant amplitudes. The roadmap of this calculation is given in Fig. 8 in the case of a stationary tidal perturber. The analysis in the case of a dynamic perturber is slightly different, and will be discussed in detail in section 2.3.3.

All three pillars come together in the calculation of the jump's amplitudes, as presented in the flowchart in Fig. 9. In section 2.4, we will describe how we determine the tidal force. Moreover, we will discuss the averaging integral, which we use to calculate the jump's amplitudes semi-analytically. Furthermore, we will formulate the equations to calculate the total jump size. In these calculations we distinguish between the stationary model in section 2.4.1 and the dynamic model in section 2.4.2. In section 2.4.3 we will present efficient computational methods which can be used in the calculations of the total jump size. This involves the so-called two-for-one deal [23], which relates the jump size of the orbital axial angular momentum to the jump size of the Carter constant, and a faster method to perform the averaging integral. Both methods are completely new compared to previous research [22, 24] and allow for calculations of the tidally induced jump size at low computational costs.

In section 3.1 we will briefly discuss the numerical method of forced osculating orbital elements. This method will merely be used as a consistency check on our semi-analytical calculations. In section 3.2, we will discuss the results of our stationary model in detail. Moreover, they will be compared to the results of previous research. We will first discuss the case where the tidal perturber is situated on the x-axis in the equatorial plane, as sketched in Fig. 3. We will describe

how we constructed fitting formulas for the jump's amplitudes in section 3.2.1, we will analyze different resonance combinations in section 3.2.2 and we will compare semi-analytical and numerical results in section 3.2.3. In section 3.2.4 we will analyze tidal resonance effects for an arbitrary sky location of the perturber. The impact of tidal resonances on the gravitational waveform will be briefly discussed in section 3.2.5. We will then present our results of the dynamic model in section 3.3. We will first discuss the case of the equatorial plane again, after which we will assume an arbitrary sky location of the perturber. We will compare semi-analytical and numerical results, and discuss the differences between the results of the stationary and dynamic model.

1.6 Notation and conventions

In this thesis we will use geometric units, meaning that we will set the speed of light c and the gravitational constant G to a value of 1. We will use the metric signature $(-,+,+,+)$ for all metrics encountered in this work. All spacetime coordinates will be denoted by Greek indices, ranging from 0 to 3. When considered separately, we will denote all spatial coordinates by Latin indices, ranging from 1 to 3. In addition, we will sometimes denote the angular coordinates by $\theta^A = (\theta, \phi)$. The Einstein summation convention for repeated indices will be implied at all times.

In this work we will consider a tidally perturbed EMRI as sketched in Fig. 3. We will denote the mass of the tidal perturber by M_*, the mass of the EMRI's central BH by M and its smaller mass by μ. The EMRI's mass ratio is denoted by $\eta = \mu/M$. We will use an Euclidean coordinate system in the construction of the tidal moments, where the z-axis is alligned with the spin axis of M and the (x, y)-plane corresponds to the equatorial plane. In the stationary model, M_* is initially situated on the x-axis at a distance b from M. In the dynamic model, M_* is allowed to move in a circular orbit of radius b. A more general sketch of a tidally perturbed EMRI, where the perturber is situated at an arbitrary position in the sky, is given in Fig 15.

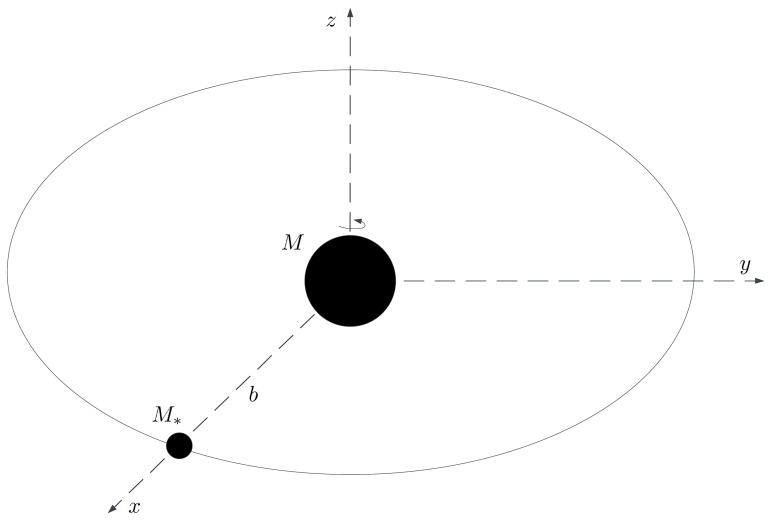

Figure 3: A sketch of an EMRI, whose central BH is of mass M, in the vicinity of a tidal perturber of mass M_*. The EMRI's secondary mass is not shown for illustrative purposes. The spin axis of M coincides with the z-axis, and the (x, y)-plane is referred to as the equatorial plane. The tidal perturber is situated on the x-axis on a distance b from M. In the dynamic model, the perturber is allowed to move in a circular orbit of radius b in the equatorial plane.

2 Theory

The goal of this thesis is to formulate a semi-analytical framework for estimating tidally induced jump sizes in an EMRI's orbital constants of motion. We will construct this framework in this theoretical section, following the roadmap as sketched in Fig. 2. In section 2.1 we will construct the perturbation in the metric induced by a tidal perturber, in section 2.2 we will describe the EMRI's orbital motion using the geodesic equations in Kerr spacetime, and section 2.3 is dedicated to the action-angle formalism. The results of these three sections come together in the calculation of the jump sizes in section 2.4, as given by the flowchart in Fig. 9.

2.1 Black hole perturbation theory

We have to resort to perturbative methods to study the influence of a tidal perturber on an EMRI system. In this subsection we will derive an expression for the metric perturbation $h_{\mu\nu}$ induced by a tidal perturbation. The steps of this derivation are sketched in the flow diagram displayed in Fig. 4. The tidal quadrupole moments $\mathcal{E}_{ab}(t)$ and $\mathcal{B}_{ab}(t)$ capture the nature of the tidal perturber, and therefore fully determine the functional form of the metric perturbation $h_{\mu\nu}$. The functional form of the tidal moments follows from the matching of two distinct metrics in their corresponding region of validity. This matching of metrics will be explained in section 2.1.3. Before that, we will discuss the set-up of this procedure.

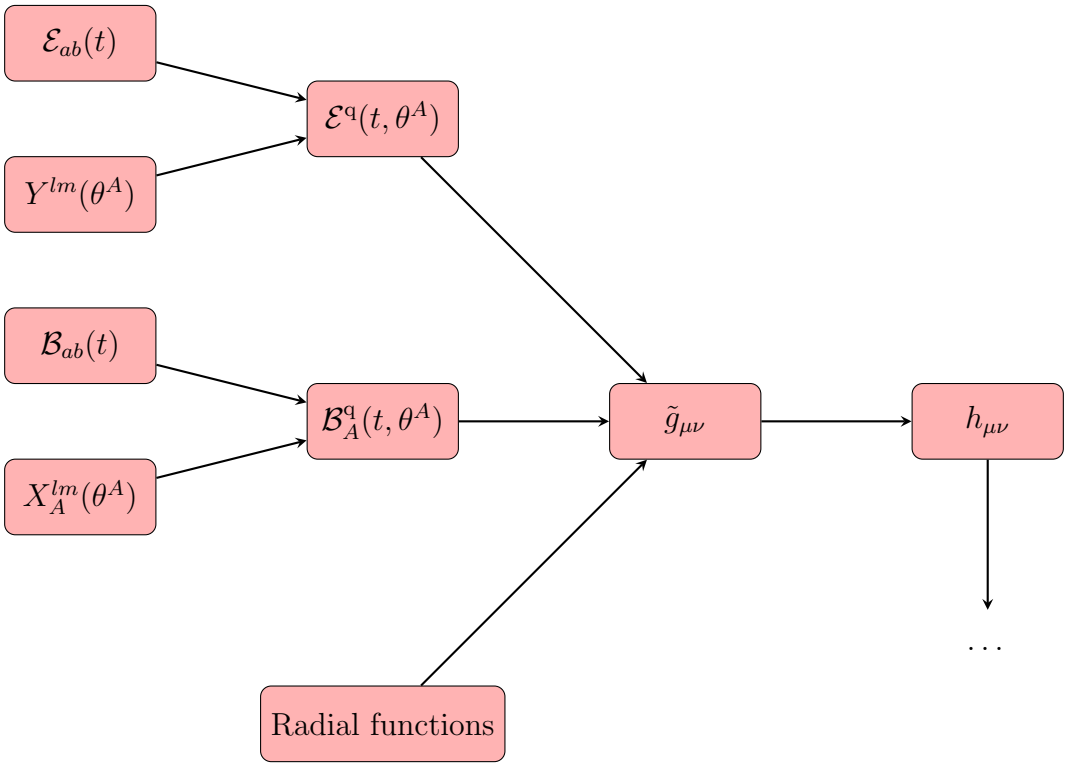

Figure 4: A flowchart describing the calculations of the metric perturbation $h_{\mu\nu}$, which will serve as input for the calculation of the tidally induced stationary jump's amplitude as described in Fig. 9.

2.1.1 Weak field approximation

The full metric $\tilde{g}_{\mu\nu}$ of a perturbed Kerr spacetime is defined as

$$\tilde{g}_{\mu\nu} = g_{\mu\nu} + h_{\mu\nu}. \tag{2.1.1}$$

Here, $g_{\mu\nu}$ is the Kerr metric and describes the unperturbed spacetime around the central BH. The line element of the Kerr solution in Boyer-Lindquist coordinates is given by [50]

$$ds^2 = -\left(1 - \frac{2Mr}{\Sigma}\right)dt^2 - \frac{4Mar\sin^2\theta}{\Sigma}dtd\phi + \frac{\Sigma}{\Delta}dr^2 + \Sigma d\theta^2 + \left(r^2 + a^2 + \frac{2Ma^2r\sin^2\theta}{\Sigma}\right)\sin^2\theta d\phi^2, \tag{2.1.2}$$

where $\Delta \equiv r^2 - 2Mr + a^2$ and $\Sigma \equiv r^2 + a^2\cos^2\theta$. The angular momentum J of the BH is captured by the spin parameter $a = \frac{J}{M}$, which is bounded by $0 < a \leq M$. Our interest lies in $h_{\mu\nu}$, which can be fully described in terms of tidal multipole moments when the tidal gravitational field is weak [56]. In this case, the central BH's scale is small compared to the radius of curvature $\mathcal{R}$ of the total spacetime. This radius is given by $\mathcal{R} = \sqrt{\frac{b^3}{M+M_*}}$, where b is the separation between the central BH and the tidal perturber. The limit where $M \ll \mathcal{R}$ is known as the small-tide approximation [48], and is given by

$$\frac{M}{\mathcal{R}} = \frac{M}{M+M_*}\left(\frac{M+M_*}{b}\right)^{\frac{3}{2}} \ll 1. \tag{2.1.3}$$

This condition is satisfied by taking

$$\frac{M+M_*}{b} \ll 1, \tag{2.1.4}$$

which is called the weak-field approximation [48]. In this case, the perturbed EMRI system can be seen as post-Newtonian. Consequently the orbital velocity of the perturber around the central BH is given by

$$u = \sqrt{\frac{M+M_*}{b}}. \tag{2.1.5}$$

The metric perturbation can be determined using Kerr perturbation theory, as was done in previous research [22, 24]. The Teukolsky equation [49] was solved in the weak field approximation, and the full metric was obtained in the ingoing radiation gauge after the metric reconstruction procedure [54]. This method, however, involves mathematically heavy calculations, which makes it computationally expensive. In this work, we will calculate $h_{\mu\nu}$ using Schwarzschild perturbation theory, which is less mathematically intense than its Kerr counterpart. So we will consider M to be a Schwarzschild BH throughout the whole construction of the metric perturbation. This means that we do not account for the central BH's spin in the tidal moments when constructing $h_{\mu\nu}$. When we analyze the dynamics of μ and investigate resonance effects, we will treat M as a Kerr BH again. While this strictly speaking is inconsistent, it notably simplifies the functional form of $h_{\mu\nu}$. This in turn enhances the computational time of analyzing the resonance effects significantly. To affirm the validity of this method, we first reproduce the results of [22, 24], in which the central BH's spin was taken into account in the construction of $h_{\mu\nu}$. Once we have established that this faster method yields accurate results, we use it to take the motion of the tidal perturber into account.

2.1.2 Tidal moments and potentials

The tidal moments encode all the information of the perturber and play a crucial role in the characterization of tidal resonances. There are two types of tidal moments, namely the gravitoelectric moments $\mathcal{E}_{ab}, \mathcal{E}_{abc}, \mathcal{E}_{abcd}, ...$ and the gravitomagnetic moments $\mathcal{B}_{ab}, \mathcal{B}_{abc}, \mathcal{B}_{abcd}, ...$ Moments with two, three and four indices are referred to as quadrupole, octupole and hexadecapole moments, respectively. The electric moments are the result of the presence of the tidal perturber, whereas the magnetic moments are produced by the perturber's dynamics. Consequently, the magnetic moments are always proportional to the perturber's orbital velocity u at the lowest post-Newtonian (0PN) order. Using a scaling analysis of the tidal environment, one can determine the scaling relations for the tidal fields [37, 39]. The electric moments scale as

$$\mathcal{E}_{ab} \sim \frac{M_*}{b^3}, \quad \mathcal{E}_{abc} \sim \frac{M_*}{b^4}, \quad \mathcal{E}_{abcd} \sim \frac{M_*}{b^5}, \tag{2.1.6}$$

and the magnetic moments as

$$\mathcal{B}_{ab} \sim \frac{M_* u}{b^3}, \quad \mathcal{B}_{abc} \sim \frac{M_* u}{b^4}, \quad \mathcal{B}_{abcd} \sim \frac{M_* u}{b^5}. \tag{2.1.7}$$

The octupole and hexadecapole moments scale with extra factors of $\frac{1}{b}$ compared to the quadrupole moments. Furthermore, the time derivatives of any of the moments above scale with an extra factor of $\frac{u}{b}$. As a result, all of these moments are suppressed in the small-tide approximation compared to the quadrupole moments. Therefore we will only consider $\mathcal{E}_{ab}$ and $\mathcal{B}_{ab}$ for the remainder of this thesis.

Formerly, tidal moments are given by the components of the Weyl tensor C_{abcd} of the external spacetime. The quadrupole moments are given by [35]

$$\mathcal{E}_{ab} = C_{a0b0}, \tag{2.1.8a}$$

$$\mathcal{B}_{ab} = \frac{1}{2}\left(\epsilon_{apq} C^{pq}{}_{b0}\right), \tag{2.1.8b}$$

where ϵ_{abc} is the Levi-Civita symbol in three dimensions with $\epsilon_{123} = 1$. All tidal tensors are symmetric and tracefree, as these properties are inherited from the Weyl tensor. Moreover, by studying parity transformations on the Weyl tensor and by mapping these relations back to the tidal tensors, it can be shown that the electric moments transform as Cartesian tensors under parity transformations while the magnetic moments transform as pseudotensors. Ergo, the electric moments have even parity while the magnetic moments have odd parity [39].

$Y^{2,0} = 1 - 3\cos^2\theta$	$\mathcal{E}^{\mathrm{q}}_0 = \frac{1}{2}(\mathcal{E}_{11} + \mathcal{E}_{22})$
$Y^{2,1c} = 2\sin\theta\cos\theta\cos\phi$	$\mathcal{E}^{\mathrm{q}}_{1c} = \mathcal{E}_{13}$
$Y^{2,1s} = 2\sin\theta\cos\theta\sin\phi$	$\mathcal{E}^{\mathrm{q}}_{1s} = \mathcal{E}_{23}$
$Y^{2,2c} = \sin^2\theta\cos 2\phi$	$\mathcal{E}^{\mathrm{q}}_{2c} = \frac{1}{2}(\mathcal{E}_{11} - \mathcal{E}_{22})$
$Y^{2,2s} = \sin^2\theta\sin 2\phi$	$\mathcal{E}^{\mathrm{q}}_{2s} = \mathcal{E}_{12}$

Table 1: Scalar $l = 2$ spherical harmonic functions (left column) and the harmonic components of the type-$\mathcal{E}$ tidal potential (right column).

The tidal moments are incorporated in the tidally deformed metric through irreducible tidal potentials. These tidal potentials can be constructed in terms of scalar, vectorial and tensorial spherical harmonics. Each potential is also related to a specific parity label and a multipole order l. For example, the quadrupolar tidal potentials are of multipole order $l = 2$ and are therefore given in terms of $l = 2$ spherical harmonics. The octupolar and hexadecapolar potentials have multipole order $l = 3$ and $l = 4$, respectively. The even-parity electric quadrupolar scalar potential is expressed in terms of scalar spherical harmonic functions $Y^{lm}(\theta^A)$ as

$$\mathcal{E}^{\mathrm{q}}(t, \theta^A) = \sum_{-2 \le m \le 2} \mathcal{E}^{\mathrm{q}}_m(t) Y^{2m}(\theta^A). \tag{2.1.9}$$

The scalar harmonics satisfy the eigenvalue equation

$$\Omega^{AB} D_A D_B Y^{lm} = -l(l+1) Y^{lm} \tag{2.1.10}$$

and only depend on $\theta^A = (\theta, \phi)$, which denotes the angular coordinates on the unit two-sphere with metric $\Omega_{AB} = \mathrm{diag}[1, \sin^2\theta]$ and covariant derivative D_A. The sum in m in Eq. (2.1.9) ranges from -2 to 2, because the quadrupole moments carry the $l = 2$ multipole order. We preferably work with real-valued spherical harmonic functions, because then the tidal moments can be treated

in a real setting as well. Therefore we rewrite $Y^{2m}(\theta^A)$ in a real (cosine) part $Y^{2,mc}(\theta^A)$ and an imaginary (sine) part $Y^{2,ms}(\theta^A)$ for $m = \pm 1$ and $m = \pm 2$. The harmonic components $\mathcal{E}^{\mathrm{q}}_m$, as a function of $\mathcal{E}_{ab}$, as well as the the functional forms of $Y^{2,mc}$ and $Y^{2,ms}$ are displayed in Table 1. In the description of the tidally perturbed metric, we also need the odd-parity magnetic quadrupolar vector potential, which is given by

$$\mathcal{B}^{\mathrm{q}}_A(t,\theta^A) = \frac{1}{2}\sum_{-2\leq m\leq 2} \mathcal{B}^{\mathrm{q}}_m(t) X^{2m}_A(\theta^A). \tag{2.1.11}$$

The harmonic components $\mathcal{B}^{\mathrm{q}}_m$ are displayed in Table 2. The odd-parity vectorial harmonics $X^{lm}_A(\theta^A)$ are given by

$$X^{lm}_A(\theta^A) = -\epsilon_A{}^B D_B Y^{lm}(\theta^A), \tag{2.1.12}$$

where ϵ_{AB} is the Levi-Civita tensor on the unit-two sphere. The nonzero components of the Levi-Civita tensor are given by $\epsilon_{\theta\phi} = -\epsilon_{\phi\theta} = \sin\theta$. The $l = 2$ vectorial harmonics are shown in Table 2. [36, 37]

$X^{2,0}_\theta = 0$	$X^{2,0}_\phi = 6\sin^2\theta\cos\theta$	$\mathcal{B}^{\mathrm{q}}_0 = \frac{1}{2}(\mathcal{B}_{11} + \mathcal{B}_{22})$
$X^{2,1c}_\theta = 2\sin\theta\cos\theta\sin\phi$	$X^{2,1c}_\phi = 2\sin\theta\cos 2\theta\cos\phi$	$\mathcal{B}^{\mathrm{q}}_{1c} = \mathcal{B}_{13}$
$X^{2,1s}_\theta = -2\sin\theta\cos\theta\cos\phi$	$X^{2,1s}_\phi = 2\sin\theta\cos 2\theta\sin\phi$	$\mathcal{B}^{\mathrm{q}}_{1s} = \mathcal{B}_{23}$
$X^{2,2c}_\theta = 2\sin^2\theta\sin 2\phi$	$X^{2,2c}_\phi = 2\sin^2\theta\cos\theta\cos 2\phi$	$\mathcal{B}^{\mathrm{q}}_{2c} = \frac{1}{2}(\mathcal{B}_{11} - \mathcal{B}_{22})$
$X^{2,2s}_\theta = -2\sin^2\theta\cos 2\phi$	$X^{2,2s}_\phi = 2\sin^2\theta\cos\theta\sin 2\phi$	$\mathcal{B}^{\mathrm{q}}_{2s} = \mathcal{B}_{12}$

Table 2: Vector $l = 2$ spherical harmonic functions (left and middle column) and the harmonic components of the type-$\mathcal{B}$ tidal potential (right column).

2.1.3 Metric matching

The metric of a tidally deformed Schwarzschild BH can be given as an expansion in $\frac{r}{b}$, which is valid in the regime where $r < r_{\max} \ll b$. Here, $r_{\max}$ is a value of r that is sufficiently smaller than b. The tidally distorted Schwarzschild metric is presented in the Regge-Wheeler gauge, so that the magnetic potentials of odd parity only appear in the tA and rA metric coefficients, while the even-parity electric potentials appear in the tt, tr, rr and AB components of the metric [32]. As we will only include the leading order quadrupole moments, the tidally distorted Schwarzschild metric in (t, r, θ, ϕ)-coordinates takes the form

$$\tilde{g}_{tt} = -f + r^2 e^{\mathrm{q}}_{tt}\mathcal{E}^{\mathrm{q}}, \tag{2.1.13a}$$
$$\tilde{g}_{tr} = 0, \tag{2.1.13b}$$
$$\tilde{g}_{rr} = f^{-1} + r^2 e^{\mathrm{q}}_{rr}\mathcal{E}^{\mathrm{q}}, \tag{2.1.13c}$$
$$\tilde{g}_{tA} = r^3 b^{\mathrm{q}}_t \mathcal{B}^{\mathrm{q}}_A, \tag{2.1.13d}$$
$$\tilde{g}_{rA} = 0, \tag{2.1.13e}$$
$$\tilde{g}_{AB} = r^2\Omega_{AB}\left(1 + r^2 e^{\mathrm{q}}\mathcal{E}^{\mathrm{q}}\right), \tag{2.1.13f}$$

where $f = 1 - \frac{2M}{r}$ and e^{q}_{tt}, e^{q}_{rr}, e^{q} and b^{q}_t are radial functions which are stated in Table 3. These functions can be determined by solving the linearized Einstein field equations in vacuum. An example of such a calculation is given in Appendix A. [37]

$e^{\mathrm{q}}_{tt} = -f^2$
$e^{\mathrm{q}}_{rr} = -1$
$e^{\mathrm{q}} = -1 + \frac{2M^2}{r^2}$
$b^{\mathrm{q}}_{t} = \frac{2}{3} f$

Table 3: Radial functions appearing in Eq. (2.1.13).

In order to determine the functional form of the tidal moments, we have to match the metric given in Eq. (2.1.13) with a post-Newtonian (PN) metric of the Schwarzschild BH. A general form of such a metric up to 1PN order is given by

$$\tilde{g}_{tt} = -1 + 2U + 2(\Psi - U^2) + 2\mathrm{PN}, \tag{2.1.14a}$$
$$\tilde{g}_{ta} = -4U_a + 2\mathrm{PN}, \tag{2.1.14b}$$
$$\tilde{g}_{ab} = (1 + 2U)\delta_{ab} + 2\mathrm{PN}, \tag{2.1.14c}$$

and involves a Newtonian potential U, a PN potential Ψ and a vector potential U_a [52]. We have denoted the flat three-dimensional Euclidean metric by δ_{ab}. The metric in Eq. (2.1.14) is valid in the PN zone, marked by $r > r_{\mathrm{min}} \gg M$. Here, r_{min} corresponds to a value of r sufficiently greater than M. This in turn allows for a PN description of the tidal moments

$$\mathcal{E}_{ab} = \mathcal{E}_{ab}(0PN) + \mathcal{E}_{ab}(1PN) + 2\mathrm{PN}, \tag{2.1.15a}$$
$$\mathcal{B}_{ab} = \mathcal{B}_{ab}(0PN) + \mathcal{B}_{ab}(1PN) + 2\mathrm{PN}. \tag{2.1.15b}$$

These expressions can be substituted in Eqs. (2.1.9) and (2.1.11), which in turn can be substituted in Eq. (2.1.13). The resulting metric can thereafter be matched with the PN metric of Eq. (2.1.14). This metric matching procedure is only allowed in the regime where both metrics are valid. This region of validity is given by the regime $M \ll r_{\mathrm{min}} < r < r_{\mathrm{max}} \ll b$ and is graphically shown in Fig. 5. [7, 36, 48]

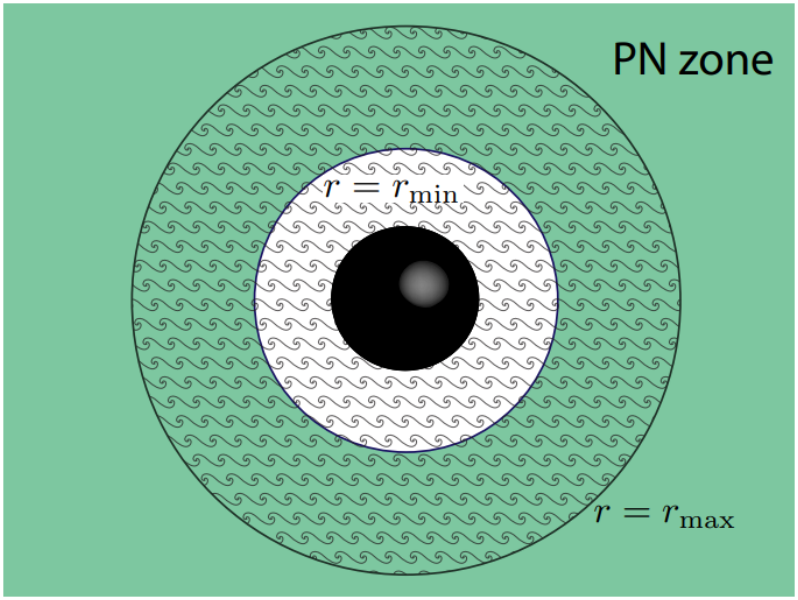

Figure 5: The metric of Eq. (2.1.13) is valid in the region where $r < r_{\mathrm{max}} \ll b$. This region is relatively close to the central BH and is depicted by the wavy pattern. The PN metric (Eq. (2.1.14)) is valid in the green PN zone, characterized by $r > r_{\mathrm{min}} \gg M$. The region of validity in the metric matching procedure is given by $r_{\mathrm{min}} < r < r_{\mathrm{max}}$ if $M \ll b$. Figure adapted from [36].

The PN-expanded tidal moments can be expressed in terms of the potentials U, Ψ and U_a as a result of the metric matching procedure. The functional form of the tidal moments can then be retrieved by specifying the nature of these potentials. We assume the relatively simple case that the tidal perturber moves in a circular orbit around the central BH, as displayed in Fig. 3. Consequently, the functional form of the potentials U, Ψ and U_a can be fully specified in terms of M_*, b and u. As the subsequent calculations leading to the tidal quadrupole moments are quite long, we only state the final form of these moments. More details regarding the metric matching procedure can be found in [36, 37]. The electric and magnetic quadrupole moments are given by

$$\mathcal{E}_{ab}(t) = -3\frac{M_*}{b^3} n_{\langle a} n_{b\rangle} + 1\text{PN}, \tag{2.1.16a}$$

$$\mathcal{B}_{ab}(t) = -6\frac{M_* u}{b^3} n_{\langle a} \lambda_{b\rangle} + 1\text{PN}. \tag{2.1.16b}$$

Here, the angular brackets around the indices denote the symmetrization and trace removal of the vector product [11]:

$$n_{\langle a}\lambda_{b\rangle} \equiv \frac{1}{2}(n_a\lambda_b + \lambda_a n_b) - \frac{1}{3}\delta_{ab} n^c \lambda_c. \tag{2.1.17}$$

The tidal moments in Eq. (2.1.16) are expressed in terms of the orthogonal unit vectors

$$n_a \equiv n_a(t) = -(\cos(\Omega_\phi t), \sin(\Omega_\phi t), 0), \tag{2.1.18a}$$

$$\lambda_a \equiv \lambda_a(t) = (\sin(\Omega_\phi t), -\cos(\Omega_\phi t), 0), \tag{2.1.18b}$$

which are given in a Cartesian (x, y, z)-notation in the frame of the central BH. The z-axis coincides with the spin axis of the central BH and the (x, y)-plane corresponds to the equatorial plane. We have chosen that the perturber is situated on the x-axis at the time $t = 0$. The time dependence of the tidal moments is encoded in the unit vectors n_a and λ_a. The orbital frequency of the perturber is given by

$$\Omega_\phi = \sqrt{\frac{M + M_*}{b^3}} + 1\text{PN}. \tag{2.1.19}$$

Both tidal moments are only given at 0PN order, as the 1PN order scales with u^2. In the region of validity where $M \ll b$, the contribution of the 1PN term will be small compared to the zeroth PN order. Therefore we will not include any higher order PN terms in further calculations performed in this thesis. [37]

The metric of the full spacetime is now given by Eq. (2.1.13), where the tidal potentials are constructed in terms of the tidal moments expressed in Eq. (2.1.16). The metric perturbation is then easily retrieved by subtracting the Schwarzschild metric.

2.2 Kerr geodesics

Since the EMRI mass ratio $\eta = \frac{\mu}{M}$ is extremely small, the motion of the secondary mass around the central BH can be described by the geodesic equations in Kerr spacetime plus radiation reaction causing the inspiral [40]. In this subsection we will only focus on the geodesic motion. We will follow the roadmap as given in Fig. 6. We will present the equations of motion in Kerr spacetime with respect to Mino time, as that will be beneficial to us when we will perform the so-called averaging integrals in section 2.4. These equations of motion can be solved analytically, and will ultimately lead to the fundamental orbital frequencies needed to study different tidal resonance combinations.

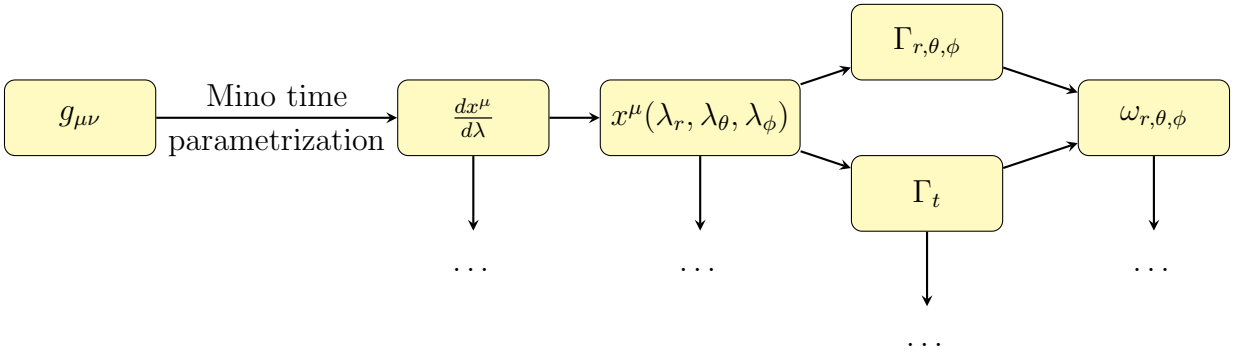

Figure 6: A flowchart describing the calculations of several quantities based on the Mino time parametrization. These quantities will serve as input for the calculation of the tidally induced jump's amplitude as described in Fig. 9.

The geodesic equations in Kerr spacetime can be described by four constants of motion $\{\mu,E,L_z,Q\}$, where μ is the EMRI's smaller mass. The orbital energy $E = -u_t$ is given per unit μ, the z-component of the orbital angular momentum $L_z = u_\phi$ is given per unit μM and the Carter constant $Q = u_\theta^2 + \cos^2\theta \left(a^2(1-E^2) + \left(\frac{L_z}{\sin\theta}\right)^2\right)$ [12] is given per unit $\mu^2 M^2$. Here, u^μ is the four-velocity of the EMRI's smaller mass. Consequently, its motion is fully determined by the constants $\{E,L_z,Q\}$. By using the definitions of these constants of motion in combination with the Kerr metric (Eq. (2.1.2)), we find four ordinary differential equations for the geodesics in terms of the Boyer-Lindquist coordinates [14, 33, 34]:

$$\frac{dt}{d\lambda} = T_r(r) + T_\theta(\cos\theta) + aL_z, \tag{2.2.1a}$$

$$\left(\frac{dr}{d\lambda}\right)^2 = R(r), \tag{2.2.1b}$$

$$\left(\frac{d\theta}{d\lambda}\right)^2 = \Theta(\theta), \tag{2.2.1c}$$

$$\frac{d\phi}{d\lambda} = \Phi_r(r) + \Phi_\theta(\cos\theta) - aE. \tag{2.2.1d}$$

The radial functions are given by

$$R(r) = \left(E(r^2+a^2)^2 - aL_z\right)^2 - \Delta\left(r^2 + (L_z - aE)^2 + Q\right), \tag{2.2.2a}$$

$$T_r(r) = \frac{r^2+a^2}{\Delta}\left(E(r^2+a^2) - aL_z\right), \tag{2.2.2b}$$

$$\Phi_r(r) = \frac{a}{\Delta}\left(E(r^2+a^2) - aE\right), \tag{2.2.2c}$$

and the polar functions are given by

$$\Theta(\theta) = Q - L_z \cot^2\theta - a^2(1-E^2)\cos^2\theta, \tag{2.2.3a}$$

$$T_\theta(\cos\theta) = a^2 E(\cos^2\theta - 1), \tag{2.2.3b}$$

$$\Phi_\theta(\cos\theta) = \frac{L_z}{1-\cos^2\theta}. \tag{2.2.3c}$$

The equations of motion in Eq. (2.2.1) are parametrized in terms of Mino time λ, which is related to μ's proper time τ by $d\tau = \Sigma d\lambda$. We have chosen this parametrization as this decouples the radial and polar differential equations. Because of the quadratic nature of Eqs. (2.2.2a) and (2.2.3a), $r(\lambda)$ and $\theta(\lambda)$ are periodic functions for bound orbits with respective Mino-time periods Λ_r and Λ_θ. These periods are given by [16, 42]

$$\Lambda_r = 2\int_{r_\mathrm{p}}^{r_\mathrm{a}} \frac{dr}{\sqrt{R(r)}}, \qquad \Lambda_\theta = 4\int_{\theta_\mathrm{min}}^{\frac{\pi}{2}} \frac{d\theta}{\sqrt{\Theta(\theta)}}. \tag{2.2.4}$$

Here, r_p and r_a correspond to the values of r at the periapsis and the apoapsis, respectively, and θ_min is the minimum value of θ. The periodic motion in r and θ ensures that $r_\mathrm{p} \leq r \leq r_\mathrm{a}$ and $\theta_\mathrm{min} \leq \theta \leq \pi - \theta_\mathrm{min}$. Consequently, a bound geodesic in Kerr spacetime can also be described by the constants $\{r_\mathrm{p}, r_\mathrm{a}, \theta_\mathrm{min}\}$ instead of $\{E, L_z, Q\}$. The relations between both sets of constants can be found in Appendix B of [44].

The motion in t and ϕ is not fully periodic. However, Eqs. (2.2.1a) and (2.2.1d) are given as a sum of a radial and a polar function, which both oscillate with their respective Mino-time periods given in Eq. (2.2.4), and a constant term. Hence, the motion in t and ϕ is given by [18, 22, 31]

$$t(\lambda) = t_0 + \Gamma_t \lambda + t_\lambda^{(r)} + t_\lambda^{(\theta)}, \tag{2.2.5a}$$

$$\phi(\lambda) = \phi_0 + \Gamma_\phi \lambda + \phi_\lambda^{(r)} + \phi_\lambda^{(\theta)}, \tag{2.2.5b}$$

where t_0 and ϕ_0 specify the initial conditions and $t_\lambda^{(r)/(\theta)}$ and $\phi_\lambda^{(r)/(\theta)}$ are oscillatory functions with periods $\Lambda_{r/\theta}$. Furthermore, the linear terms in λ depend on the temporal and azimuthal Mino-time frequencies [18]

$$\Gamma_t = \langle T_r(r)\rangle_\lambda + \langle T_\theta(\cos\theta)\rangle_\lambda + aL_z, \tag{2.2.6a}$$

$$\Gamma_\phi = \langle \Phi_r(r)\rangle_\lambda + \langle \Phi_\theta(\cos\theta)\rangle_\lambda - aE. \tag{2.2.6b}$$

Here, $\langle\cdots\rangle_\lambda$ refers to time averaging with respect to λ [34]:

$$\langle T_r(r)\rangle_\lambda = \frac{1}{\Lambda_r}\int_0^{\Lambda_r} T_r(r)d\lambda, \qquad \langle T_\theta(\cos\theta)\rangle_\lambda = \frac{1}{\Lambda_\theta}\int_0^{\Lambda_\theta} T_\theta(\cos\theta)d\lambda, \tag{2.2.7a}$$

$$\langle \Phi_r(r)\rangle_\lambda = \frac{1}{\Lambda_r}\int_0^{\Lambda_r} \Phi_r(r)d\lambda, \qquad \langle \Phi_\theta(\cos\theta)\rangle_\lambda = \frac{1}{\Lambda_\theta}\int_0^{\Lambda_\theta} \Phi_\theta(\cos\theta)d\lambda. \tag{2.2.7b}$$

The radial and polar Mino-time frequencies are given by their corresponding periods

$$\Gamma_{r,\theta} = \frac{2\pi}{\Lambda_{r,\theta}}. \tag{2.2.8}$$

Analytical solutions of all four Mino-time frequencies as a function of $\{a, r_\mathrm{p}, r_\mathrm{a}, \theta_\mathrm{min}\}$ are presented in sections 3.2 and 3.3 of [18] and are implemented in the *KerrGeodesics* package of the Black Hole Perturbation Toolkit (BHPT) [1].

The fundamental orbital frequencies as measured by a distant observer are obtained by dividing the orbital Mino-time frequencies by Γ_t [15]:

$$\omega_{r,\theta,\phi} = \frac{\Gamma_{r,\theta,\phi}}{\Gamma_t}. \tag{2.2.9}$$

Here, ω_ϕ describes the periodic motion in the equatorial plane, while ω_r and ω_θ give the oscillations in the radial and polar direction, respectively. The Kerr geodesic orbit can also be specified in terms of the semi-latus rectum p, the orbital eccentricity e and cosine of the orbital inclination angle $x = \cos I$. These orbital parameters are given as a function of $\{r_\mathrm{p}, r_\mathrm{a}, \theta_\mathrm{min}\}$ by [22]

$$p = \frac{2 r_\mathrm{p} r_\mathrm{a}}{M(r_\mathrm{p} + r_\mathrm{a})}, \tag{2.2.10a}$$

$$e = \frac{r_\mathrm{a} - r_\mathrm{p}}{r_\mathrm{a} + r_\mathrm{p}}, \tag{2.2.10b}$$

$$x = \cos\left(\frac{\pi}{2} - \mathrm{sgn}(L_z)\theta_\mathrm{min}\right). \tag{2.2.10c}$$

It is convenient to use this characterization of the Kerr geodesic orbit in order to map out the whole parameter space, because $0 < e < 1$ and $-1 \leq x \leq 1$. The semi-latus rectum is bounded from below by the separatrix p_s. The gravitational pull of the central BH is too strong when $p < p_s$, as a result of which the bound orbit becomes a plunge orbit. [44]

The fundamental orbital frequencies can also be written as a function of $\{a,p,e,x\}$. Figure 7 shows these frequencies as a function of p. Near the central BH the frequencies strongly deviate from each other, whereas they asymptotically tend towards the frequency given by Kepler's law in the weak field regime. The orbital frequencies as a function of $\{a,p,e,x\}$ are also implemented in the *KerrGeodesics* package of the Black Hole Perturbation Toolkit (BHPT) [1], and are comprehensively used in this work to study tidal resonance effects.

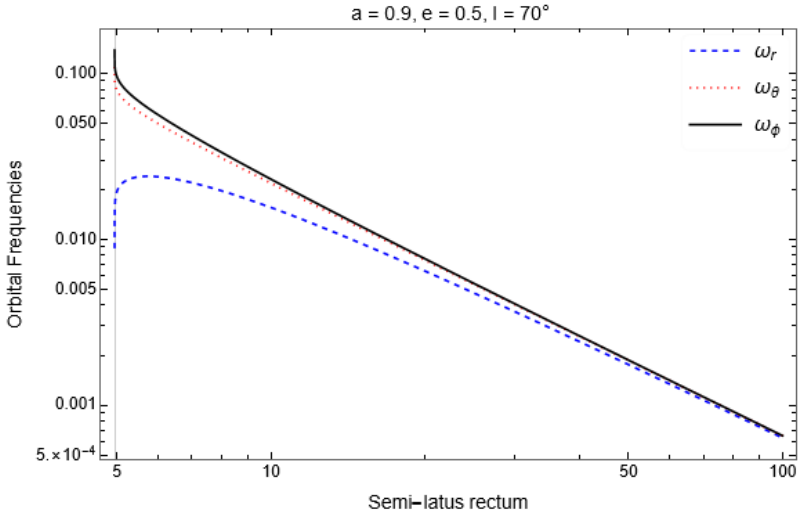

Figure 7: The dimensionless fundamental orbital frequencies as a function of the semi-latus rectum p for given values of a, e and $x = \cos I$. The separatrix is shown by the vertical grey line.

2.3 EMRI evolution

In this subsection we will focus on the radiation reaction which drives the evolution of the EMRI. The radiation reaction can be described by the gravitational self-force, which is given by a dissipative and a conservative piece. The inspiral is caused by the dissipative part of the self-force, corresponding to slow timescales ($\sim M/\eta$), and induces the dissipation of orbital angular momentum and energy through gravitational radiation. The conservative part of the self-force describes the orbital dynamics of the secondary mass around the central BH. It is associated with short timescales ($\sim M$) and is therefore generally subdominant to the dissipative piece of the self-force. This is referred to as the adiabatic approximation [25, 41].

The EMRI's evolution is most easily modeled in the formalism of action-angle variables, because the EMRI spacetime is highly symmetric in the test particle limit of the EMRI's smaller mass. Besides that, both the gravitational self-force and the tidal force can be added to the EMRI's evolution equations perturbatively. When we analyze the perturbed EMRI, we can easily distinguish the adiabatic terms from the resonant terms, which makes this formalism of action-angle variables well-suited to study resonance effects in EMRIs [29]. The resonant terms ($G^{(1)}_{i,nkm}$) can cause a jump in the EMRI's orbital constants of motion when the tidal resonance condition ($\omega_{nkm} = 0$) is satisfied. The roadmap to determine the resonant terms and the resonance condition is presented in Fig. 8 in the case of the stationary model. The roadmap for the dynamic model has an equivalent structure, but a slightly different notation.

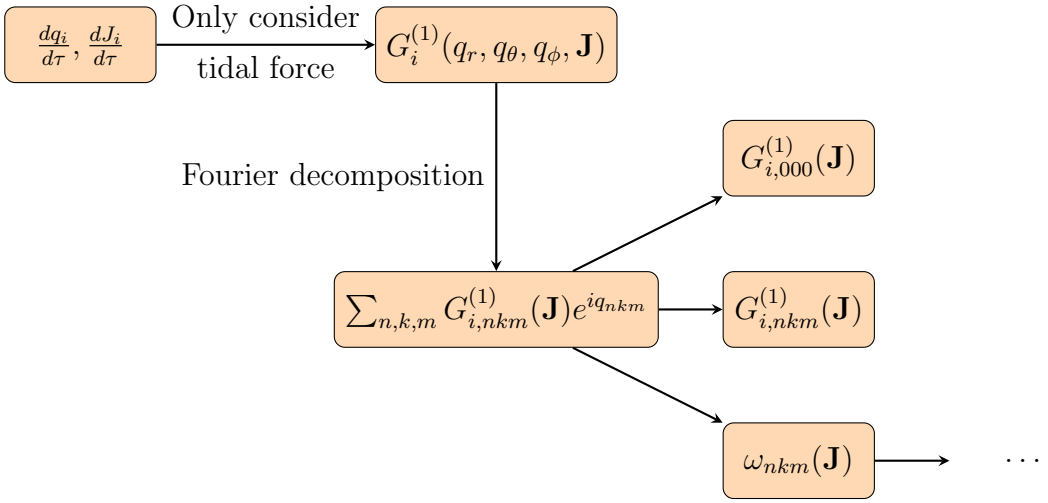

Figure 8: A flowchart describing the determination of the resonance condition $\omega_{nkm} = 0$, which will serve as input for the calculation of the tidally induced stationary jump's amplitude as described in Fig. 9. Furthermore, the Fourier decomposition of the tidal force allows the resonant terms $G^{(1)}_{i,nkm}(\mathbf{J})$ to be distinguished from the adiabatic terms $G^{(1)}_{i,000}(\mathbf{J})$.

2.3.1 Action-angle variables

In the framework of action-angle variables, the equations of motion in the EMRI's spacetime can be written in terms of angles q_i with corresponding actions J_i. The actions are functions of the orbital constants $\{E,L_z,Q\}$ and correspond to integrals of motion. They are generally given (per unit μ) as [29]

$$J_i = \frac{1}{2\pi} \oint u_i \, dx_i. \tag{2.3.1}$$

The integrals are calculated for one oscillation with respect to the integration variable. In Boyer-Lindquist coordinates, the actions are given by [44]

$$J_t = -E, \qquad J_r = \frac{1}{2\pi}\oint \frac{\pm\sqrt{R(r)}}{\Delta} dr, \tag{2.3.2a}$$

$$J_\phi = L_z, \qquad J_\theta = \frac{1}{2\pi}\oint \pm\sqrt{\Theta(\theta)} d\theta. \tag{2.3.2b}$$

The plus-minus signs in the equations on the right-hand side are chosen to be negative/positive if the integration variable decreases/increases. The actions are conserved if the motion is geodesic. The angles q_i then evolve at constant rates, which are equal to the fundamental orbital frequencies given in Eq. (2.2.9). As a result, the geodesic motion in r, θ and ϕ can be written as

$$\frac{dq_i}{d\tau} = \omega_i(\mathbf{J}), \tag{2.3.3a}$$

$$\frac{dJ_i}{d\tau} = 0, \tag{2.3.3b}$$

where the orbital frequencies are now given in terms of the actions $\mathbf{J} = \{J_r, J_\theta, J_\phi\}$. The action-angle formalism is well suited to perturbatively add the effect of the gravitational self-force and the tidal force. Therefore we expand the equations of motion in the smallness parameters η and ϵ, where the latter determines the strength of the tidal field:

$$\epsilon = \frac{M_* M^2}{b^3}. \tag{2.3.4}$$

2.3.2 Stationary approach

Before we can perturb the equations of motion, we have to specify the nature of the tidal perturber. We will first assume that the perturber is stationary on the timescale of a tidal resonance, which means that the tidal force does not depend on the dynamics of the perturber. As a result, the perturbative expansion of Eq. (2.3.3) is given by [9, 30]

$$\frac{dq_i}{d\tau} = \omega_i(\mathbf{J}) + \eta\ g^{(1)}_{i,\mathrm{sf}}(q_r, q_\theta, \mathbf{J}) + \epsilon\ g^{(1)}_{i,\mathrm{td}}(q_r, q_\theta, q_\phi, \mathbf{J}) + \mathcal{O}(\eta^2, \epsilon^2, \eta\epsilon), \tag{2.3.5a}$$

$$\frac{dJ_i}{d\tau} = \eta\ G^{(1)}_{i,\mathrm{sf}}(q_r, q_\theta, \mathbf{J}) + \epsilon\ G^{(1)}_{i,\mathrm{td}}(q_r, q_\theta, q_\phi, \mathbf{J}) + \mathcal{O}(\eta^2, \epsilon^2, \eta\epsilon). \tag{2.3.5b}$$

We note that the self-force terms $\left(g^{(1)}_{i,\mathrm{sf}}, G^{(1)}_{i,\mathrm{sf}}\right)$ scale with the EMRI mass ratio while the tidal force terms $\left(g^{(1)}_{i,\mathrm{td}}, G^{(1)}_{i,\mathrm{td}}\right)$ scale with ϵ. Moreover, the self-force is independent of the angle q_ϕ, because the Kerr spacetime is axisymmetric in the central BH's spin axis. The tidal force does depend on q_ϕ, as the introduction of the tidal perturber breaks the axisymmetry of the Kerr spacetime unless the perturber is situated exactly at the central BH's spin axis.

Because we want to study tidal resonance effects in the EMRI system, we will only focus on the tidal force $G^{(1)}_{i,\mathrm{td}}$ and omit the subscript 'td'. The adiabatic approximation tells us that, to lowest order, Eq. (2.3.5) can be written as [25]

$$\frac{dq_i}{d\tau} \approx \omega_i(\mathbf{J}), \tag{2.3.6a}$$

$$\frac{dJ_i}{d\tau} \approx \epsilon \left\langle G^{(1)}_i(q_r, q_\theta, q_\phi, \mathbf{J}) \right\rangle. \tag{2.3.6b}$$

Here, the angular brackets denote the phase space average over the 3-torus spanned by the angles. In order to calculate the average of the tidal force, we first rewrite the force by performing a Fourier decomposition:

$$G_i^{(1)}(q_r, q_\theta, q_\phi, \mathbf{J}) = \sum_{n,k,m} G_{i,nkm}^{(1)}(\mathbf{J}) e^{i(nq_r + kq_\theta + mq_\phi)}. \tag{2.3.7}$$

Here we have decoupled the angles from the actions. The angles appear in the exponential function as a total angular phase $q_{nkm} := nq_r + kq_\theta + mq_\phi$. Because the exponential is an oscillatory function, all these terms generally drop out in the averaging process. This is true, except for two cases when the exponential does not oscillate. The first case corresponds to the adiabatic approximation, where $n = k = m = 0$. The second case occurs when the time derivative of the exponent vanishes. By using the definition of the time derivatives of the angles in Eq. (2.3.6a), we find the stationary resonance condition

$$\omega_{nkm} := n\omega_r + k\omega_\theta + m\omega_\phi = 0. \tag{2.3.8}$$

We say that a tidal resonance occurs if we can find any set of integers (n,k,m) that satisfies the resonance condition. If the EMRI is on resonance, the geodesic orbit only traverses a subset of the (q_r,q_θ,q_ϕ)-torus, whereas the orbit generally covers this torus entirely. As a result, the average of the tidal force is given by the sum of $G_{i,000}^{(1)}$ and the other coefficients $G_{i,nkm}^{(1)}$ for which n, k and m satisfy the stationary resonance condition in Eq. (2.3.8). However, the contribution of $G_{i,000}^{(1)}$ is suppressed compared to the resonant coefficients, because the tidal field is weak. As a result, the change in the actions is completely determined by the coefficients $G_{i,nkm}^{(1)}$ at the time of resonance [22].

The resonance condition can effectively be satisfied an infinite number of times, as the only restriction on (n,k,m) is that they have to be integers. However, the EMRI is not on resonance during most of the inspiral. This can be explained from the fact that only resonances with low values of (n,k,m) dominate. Such resonances are referred to as low-order resonances. Resonant orbits with a high resonance order already cover a large part of the (q_r,q_θ,q_ϕ)-torus and genuinely average over the torus in the process. Furthermore, if a tidal resonance occurs for a set of integers (n,k,m), it actually means that the resonance condition is also satisfied for the set (jn,jk,jm) for every $j \in \mathbb{Z}$. However, these higher order resonances are also subdominant based on the previous argument. Therefore we will only consider resonances with $|j| = 1$ for the remainder of this work. [47]

The assumption of a stationary perturber is valid as long as tidal resonances occur on much shorter timescales than the orbital period of the perturber. The latter is given by $T_{\rm td} = \frac{2\pi}{\Omega_\phi}$, where Ω_ϕ is given by Eq. (2.1.19). In order to determine the resonance duration $\tau_{\rm res}$, we can expand q_{nkm} in a Taylor series around the time of resonance $\tau = \tau_0$:

$$q_{nkm} = \chi_s + (n\omega_{r0} + k\omega_{\theta 0} + m\omega_{\phi 0})(\tau - \tau_0) + \frac{1}{2}\Gamma(\tau - \tau_0)^2 + \cdots . \tag{2.3.9}$$

Here, $\chi_s = q_{r0} + q_{\theta 0} + q_{\phi 0}$ denotes the total phase at the time of resonance. The second term involves the stationary resonance condition at the time of resonance and therefore evaluates to zero. In the third term, $\Gamma = n\dot{\omega}_{r0} + k\dot{\omega}_{\theta 0} + m\dot{\omega}_{\phi 0}$, where the $\dot{\omega}_{i0}$ represent the derivative of the fundamental frequencies with respect to proper time evaluated at τ_0. A tidal resonance endures as long as the total phase remains stationary. This condition is violated when the third term on the right-hand side of Eq. (2.3.9) becomes dominant. Therefore, the factor $\frac{1}{2}\Gamma$ scales with $\tau_{\rm res}^{-2}$. This leads to our definition of the resonance duration [24]

$$\tau_{\rm res} = \sqrt{\frac{4\pi}{|\Gamma|}} \sim M\sqrt{\frac{1}{\eta}}. \tag{2.3.10}$$

Hence, the stationary perturber approximation holds when $\tau_{\rm res} \ll T_{\rm td}$. This can also be translated in terms of orbital frequencies as $\Omega_\phi \ll \omega_\phi$. Generally, the stationary perturber approximation holds when a resonance takes place in the central BH's weak field regime. However, this approximation is violated when the perturber is too close to the central BH. Therefore we will have to model for the perturber's dynamics, which is accomplished in the next chapter.

2.3.3 Dynamic approach

We will now allow the perturber to move in a circular orbit in the equatorial plane. The orbital frequency of the perturber is given in Eq. (2.1.19). This slightly alters the perturbative expansion of the equations of motion in Eq. (2.3.5), because the tidal force terms are now also a function of Ω_ϕ. As we work in the framework of action-angle variables, this functional dependence is incorporated as a phase Q_ϕ, which relates to the perturber's orbital frequency as

$$\Omega_\phi = \frac{dQ_\phi}{dt}. \tag{2.3.11}$$

In order to compare this frequency with the fundamental frequencies of the EMRI's secondary mass, we define the perturber's orbital frequency with respect to proper time as

$$\tilde{\Omega}_\phi = \frac{dQ_\phi}{d\tau} = \Omega_\phi \frac{dt}{d\tau}. \tag{2.3.12}$$

The function $\frac{dt}{d\tau}$ is presented in the *KerrGeodesic* package of the BHPT [1] and can be determined from the roots of Eqs. (2.2.2a) and (2.2.3a). The adiabatic approximation still holds, and Eq. (2.3.6b) is now given by

$$\frac{dJ_i}{d\tau} \approx \epsilon \left\langle G_i^{(1)}(q_r, q_\theta, q_\phi, Q_\phi, \mathbf{J}) \right\rangle. \tag{2.3.13}$$

The angular torus is now spanned by four angles, so the angular brackets represent a four-dimensional averaging integral in this case. To calculate this integral we can perform a Fourier decomposition of the tidal force again, which now looks like

$$G_i^{(1)}(q_r, q_\theta, q_\phi, Q_\phi, \mathbf{J}) = \sum_{n,k,m,s} G_{i,nkms}^{(1)}(\mathbf{J}) e^{i(nq_r + kq_\theta + mq_\phi + sQ_\phi)}. \tag{2.3.14}$$

The solution representing the adiabatic approximation is given by $G_{i,0000}^{(1)}$, and is again suppressed in the weak field approximation. The post-adiabatic solutions correspond to the coefficients $G_{i,nkms}^{(1)}$ for which the set of integers (n,k,m,s) satisfies the dynamic resonance condition

$$\omega_{nkms} := n\omega_r + k\omega_\theta + m\omega_\phi + s\tilde{\Omega}_\phi = 0. \tag{2.3.15}$$

While it still holds that high order resonances are suppressed, this new resonance condition introduces new features. Firstly, it complements the stationary resonances in the weak field regime. Because we have that $\Omega_\phi \ll \omega_\phi$ in this region, we expect that the magnitude of the jumps in the orbital constants is only slightly altered in this case. However, the time when a resonance occurs differs in the dynamic and stationary models, which can have a measurable effect on the waveform of the GWs emitted by the EMRI. Secondly, it is also possible to explore resonances in the case where the perturber is placed closer to the central BH. Lastly, the dynamic model introduces a whole new class of resonances. In the case of prograde orbits, whose rotation is aligned with the rotation of the central BH, all fundamental frequencies are positive. Therefore at least one of the integers in the set (n,k,m) had to be negative for the stationary resonance condition to hold. If we consider a dynamic perturber, (n,k,m) can all be positive while s is negative. This gives rise to resonances where Ω_ϕ can in theory even be larger than the orbital frequencies of the EMRI's secondary mass.

2.4 Calculating the jump size

We will use the input from the previous subsections to determine the tidally induced jump sizes ΔC for $C \in \{L_z, Q\}$. We will follow the flowchart in Fig. 9. In order to calculate a jump size, the values of the set $\{a, e, x, n, k, m\}$ have to be specified beforehand. They will be substituted in the resonance condition to find the resonant value of the semi-latus rectum p. The set $\{a, p, e, x\}$ will then serve as input to determine the rate of change in C at the time of resonance. The jump's amplitude can subsequently be found using a semi-analytical averaging integral. Lastly, the jump size can be found by multiplying the amplitude with the duration of the tidal resonance and a total phase factor. These last two quantities have to be determined using a full numerical analysis. Finally we note that the diagram in Fig 9 is only presented for the stationary model. However, the diagram is completely similar in the dynamic model apart from some differences in notation.

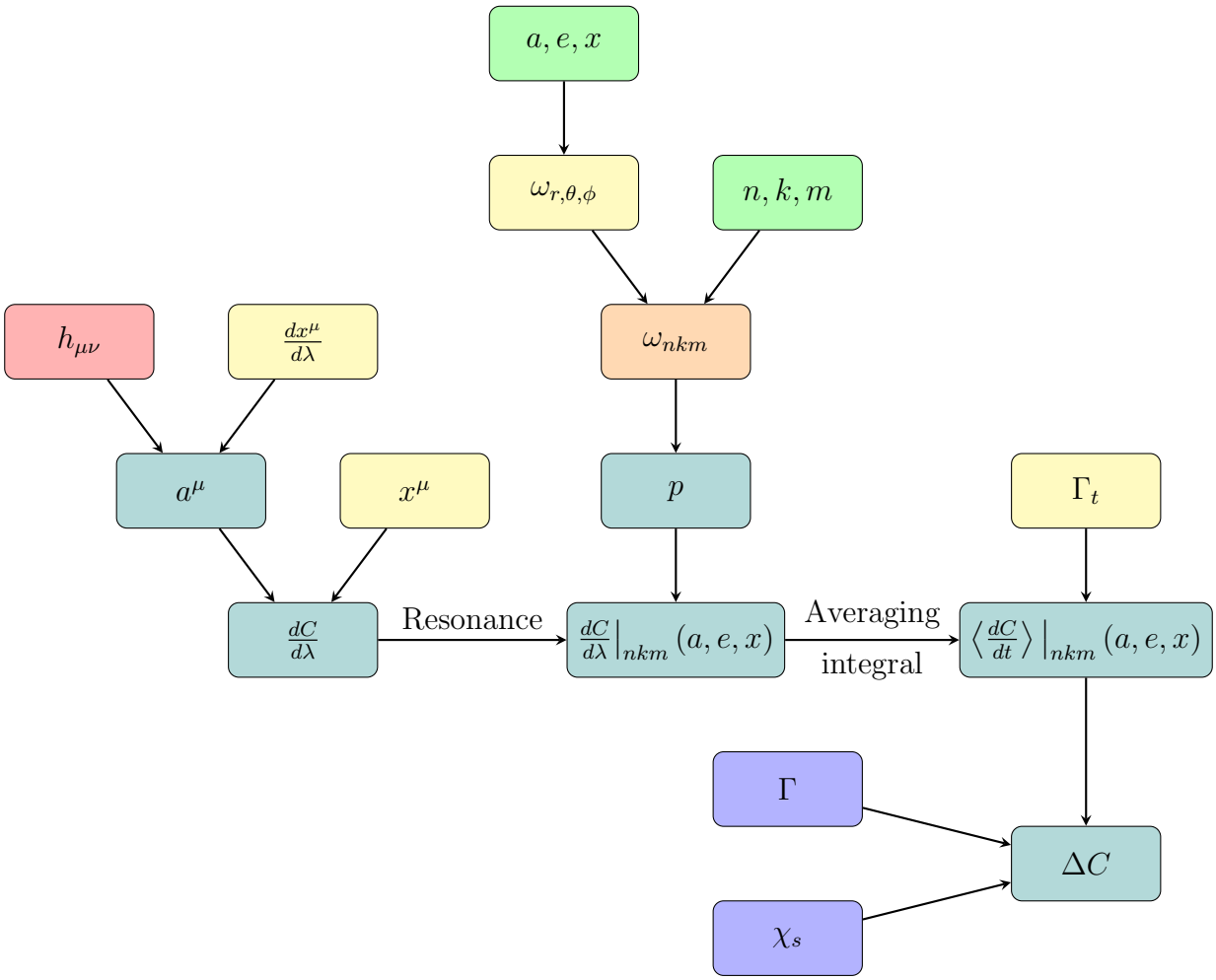

Figure 9: A flowchart describing the calculation of the tidally induced stationary jump size ΔC. The quantities in green have to be given as input for this calculation. The quantities in red, yellow and orange are the output of the flowcharts presented in Figs. 4, 6 and 8, respectively. The quantities in blue are found using a numerical analysis. This numerical method of osculating elements is discussed in section 3.1. We remark that these quantities in blue, as well as Γ_t, have to be taken at the time of resonance.

2.4.1 Stationary approach

We will first determine the jump sizes in L_z and Q based on a stationary metric perturbation. From Eq. (2.3.6b) we can estimate the change in the actions as [17]

$$\begin{aligned}\Delta J_i &\approx \epsilon \int_{-\infty}^{\infty} \left\langle G_i^{(1)}(q_\phi, q_\theta, q_\phi, \mathbf{J}) \right\rangle d\tau \\ &= \epsilon \sum_{j=\pm 1} \sqrt{\frac{2\pi}{|j\Gamma|}} \exp\left[\operatorname{sgn}(j\Gamma)\frac{i\pi}{4} + ij\chi_s\right] G^{(1)}_{i,jn,jk,jm}(\mathbf{J}).\end{aligned} \tag{2.4.1}$$

Here, Γ and χ_s are specified below Eq. (2.3.9). As discussed below Eq. (2.3.8) we will only take the dominant low order resonances into account by only summing over $j = \pm 1$. Because the combinations (n,k,m) and $(-n,-k,-m)$ will lead to the same resonant values of $\{a, p, e, x\}$ and therefore also to the same jump size, we will always take $n > 0$. For resonances with $n = 0$ we will take $k > 0$. The square root in Eq. (2.4.1) resembles the duration of the resonance, as becomes clear from Eq. (2.3.10), while the exponential term comes down to an overall phase factor. Hence, Eq. (2.4.1) is loosely translated as

$$\text{Jump size} \;=\; \text{resonance duration} \;\times\; \text{phase} \;\times\; \text{jump amplitude}. \tag{2.4.2}$$

The jump's amplitudes are characterized by the Fourier coefficients $G^{(1)}_{i,nkm}(\mathbf{J})$. These coefficients are determined by the evolution of the conserved quantities, which can be obtained from the acceleration in Kerr spacetime induced by the metric perturbation. This acceleration up to first order in the metric perturbation is derived in Appendix B and is given by

$$a^\alpha = -\frac{1}{2}\left(g^{\alpha\beta} + u^\alpha u^\beta\right)\left(2\nabla_\rho h_{\beta\lambda} - \nabla_\beta h_{\lambda\rho}\right) u^\lambda u^\rho + \mathcal{O}(h^2). \tag{2.4.3}$$

Here, $g_{\alpha\beta}$ is the Kerr metric and $h_{\alpha\beta}$ is the metric perturbation (see Eq. (2.1.1)). The covariant derivative ∇_ρ is compatible with the Kerr metric and u^α is the four-velocity of EMRI's secondary mass. The induced acceleration is completely determined by the metric perturbation, which can be constructed from the tidal fields as described in section 2.1. In the case of a stationary perturber, the electric quadrupole tidal field is given by $\mathcal{E}_{ab}(0)$ in Eq. (2.1.16a) and the magnetic quadrupole tidal field $\mathcal{B}_{ab}(t)$ vanishes, because $u = 0$. [22]

To find the evolution of L_z and Q, one simply takes the derivative with respect to proper time of their definitions as given above Eq. (2.2.1). This gives [53]

$$\frac{dL_z}{d\tau} = a_\phi, \tag{2.4.4a}$$

$$\frac{dQ}{d\tau} = 2u_\theta a_\theta - 2a^2\cos^2\theta u_t a_t + 2\cot^2\theta u_\phi a_\phi. \tag{2.4.4b}$$

The four-acceleration is given by Eq. (2.4.3), and the four-velocity is given by

$$u^\mu = \frac{dx^\mu}{d\tau} = \frac{dx^\mu}{d\lambda}\frac{d\lambda}{d\tau} = \frac{1}{\Sigma}\frac{dx^\mu}{d\lambda}, \tag{2.4.5}$$

where $\frac{dx^\mu}{d\lambda}$ is given by the equations of motion in Eq. (2.2.1). We can then obtain the Fourier coefficients by averaging over the rates in Eq. (2.4.4) by means of an inverse Fourier transform. If $C \in \{L_z, Q\}$, then

$$\left\langle \frac{dC}{dt} \right\rangle\Bigg|_{nkm} = \frac{1}{\Gamma_t(2\pi)^3}\int_0^{2\pi} dq_r \int_0^{2\pi} dq_\theta \int_0^{2\pi} dq_\phi \frac{dC}{d\lambda} e^{-i(nq_r + kq_\theta + mq_\phi)}. \tag{2.4.6}$$

Here, the rates of Eq. (2.4.4) are given with respect to Mino time. We have recovered the evolution of C with respect to Boyer-Lindquist coordinate time t by multiplying the standard inverse Fourier transform by Γ_t^{-1} [14]. In order for this formulation to work, the rates $\frac{dC}{d\lambda}$ have to be written in terms of the angles q_i. However, we have constructed these rates in terms of Boyer-Lindquist coordinates through the definitions of a^α and u^α. The solution to this problem is to write Eq. (2.4.6) in a complete Mino time formulation. Therefore we introduce three separate Mino times λ_i for $i \in \{r, \theta, \phi\}$, which relate to the angles q_i as

$$q_i = \frac{2\pi}{\Lambda_i}\lambda_i. \tag{2.4.7}$$

Here, Λ_i are the Mino-time periods. Λ_r and Λ_θ are defined in Eq. (2.2.4), while $\Lambda_\phi = \frac{2\pi}{\Gamma_\phi}$. This parametrization allows the Boyer-Lindquist coordinates to be written in terms of individual Mino times as well. Since the motion in r and θ is decoupled, the solutions to Eq. (2.2.1b) and Eq. (2.2.1c) are given by $r(\lambda_r)$ and $\theta(\lambda_\theta)$, respectively. The motion in ϕ in terms of Mino time was already presented in Eq. (2.2.5b). In terms of the individual Mino times, this equation can be rewritten as

$$\phi(\lambda_r, \lambda_\theta, \lambda_\phi) = \phi_\lambda^{(r)}(\lambda_r) + \phi_\lambda^{(\theta)}(\lambda_\theta) + \phi_\lambda^{(\phi)}(\lambda_\phi), \tag{2.4.8}$$

where $\phi_\lambda^{(\phi)}(\lambda_\phi) = \Gamma_\phi \lambda_\phi$, and for simplicity we have assumed that $\phi_0 = 0$. The analytical solutions of $r(\lambda_r)$, $\theta(\lambda_\theta)$, $\phi_\lambda^{(r)}(\lambda_r)$ and $\phi_\lambda^{(\theta)}(\lambda_\theta)$ are presented in sections 4.1 and 4.2 of [18]. These solutions are incorporated in the *KerrGeodesic* package of the BHPT [1] in terms of the central BH's dimensionless spin parameter a and the orbital parameters $\{p,e,x\}$.

Before we can perform the averaging integral, we have to specify the values of the set $\{a,p,e,x\}$ and we have to make sure that the orbit is on a resonance. Therefore we first determine our resonance of interest by stating the values of (n,k,m), after which we specify the values of $\{a,e,x\}$. Because the fundamental frequencies are a function of $\{a,p,e,x\}$, we can demand that we are on a resonance by solving the stationary resonance condition in Eq. (2.3.8) for p. The resulting set of parameters $\{a,p,e,x\}$ can then be inserted in $r(\lambda_r)$, $\theta(\lambda_\theta)$ and $\phi(\lambda_r, \lambda_\theta, \lambda_\phi)$, which in turn determine the rates $\frac{dC}{d\lambda}$. To state the dependence of the different parameters, we will denote the rates as $\frac{dC}{d\lambda}\big|_{nkm}(a, e, x)$ from this point on. To do the averaging integral of Eq. (2.4.6) in terms of Mino times, we perform a change of variables according to Eq. (2.4.7). We find

$$\begin{aligned}\left\langle \frac{dC}{dt} \right\rangle\Big|_{nkm}(a, e, x) = \\ \frac{1}{\Gamma_t \Lambda_r \Lambda_\theta \Lambda_\phi} \int_0^{\Lambda_r} d\lambda_r \int_0^{\Lambda_\theta} d\lambda_\theta \int_0^{\Lambda_\phi} d\lambda_\phi \frac{dC}{d\lambda}\Big|_{nkm}(a, e, x)\, e^{-i\left(n\frac{2\pi}{\Lambda_r}\lambda_r + k\frac{2\pi}{\Lambda_\theta}\lambda_\theta + m\frac{2\pi}{\Lambda_\phi}\lambda_\phi\right)}.\end{aligned} \tag{2.4.9}$$

The jumps ΔC are then determined by substituting these averaged rates for the Fourier coefficients $G^{(1)}_{i,nkm}(\mathbf{J})$ in Eq. (2.4.1).

2.4.2 Dynamic approach

If we consider the scenario where we include the perturber's dynamics at the time of resonance, Eq. (2.4.1) is slightly altered because the tidal force now also depends on the azimuthal phase of the perturber:

$$\begin{aligned}\Delta J_i &\approx \epsilon \int_{-\infty}^{\infty} \left\langle G_i^{(1)}(q_\phi, q_\theta, q_\phi, Q_\phi, \mathbf{J}) \right\rangle d\tau \\ &= \epsilon \sum_{j=\pm 1} \sqrt{\frac{2\pi}{|j\Gamma|}} \exp\left[\operatorname{sgn}(j\Gamma)\frac{i\pi}{4} + ij\chi_d\right] G^{(1)}_{i,jn,jk,jm,js}(\mathbf{J}).\end{aligned} \tag{2.4.10}$$

Here, $\chi_d = \chi_s + Q_{\phi 0}$ where $Q_{\phi 0}$ is the perturber's angular phase at the time of resonance. The resonance duration is not different in the case of a dynamic perturbation, as Γ does not change due to the fact that $\dot{\Omega}_\phi = 0$. The induced acceleration remains the same, except for the functional form of metric perturbation. This perturbation is now driven by the time-dependent quadrupole moments $\mathcal{E}_{ab}(t)$ and $\mathcal{B}_{ab}(t)$ as specified in Eq. (2.1.16). We will substitute $Q_\phi = \Omega_\phi t$ in these moments to model for the perturber's dynamics. The induced acceleration can then be substituted in Eq. (2.4.4) to obtain the rates in L_z and Q. Lastly we perform the averaging integral in terms of Mino times, analogous to the stationary case. However, we also have to average over the phase of the perturber, which results in a four-dimensional integral

$$\left\langle \frac{dC}{dt} \right\rangle \Big|_{nkms} (a,e,x) = \\ \frac{1}{2\pi\Gamma_t \Lambda_r \Lambda_\theta \Lambda_\phi} \int_0^{\Lambda_r} d\lambda_r \int_0^{\Lambda_\theta} d\lambda_\theta \int_0^{\Lambda_\phi} d\lambda_\phi \int_0^{2\pi} dQ_\phi \frac{dC}{d\lambda}\Big|_{nkms} (a,e,x)\, e^{-i\left(n\frac{2\pi}{\Lambda_r}\lambda_r + k\frac{2\pi}{\Lambda_\theta}\lambda_\theta + m\frac{2\pi}{\Lambda_\phi}\lambda_\phi + sQ_\phi\right)}. \tag{2.4.11}$$

These averaged rates are substituted for $G^{(1)}_{i,jn,jk,jm,js}(\mathbf{J})$ in Eq. (2.4.10) to find the dynamic jump sizes in L_z and Q.

2.4.3 Efficient jump calculations

Up to this point, our analysis has been purely analytical. However, the averaging integrals in Eqs. (2.4.9) and (2.4.11) are too complicated to do analytically, because the radial and polar functions depending on λ_r and λ_θ involve elliptical integrals. Therefore we have to perform the averaging integrals numerically. We specify the accuracy of a single integral by a given number n_s, which corresponds to the total number of integration steps in each single integral. Consequently, the size of each integration step is given by $\Delta\lambda_i = \frac{\Lambda_i}{n_s}$ for the integrals over the Mino times and by $\Delta Q_\phi = \frac{2\pi}{n_s}$ for the integral over the azimuthal phase of the perturber. This means that the computational costs in Eq. (2.4.9) scale with n_s^3 while they scale with n_s^4 in Eq. (2.4.11). Concretely, the dynamic jump calculation would take n_s times as long as a stationary jump calculation. Motivated by this difference, we found a faster way to compute the averaging integrals by splitting them in an analytical and a numerical part. We will show this for the dynamic case, as this analysis can then be easily adapted to the stationary case.

The functional dependence of the rates $\frac{dC}{d\lambda}\big|_{nkms}$ on λ_ϕ and Q_ϕ is not so complicated that we have to resort to numerical integration to perform the integrals over these two variables. The only dependence on λ_ϕ resides in Eq. (2.4.8) and can easily be rewritten as

$$\phi^{(\phi)}_\lambda(\lambda_\phi) = \Gamma_\phi \lambda_\phi = \frac{2\pi}{\Lambda_\phi}\lambda_\phi \overset{2.4.7}{=} q_\phi. \tag{2.4.12}$$

Hence we rewrite Eq. (2.4.11) as

$$\left\langle \frac{dC}{dt} \right\rangle \Big|_{nkms} (a,e,x) = \\ \frac{1}{(2\pi)^2 \Gamma_t \Lambda_r \Lambda_\theta} \int_0^{\Lambda_r} d\lambda_r \int_0^{\Lambda_\theta} d\lambda_\theta \int_0^{2\pi} dq_\phi \int_0^{2\pi} dQ_\phi \frac{dC}{d\lambda}\Big|_{nkms} (a,e,x)\, e^{-i\left(n\frac{2\pi}{\Lambda_r}\lambda_r + k\frac{2\pi}{\Lambda_\theta}\lambda_\theta\right)} z^{-m} y^{-s}. \tag{2.4.13}$$

Here, the dependence on the azimuthal angles is written as exponential functions $z = e^{iq_\phi}$ and $y = e^{iQ_\phi}$. The rates can also be written in terms of z and y as

$$\frac{dC}{d\lambda}\Big|_{nkms} (a,e,x) = \sum_{-2\le\mu,\sigma\le 2} A_{nk\mu\sigma} z^\mu y^\sigma, \tag{2.4.14}$$

where $A_{nk\mu\sigma}$ are functions of λ_r and λ_θ. The sum in μ and σ runs from -2 to 2, as the metric perturbation is constructed from the quadrupole tidal potentials only, which consist of the $l = 2$ spherical harmonics. This formulation of the rates in Eq. (2.4.14) decouples the four-dimensional integral of Eq. (2.4.13) into a double integral over λ_r and λ_θ and two single integrals over q_ϕ and Q_ϕ. These two single integrals can be performed by making use of the standard integral

$$\frac{1}{2\pi}\int_0^{2\pi} e^{iax}dx = \begin{cases} 1 & \text{if } a = 0 \\ 0 & \text{if } a \in \mathbb{Z}/\{0\}. \end{cases} \tag{2.4.15}$$

The two integrals over the azimuthal angles in Eq. (2.4.13) are then calculated as

$$\begin{aligned} \frac{1}{(2\pi)^2}\int_0^{2\pi} dq_\phi \int_0^{2\pi} dQ_\phi \left.\frac{dC}{d\lambda}\right|_{nkms}(a,e,x)\, z^{-m} y^{-s} & \\ \overset{2.4.14}{=} \frac{1}{(2\pi)^2} \sum_{-2\leq\mu,\sigma\leq 2} A_{nk\mu\sigma} \int_0^{2\pi} z^{\mu-m} dq_\phi \int_0^{2\pi} y^{\sigma-s} dQ_\phi & \\ \overset{2.4.15}{=} A_{nkms}. & \end{aligned} \tag{2.4.16}$$

Because the values of the set (n,k,m,s) are specified beforehand, we do not have to perform the two integrals over the azimuthal angles, as these integrals evaluate to the function A_{nkms}. The remaining part of the averaging integral then has to be done numerically:

$$\left\langle \frac{dC}{dt} \right\rangle \Bigg|_{nkms}(a,e,x) = \frac{1}{\Gamma_t \Lambda_r \Lambda_\theta} \int_0^{\Lambda_r} d\lambda_r \int_0^{\Lambda_\theta} d\lambda_\theta \; A_{nkms}\, e^{-i\left(n\frac{2\pi}{\Lambda_r}\lambda_r + k\frac{2\pi}{\Lambda_\theta}\lambda_\theta\right)}. \tag{2.4.17}$$

Because the computational costs of this integral only scale with n_s^2, this integral is calculated $n_s^{4-2} = n_s^2$ times faster than the four-dimensional integral in Eq. (2.4.11). A similar analysis holds for the stationary scenario, where the computational costs can be reduced by a factor of n_s. In this case, the rates can be written as

$$\left.\frac{dC}{d\lambda}\right|_{nkm}(a,e,x) = \sum_{-2\leq\mu\leq 2} A_{nk\mu} z^\mu, \tag{2.4.18}$$

which leads to the stationary averaging integral

$$\left\langle \frac{dC}{dt} \right\rangle \Bigg|_{nkm}(a,e,x) = \frac{1}{\Gamma_t \Lambda_r \Lambda_\theta} \int_0^{\Lambda_r} d\lambda_r \int_0^{\Lambda_\theta} d\lambda_\theta \; A_{nkm}\, e^{-i\left(n\frac{2\pi}{\Lambda_r}\lambda_r + k\frac{2\pi}{\Lambda_\theta}\lambda_\theta\right)}. \tag{2.4.19}$$

Additionally, one can reduce the computational costs of the stationary jump calculations by almost 50% by making use of the so-called two-for-one deal. As stated in a recent paper by Gupta et al. [23], the jumps in L_z and Q are related by

$$\frac{dQ}{dt} = \frac{\frac{\pi a k}{m}\sqrt{1-E^2}\, y_+ - 2L_z\left(K\left[\left(\frac{y_-}{y_+}\right)^2\right] - \Pi\left[y_-^2, \left(\frac{y_-}{y_+}\right)^2\right]\right)}{K\left[\left(\frac{y_-}{y_+}\right)^2\right]} \frac{dL_z}{dt}, \tag{2.4.20}$$

provided that $m \neq 0$. Here, $y_\pm = \cos\theta_\pm$, where $\theta_\pm$ are the zeroes of $\Theta(\theta)$ in Eq. (2.2.3a), and $y_+ > y_-$. This expression also involves elliptical integrals of the first and second kind, denoted as $K[m]$ and $\Pi[n,m]$ respectively. Hence, the jumps in Q can also be determined from the jumps in L_z at low computational costs.

3 Results

3.1 Osculating orbital elements method

We will use the method of forced osculating orbital elements to perform a consistency check on the semi-analytical calculations of the jumps in the constants of motion. Using this method, the equations of motion in the perturbed Kerr spacetime can be integrated numerically as long as the orbital motion is bounded. Osculating orbits are reference geodesics tangent to the worldline of the EMRI's secondary mass. These geodesics are characterized by a set of constants, referred to as orbital elements. The orbit's motion is determined by the change in the osculating orbits, which in turn is governed by the evolution of the orbital elements [40]. This evolution is driven by the radiation reaction, which causes the orbit's adiabatic inspiral, and the perturber's tidal force, which is completely determined by the metric perturbation $h_{\mu\nu}$. The radiation reaction is determined by post-Newtonian radiation fluxes. These fluxes describe the rate of change of the orbital parameters due to the dissipative piece of the gravitational self-force up to 5PN order and tenth order in the eccentricity [19]. Analytical expressions of the radiation fluxes can be found in [43, 55]. In order to compute the numerical jumps in the constants of motion, we use the already existing osculating elements code as used in previous research [22, 24], which is a modified version of the code used in the 'gas-drag' problem in [20]. In the dynamic model, we made some minor changes to account for the perturber's dynamics.

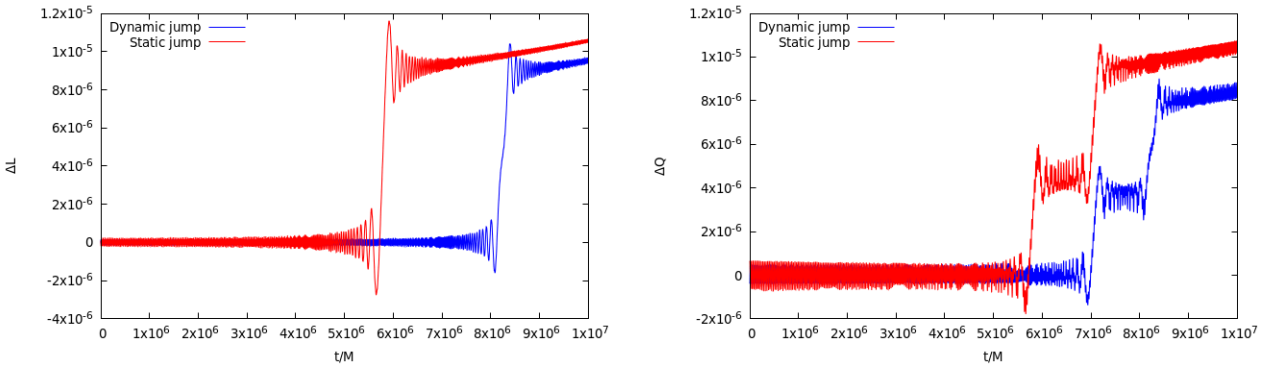

(a) The difference in L_z caused by a tidal perturber. (b) The difference in Q caused by a tidal perturber.

Figure 10: The effect on an EMRI's orbital constants L_z and Q caused by a tidal perturber with mass $M_* = 30M_\odot$ at a distance $b = 10\,\mathrm{AU}$ from the EMRI's central BH with mass $M = 4\times10^6 M_\odot$. The orbit's initial conditions are given by $\{a, p, e, x\} = \{0.1M, 7M, 0.6, \cos 20°\}$ and the EMRI's mass ratio corresponds to $\eta = 7.5 \times 10^{-6}$. The orbit crosses the $(3, 0, -2)$-tidal resonance at $t = 5.78M$ in the stationary model and at $t = 8.24M$ in the dynamic model. The $(3, -2, 0)$-tidal resonance is crossed at $t = 7.05M$ in both models.

The influence of the tidal perturber on the EMRI's secondary mass can be determined by taking the difference of a full trajectory, constructed from both radiation fluxes and the tidal force, and a trajectory consisting of radiation effects only. Both trajectories have to be specified by the same set of initial conditions. Examples of the effect of the tidal perturber on the orbit's constants of motion are shown in Figs. 1 and 10. The jumps in ΔL_z and ΔQ occur when the orbit is on a tidal resonance. The static jumps are calculated using a stationary metric perturbation, while the dynamic jumps are the result of a dynamic metric perturbation. The fast oscillations in Figs. 1 and 10 correspond to the timescales associated with the orbital motion. These oscillations are 'averaged out', as discussed below Eq. (2.3.7), and do not induce a secular change in the orbit's constants of motion. However, after the orbit has experienced a resonance, the orbital evolution is altered, because the orbital constants of motion now have different values. As a result, ΔL_z and

ΔQ tend to increase or decrease after a resonance crossing, rather than evolve around a constant value. Therefore the GWs emitted by the EMRI can suffer from significant dephasing after a tidal resonance is encountered. While the osculating elements method is a powerful tool to study tidal resonance effects, it is rather slow and computationally expensive. Therefore it is not well suited for the data analysis of GW measurements by LISA. The semi-analytical analysis, on the other hand, allows for computationally inexpensive calculations of the tidally induced jumps in the orbit's constants of motion. Hence, we will only use the osculating elements method to verify the semi-analytical results.

3.2 Stationary model

3.2.1 Fitting formulas

In this section we will discuss the jumps in L_z and Q obtained from the semi-analytical analysis based on a stationary metric perturbation. No jump in E is induced, because the tidal perturbation is considered to be stationary when a tidal resonance is encountered [53]. As mentioned above Eq. (2.4.9), the values of the integers (n,k,m) as well as the set $\{a,e,x\}$ have to be specified beforehand in order to calculate the jump's amplitude. As a, e and x are all bounded, the whole parameter space can be surveyed for a given resonance. Therefore we compute jumps for $a/M \in [0.1, 0.5, 0.9]$, $e \in [0.10, 0.15, \cdots, 0.80, 0.85]$ and $I \in [1°, 5°, 10°, \cdots, 80°, 85°, 89°]$ where $x = \cos I$. We only consider prograde orbits for which L_z is positive, leading to the range $0° \leq I \leq 90°$ according to Eq. (2.2.10c). Using all these jumps we make a polynomial ansatz for the jump's amplitude in terms of a, e and x, which we will refer to as a fitting formula. These fitting formulas can then be used to determine the jump size at low computational costs for arbitrary $\{a,e,x\}$. A similar analysis can be performed for retrograde orbits, which rotate in the opposite direction compared to the central BH and have orbital inclination angles in the range $90° \leq I \leq 180°$. The jump size due to a tidal resonance in a retrograde orbit will be somewhat larger than a jump in a prograde orbit, because these resonances occur at larger p values. Here, the radiation reaction is slower compared to regions closer to the central BH. Consequently, the resonance duration will be longer, leading to larger jump sizes. [24]

We have calculated jumps using the triple numerical integral in Eq. (2.4.9) and the faster integral in Eq. (2.4.19), where we specified the accuracy of a single integral to $n_s = 60$. Both methods give equivalent results, while the faster integration method reduced the computational time by a factor between 20 and 50, depending on intrinsic parameters. We have also checked the two-for-one deal by calculating jumps in Q using Eq. (2.4.20). The jump sizes obtained from this method match with the jump sizes obtained from the other integration methods within the range of 0.1%.

Fitting formulas for the tidal resonance with $(n,k,m)=(3,0,-2)$ are given in Appendix C. Eqs. (C.1.1) and (C.1.2) are calculated from a Schwarzschild-like metric perturbation, as discussed in section 2.1. Eqs. (C.2.1) and (C.2.2) are based on a metric perturbation in Kerr spacetime, which is constructed using the Teukolsky equation and the metric reconstruction procedure as discussed in [22, 24]. We have constructed the fitting formulae for the change in L_z for a lower polynomial order than the formulae for the change in Q, such that each fitting coefficient in Eq. (C.1.1) can be directly compared to its counterpart in Eq. (C.2.1). A scan across the whole parameter space shows that the Kerr and Schwarzschild fitting formulas generally only differ by less than 0.1%. An exception are highly eccentric orbits, where this difference maximally equals 1.0%. This observation also holds for other resonances. Hence, the effect of the central BH's spin only has a small effect on the metric perturbation in the weak-field approximation. It is also much more feasible to calculate the tidally induced jump amplitudes based on a Schwarzschild-like metric perturbation. Concretely, the calculation of the perturbation in the metric took approximately 15 times as long using Kerr perturbation theory in comparison to its Schwarzschild counterpart.

3.2.2 Resonance characterization

We only encounter tidal resonances with m ranging from -2 to 2, because the metric perturbation is constructed in terms of quadrupolar tidal moments corresponding to $l = 2$ modes. In practice, we merely find resonances with $m \in \{-2, 0, 2\}$ in the equatorial plane. This can be explained from the functional form of the harmonic components of the electric tidal potential, displayed in the right column of Table 1. The electric quadrupole moment in Eq (2.1.16a) only has diagonal entries, causing the potential's components $\mathcal{E}^{\mathrm{q}}_{1c}$, $\mathcal{E}^{\mathrm{q}}_{1s}$ and $\mathcal{E}^{\mathrm{q}}_{2s}$ to vanish. These components correspond directly with the values of m. As both $m = 1$ components vanish in the equatorial plane, we do not find resonances with $m = \pm 1$. If the perturber is not situated on the equatorial plane, the electric quadrupole moment will have off-diagonal entries, which will allow $m = \pm 1$ resonances to manifest. This will be discussed in more detail in section 3.2.4.

The tidal force is ϕ-independent for tidal resonances with $m = 0$. Consequently, the axisymmetry of the Kerr spacetime is preserved during such resonances. As a result, no jump in L_z is induced. There does occur a jump in Q, which still can lead to significant dephasing of the gravitational waveform. Additionally, $m = 0$ tidal resonances are degenerate with self-force resonances, which occur if only the radial and polar orbital frequencies become commensurate. Both resonances occur at the same time, and only differ by their respective driving force. In order to distinguish tidal and self-force resonances, one has to correctly implement both types of resonances when modeling for the EMRI waveform.

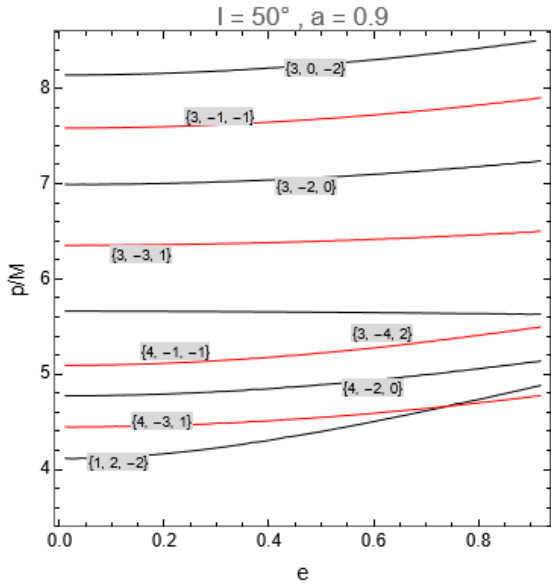

Figure 11: Resonance contour of low order stationary resonances for $a = 0.9M$ and $x = \cos 50°$. The stationary resonance condition of Eq. (2.3.8) is satisfied at each line. The set of numbers corresponds to the values of the set $\{n, k, m\}$. An orbit in the equatorial plane only encounters the resonances displayed by a black line. If the orbit has an arbitrary configuration in the sky, it can cross both black and red resonances.

The EMRI's secondary mass can experience several tidal resonances during the inspiral, as can be seen in Fig. 11. This figure displays a resonance contour in the (e,p)-plane for an orbital inclination of $x = \cos 50°$ and a value of the central BH's spin of $a = 0.9M$. The lines denote when the stationary resonance condition of Eq. (2.3.8) is satisfied for the corresponding values of the set $\{n, k, m\}$. The resonance contour shows all low order resonances for $n, k \in \{-4, 4\}$ and $m \in \{-2, 2\}$, except for resonances for which $k + m =$ odd. That's because in the stationary model, only tidal resonances with $k + m =$ even contribute to shifts in L_z and Q. This statement

is referred to as a 'selection rule'. If the perturber is situated on the equatorial plane, tidal resonances with $m = \pm 1$ are not encountered, meaning that an orbit only encounters resonances with $k =$ even. The derivation of both selection rules will be given in Appendix D.

The value of p decreases during the adiabatic inspiral. As a result, the orbit crosses all the resonances displayed in the resonance contour. However, an orbit can also pass through a resonance without actually feeling the resonance effect. If we work out the sum in Eq. (2.4.1), we find that the jump size has a sinusoidal dependence on the total phase, with which it enters the resonance. Therefore, the EMRI's secondary mass does not notice that it is on a resonance if its phase equals zero.

3.2.3 Comparing analytical and numerical results

The jumps as calculated using the semi-analytical analysis can be compared to the numerical jumps obtained by the osculating elements method. In Figs. 12 and 13 we compare the stationary jumps in L_z and Q for the $(3, 0, -2)$-tidal resonance. In these figures, the horizontal lines denote the jump sizes as calculated using the semi-analytical analysis. In order to determine these jumps, the values of a, e and x are taken at the resonance and are subsequently substituted in Eqs. (C.1.1) and (C.1.2) to obtain the jump's amplitude. This gives the maximal jump size.

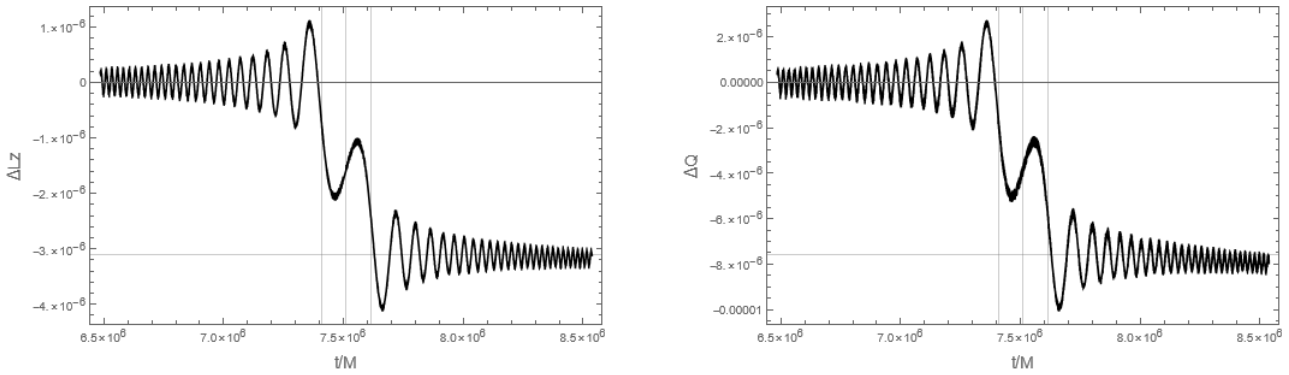

(a) $\Delta L_z = -3.1909 \times 10^{-6}$. (b) $\Delta Q = -7.59287 \times 10^{-6}$.

Figure 12: A closer look at the stationary jumps in L_z and Q in Fig. 1.

To match with the numerical results, we also need the phase at the moment of resonance. This is calculated by numerically integrating the stationary resonance condition

$$\chi_s = \int_0^{t_0} (n\omega_r(t) + k\omega_\theta(t) + m\omega_\phi(t))\, dt, \tag{3.2.1}$$

where t_0 is the time of resonance and the orbital frequencies are now a function of Boyer-Lindquist time t. The phases modulo 2π correspond to $\chi_s = 3.47$ for Fig. 12 and $\chi_s = 4.67$ for Fig. 13. The rate of change of the orbital frequencies (Γ) is also determined with respect to t, and is negative in both cases. Therefore the total phase dependence is given by $2\sin(\frac{\pi}{4} - \chi_s)$. As the sign of this factor differs for the jumps in Figs. 12 and 13, the jumps are positive in one figure and negative in the other. The outer vertical lines in both figures denote the duration of the resonance, as calculated using Eq. (2.3.10), while the value of t_0 is marked by the middle vertical line. The analytical jump sizes are given below each figure. They match with the jump sizes obtained from the osculating code, as can be clearly seen from both figures.

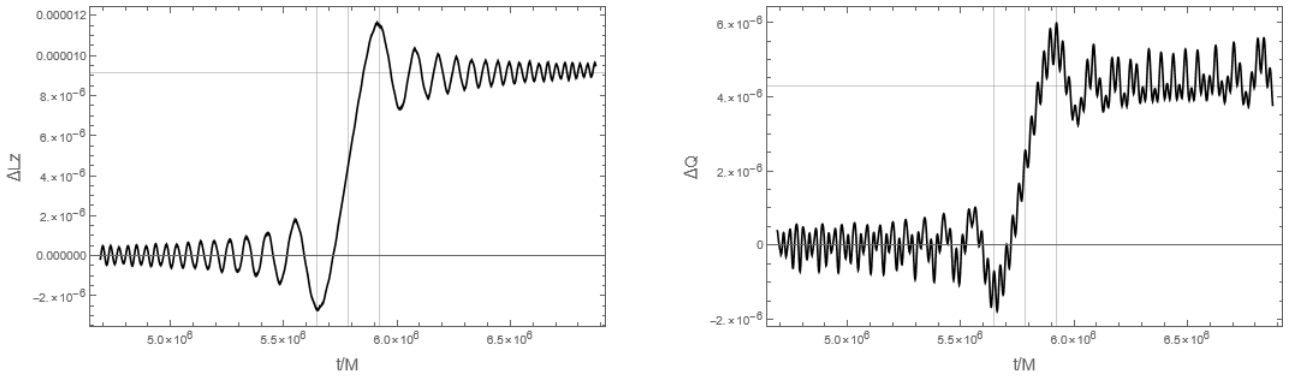

(a) $\Delta L_z = 9.12761 \times 10^{-6}$. (b) $\Delta Q = 4.28646 \times 10^{-6}$.

Figure 13: A closer look at the stationary jumps in L_z and Q in Fig. 10, corresponding to the $(3, 0, -2)$-resonance.

Fig. 14 zooms in on the $(3, -2, 0)$-tidal resonance of Fig. 10. No jump in L_z is induced because $m = 0$. The vertical axis is rescaled with the jump in Q of the $(3, 0, -2)$-resonance, since in the stationary model this resonance is encountered earlier in the inspiral. Because the orbital evolution is altered after the $(3, 0, -2)$-resonance, the trajectory is not perfectly oscillating around the rescaled horizontal axis before the $(3, -2, 0)$-resonance is encountered. As a consequence, the numerical results do not perfectly match with the semi-analytical results in this case.

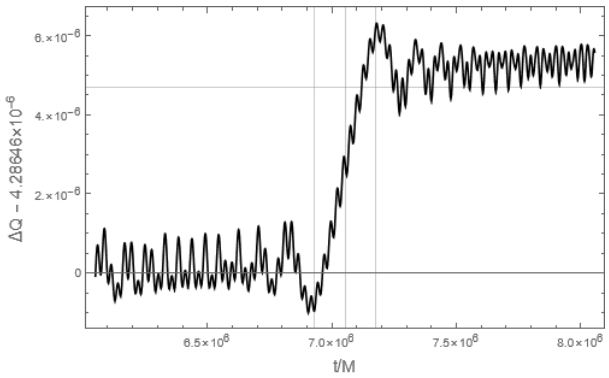

Figure 14: A closer look at the stationary jump in Q in Fig. 10, corresponding to the $(3, -2, 0)$-resonance. The vertical axis is shifted, because the orbit crosses the $(3, 0, -2)$-resonance earlier in the inspiral. The phase at the resonance is given by $\chi_s \mod 2\pi = 1.83$ and the jump size obtained from the semi-analytical analysis is given by $\Delta Q = 4.68096 \times 10^{-6}$.

3.2.4 General sky location of the perturber

If we want to study tidal resonance effects caused by a perturber that is not situated on the x-axis, we have to rotate our tidal field by two angles θ_y and θ_z, where $\theta_{y/z}$ describes a rotation around the y/z-axis. The rotated electric quadrupole moment then has the functional form

$$\mathcal{E}_{ab}(t, \theta_y, \theta_z) = R_z(\theta_z) R_y(\theta_y) \mathcal{E}_{ab}(t) R_y(\theta_y)^T R_z(\theta_z)^T. \tag{3.2.2}$$

Here, $\mathcal{E}_{ab}(t)$ is the electric quadrupole moment in the equatorial plane, as given in Eq. (2.1.16a). $R_y(\theta_y)$ and $R_z(\theta_z)$ are rotation matrices given by

$$R_y(\theta_y) = \begin{pmatrix} \cos\theta_y & 0 & \sin\theta_y \\ 0 & 1 & 0 \\ -\sin\theta_y & 0 & \cos\theta_y \end{pmatrix}, \qquad R_z(\theta_z) = \begin{pmatrix} \cos\theta_z & -\sin\theta_z & 0 \\ \sin\theta_z & \cos\theta_z & 0 \\ 0 & 0 & 1 \end{pmatrix}, \tag{3.2.3}$$

where $\theta_y \in [-\frac{\pi}{2}, \frac{\pi}{2}]$ and $\theta_z \in [0, 2\pi)$. The perturber is on the x-axis when $\theta_y = \theta_z = 0$. The perturber can now be situated at an arbitrary position in the sky, as can be seen in Fig. 15. As we deal with a stationary perturber, we substitute $t = 0$ in Eq. (3.2.2) and use this tidal moment to determine the metric perturbation. The jumps in the constants of motion are then also a function of the perturber's inclination angles and can subsequently be calculated using a similar analysis as in the equatorial plane.

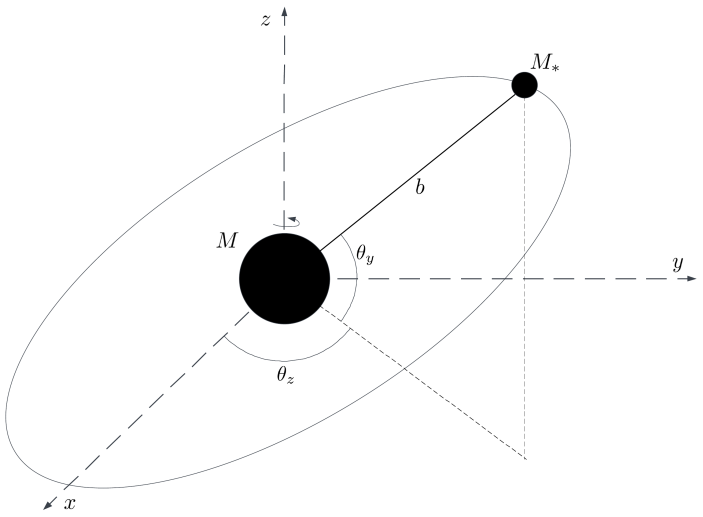

Figure 15: A sketch of an EMRI, whose central BH is of mass M, in the vicinity of a tidal perturber of mass M_*. The EMRI's secondary mass is not shown for illustrative purposes. The spin axis of M coincides with the z-axis, and the (x, y)-plane is denoted as the equatorial plane. The tidal perturber is situated on a distance b from M and is rotated by the angles θ_y and θ_z as compared to the situation sketched in Fig 3. In the dynamic model, the perturber is allowed to move in a circular orbit of radius b.

In previous research [24], only rotations around the y-axis were considered, and the functional dependence on the rotation angle was determined by fits. We found analytical expressions of the functional dependence on both rotation angles by analyzing the functional form of the jump amplitude. In the case of a rotated tidal field, Eq. (2.4.18) is given by

$$\begin{aligned}\left.\frac{dC}{d\lambda}\right|_{nkm}(a,e,x,\theta_y,\theta_z) &= A_{nk-2}\, z^{-2} e^{2\theta_z} \cos^2\theta_y + A_{nk-1}\, z^{-1} e^{\theta_z} \sin 2\theta_y \\ &\quad + \frac{1}{2} A_{nk0}\,(3\cos 2\theta_y - 1) + A_{nk1}\, z\, e^{-\theta_z} \sin 2\theta_y + A_{nk2}\, z^2 e^{-2\theta_z} \cos^2\theta_y \\ &\equiv \sum_{-2\leq\mu\leq 2} A_{nk\mu} z^\mu e^{-\mu\theta_z} f_\mu(\theta_y),\end{aligned} \tag{3.2.4}$$

where in the last step we incorporated the functions of θ_y as $f_\mu(\theta_y)$, which are given in Tab. 4. This equation tells us that the functional dependence on the perturber's inclination angles is completely determined by the value of m, since the averaging integral of Eq. (2.4.19) is now given by

$$\begin{aligned}\left\langle\frac{dC}{dt}\right\rangle\Big|_{nkm}(a,e,x,\theta_y,\theta_z) &= \frac{1}{\Gamma_t\Lambda_r\Lambda_\theta}\int_0^{\Lambda_r} d\lambda_r \int_0^{\Lambda_\theta} d\lambda_\theta\; A_{nkm}\; e^{-m\theta_z} f_m(\theta_y)\; e^{-i\left(n\frac{2\pi}{\Lambda_r}\lambda_r + k\frac{2\pi}{\Lambda_\theta}\lambda_\theta\right)} \\ &= \left\langle\frac{dC}{dt}\right\rangle\Big|_{nkm}^{\theta_m}(a,e,x)\, e^{-m\theta_z} f_m(\theta_y).\end{aligned} \tag{3.2.5}$$

Here, $\left\langle\frac{dC}{dt}\right\rangle|_{nkm}^{\theta_m}(a,e,x)$ is the jump amplitude in C calculated for $\theta_z = 0$ and $\theta_y = \theta_m$, which is a fixed reference angle. Logically, one takes $\theta_m = 0$. We cannot always do this, however, as some jump amplitudes always vanish in this case. For example, $f_{\pm1}(\theta_m) = 0$ for $\theta_m = 0$, which causes the $m = \pm1$ jump amplitudes to vanish at all times. Therefore the values of θ_m have to be specified for each value of m. This is shown in Table 4, in combination with with the functions $f_m(\theta_y)$. There are only three distinct functions, since $f_m(\theta_y) = f_{-m}(\theta_y)$. All three coincide with the functions as obtained by fits in [24]. It is possible to choose another reference angle $\tilde{\theta}_m$ instead of θ_m, as long as $f_m(\tilde{\theta}_m) \neq 0$ for the given value of m. In this case, the total jump amplitude will be given as

$$\left\langle\frac{dC}{dt}\right\rangle\Big|_{nkm}(a,e,x,\theta_y,\theta_z) = \frac{1}{f_m(\tilde{\theta}_m)}\left\langle\frac{dC}{dt}\right\rangle\Big|_{nkm}^{\tilde{\theta}_m}(a,e,x)\, e^{-m\theta_z} f_m(\theta_y). \tag{3.2.6}$$

The dependence on θ_z is always given by an exponential. Therefore, from now on, we will include it as an additional phase dependence rather than an amplitude. The total phase of the jumps in L_z and Q will then be given as $2\sin\left(\pm\frac{\pi}{4} - \chi_s + m\theta_z\right)$.

m	θ_m	$f_m(\theta_y)$
-2	0	$\cos^2\theta_y$
-1	$\pi/4$	$\sin 2\theta_y$
0	0	$\frac{1}{2}(3\cos 2\theta_y - 1)$
1	$\pi/4$	$\sin 2\theta_y$
2	0	$\cos^2\theta_y$

Table 4: The functional dependence of the jumps on θ_y in the case of a stationary perturber.

3.2.5 Impact on gravitational waveform

The orbital evolution of the secondary EMRI mass is altered after the passing of a resonance. It becomes out of phase as compared to the pre-resonance evolution. As a result, there occurs a shift in the orbital phases. This in turn causes a deviation in the GW phases. The total phase shift induced by one resonance from the resonance time until the secondary plunges into the central BH is

$$\Delta\Psi_i = 2\int_{t_0}^{t_{plunge}} \Delta\omega_i \, dt \tag{3.2.7}$$

for $i \in (r, \theta, \phi)$. Here, $\Delta\omega_i$ are the shifts in the orbital frequencies, as caused by the change in the orbital's constants of motion due to a tidal resonance. The integration is performed from the resonance time t_0 up to the plunge time t_{plunge}. So even if a tidal resonance induces a relatively small change in the orbital constants of motion, the gravitational waveform can become significantly dephased if a resonance is crossed early in the inspiral. The phase shifts in the gravitational waveform can be measured by LISA if $\Delta\Psi_\phi \geq 0.1$, if we assume a signal-to-noise ratio of 20 [28, 47]. Phase contours of the $(3, 0, -2)$-tidal resonance are displayed in Fig. 16 for different values of the spin parameter a. They are constructed by taking $M = 4 \times 10^6 M_\odot$, $\mu = M_* = 30 M_\odot$, $b = 10\,\mathrm{AU}$ and $\theta_y = 0$. They show that the phase shifts in the waveform caused by this resonance can all be detected by LISA for these parameters, except for orbits with $e < 0.2$.

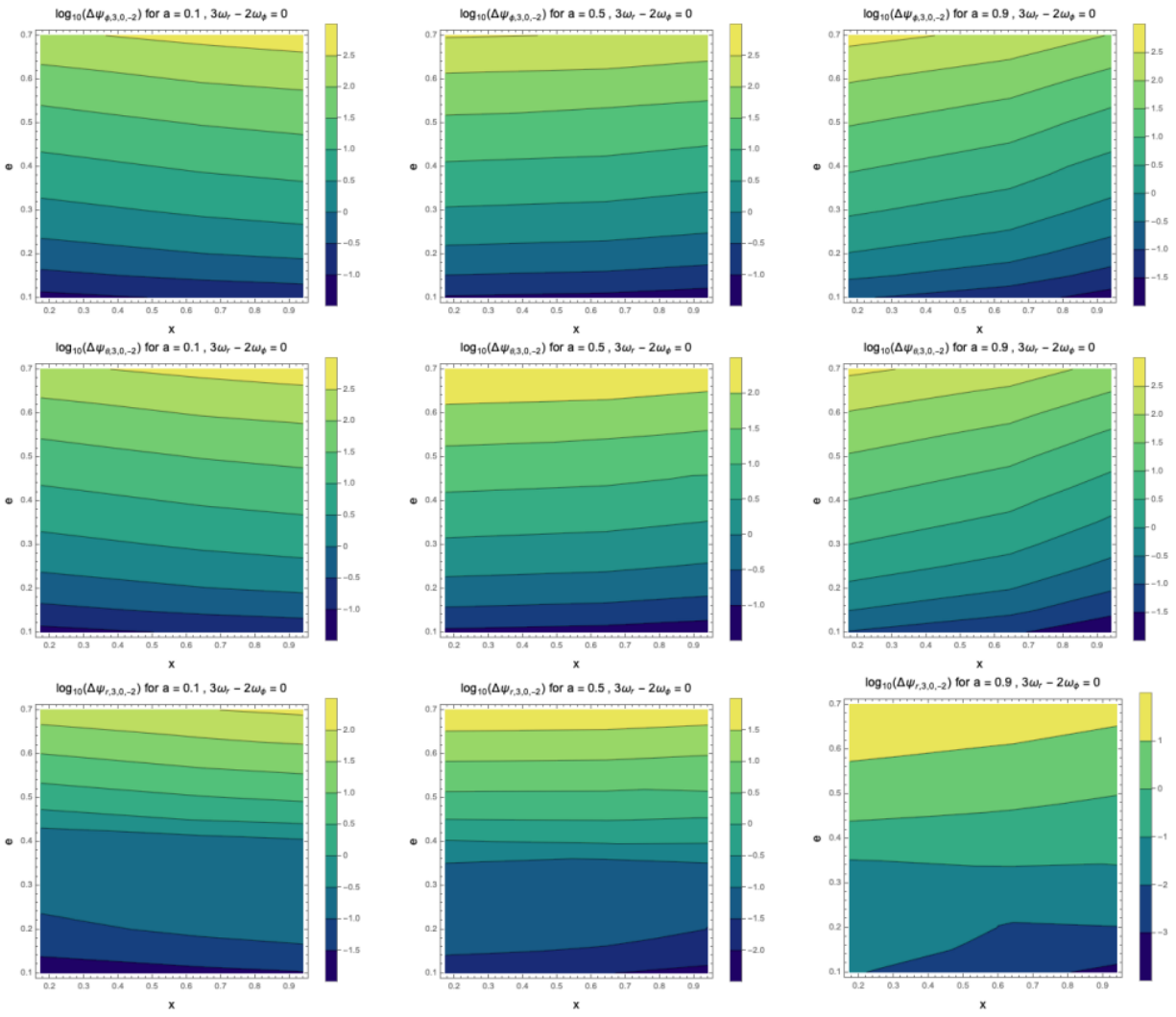

Figure 16: Phase contours in the (x, e)-plane displaying the phase shifts $\Delta\Psi_i$ in the gravitational waveform caused by the crossing of the $(3, 0, -2)$-tidal resonance. Figure adapted from [22].

Throughout our whole analysis we have assumed fixed values for the three masses M, μ and M_*. The position of the perturber is determined by the distance b to the central BH and the inclination angle θ_y, which both have to be specified beforehand as well. The accumulated phase shifts $\Delta\Psi_i'$ for a different set of parameters $\{M', \mu', M_*', b', \theta_y'\}$ can be easily obtained from the scaling relation

$$\Delta\Psi_i' = \Delta\Psi_i \left(\frac{M'}{M}\right)^{\frac{7}{2}} \left(\frac{\mu'}{\mu}\right)^{-\frac{3}{2}} \left(\frac{M_*'}{M_*}\right) \left(\frac{b'}{b}\right)^{-3} \left(\frac{f_m(\theta_y')}{f_m(\theta_y)}\right). \tag{3.2.8}$$

The phase evolution of the gravitational waveform depends on all three phases Ψ_i. Shifts in each of these phases can lead to significant dephasing of the GWs radiated by the EMRI. Fig 17 displays two h_+ snapshots of EMRI waveforms during the last hours of the inspiral. Tidal effects are neglected in the construction of the red waveform, while the green waveform is constructed from a trajectory that crosses one tidal resonance in its inspiral. Directly after the resonance crossing, both waveforms only slightly differ. This difference, however, increases after each orbital revolution. Therefore, after many orbits, a significant mismatch appears between both waveforms. Furthermore, the orbit corresponding to the red waveform in Fig. 17 plunges earlier than the orbit of the green waveform. Since the orbit corresponding to the green waveform has encountered a tidal resonance, we can deduce from Fig. 17 that it has experienced a positive jump in its constants of motion, allowing the radiation reaction to last longer as compared to the red waveform.

Fig. 17 only shows the dephasing of the gravitational waveform due to one tidal resonance. However, as we have noted from the resonance contour in Fig. 11, an orbit can cross several tidal resonances during its inspiral. These additional resonance crossings can result in an even more dephased waveform, but they can also potentially 'cancel out' previous phase shifts. So, to correctly predict an EMRI's waveform, strong theoretical input is needed.

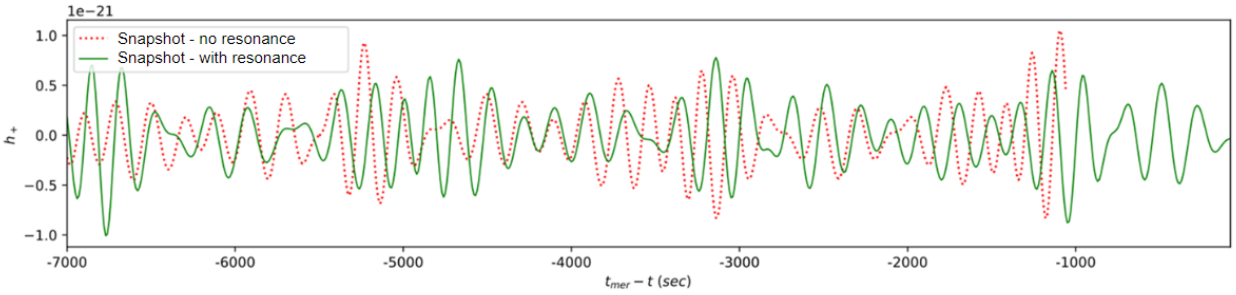

Figure 17: A comparison of h_+ waveforms. The green waveform is constructed by taking one tidal resonance into account, whereas this resonance crossing is neglected in the dashed red waveform. Figure adapted from [24].

3.3 Dynamic model

3.3.1 Equatorial plane

We will now discuss the jumps in L_z and Q obtained from a dynamic metric perturbation. At first, we will focus on the scenario where the tidal perturber is restricted to the equatorial plane. Similar to the stationary case, we only encounter resonances with $m \in \{-2, 0, -2\}$ here, because the electric quadrupole moment in Eq. (2.1.16a) is diagonal. When we assume an arbitrary inclination of the perturber with respect to the equatorial plane, we will find $m = \pm 1$ resonances. A similar analysis applies to the s-modes, as they also correspond to azimuthal motion. The fact that the electric quadrupole moment is diagonal explains that we only find resonances with $s \in \{-2, 0, 2\}$ for a perturber on the equatorial plane. Resonances with $s = \pm 1$ are again encountered if the perturber has an arbitrary configuration in the sky. However, these resonances are not formed from the electric quadrupole moment, but from the magnetic quadrupole moment in Eq. (2.1.16b), which is nonzero in the dynamic model. Generally, the only non-vanishing harmonic components of the magnetic quadrupole vector potential in Eq. (2.1.11) are given by $\mathcal{B}^{\mathrm{q}}_{1c}$ and $\mathcal{B}^{\mathrm{q}}_{1s}$, which correspond to the $s = \pm 1$ modes. These harmonic components are zero for a perturber on the equatorial plane. They are nonzero if the perturber has a general sky location, allowing the manifestation of $s = \pm 1$ resonances. Hence, we find that the electric quadrupole moments of even parity provide resonances with even s, while resonances with odd s are the consequence of the odd-parity magnetic quadrupole moments. This allows for a separate treatment of the electric and magnetic sector.

We focus on the electric sector first. Not every resonance with combinations of $m, s \in \{-2, 0, 2\}$ occurs in the equatorial plane. We can determine the resonance combinations of m and s by analyzing the functional form of the jump size as given in Eq. (2.4.14). In the equatorial plane we find

$$\left.\frac{dC}{d\lambda}\right|_{nkms}(a, e, x) = A_{nk00} + A_{nk-22}\, z^{-2} y^2 + A_{nk2-2}\, z^2 y^{-2}. \tag{3.3.1}$$

If we then perform the double integral over the azimuthal phases as given in Eq. 2.4.16), we find that we only encounter resonances with $m = -s$, which is in agreement with [45]. The functional form of the jump in Eq. (3.3.1) also confirms that resonances with $m, s = \pm 1$ are not encountered. The semi-analytical jump amplitudes can then be obtained by doing the integral in Eq. (2.4.17) numerically. We performed a consistency check on these amplitudes by also calculating them using the numerical four-dimensional integral as given in Eq. (2.4.11). The results were equivalent, while the four-dimensional integral was almost 400 times slower in some cases. We also calculated dynamical jump amplitudes in Q using the two-for-one deal as given by Eq. (2.4.20). Similarly to the stationary model, these amplitudes matched with the other integration methods within the margin of 0.1%. We find that no jump in the orbital energy E is induced despite that the perturber is allowed to move during the resonance. This can be explained from the fact that we found that the condition $\Omega_\phi \ll \omega_\phi$ still holds for the cases we studied. Therefore the stationary perturber approximation effectively still holds, leading to no jump in the orbital energy.

In order to compare the stationary and dynamic resonance models, we will look at the tidal resonance with $(n, k, m, s) = (3, 0, -2, 2)$. Fitting formulas for the jump's amplitude are given in Eqs. (C.3.1) and (C.3.2), where $\theta_y = 0$ again corresponds to the case of a tidal perturber on the equatorial plane. If we compare these with the corresponding stationary fitting formulas in Eqs. (C.1.1) and (C.1.2), we find that the dynamic amplitudes of this resonance are smaller by a factor of $2.5 - 12\%$ for orbits with eccentricities below $e = 0.7$. For more eccentric orbits, this difference can be over 30%. As a result, the maximal jump sizes in the dynamic model are smaller than the maximal jump sizes in the stationary model for this tidal resonance.

We can explain the difference in maximal jump sizes between both models by looking at the resonance contour in Fig. 21a. The $(3, 0, -2, 2)$-resonance corresponds to the thickly dashed black line. The solid black line, corresponding to the dynamic $(3, 0, -2, 0)$-resonance, is equivalent to the stationary $(3, 0, -2)$-resonance, because the dynamic resonance condition in Eq. (2.3.15) equals the stationary resonance condition in Eq. (2.3.8) if $s = 0$. The dynamic $(3, 0, -2, 0)$-resonance and the stationary $(3, 0, -2)$-resonance therefore occur at the same moment in the inspiral, which results in the same tidally induced amplitude in the orbital constants. The upper dashed black line in Fig. 21a corresponds to the $(3, 0, -2, -2)$-resonance. This resonance, as well as the $(3, 0, -2, 0)$-resonance, is not encountered when the perturber resides in the equatorial plane, since $m \neq s$. These resonances can be crossed by an orbit when the perturber is situated off the equatorial plane, as will be discussed in section 3.3.2.

Fig. 21a shows us that the $(3, 0, -2, 2)$-resonance always occurs at a lower value of p compared to the $(3, 0, -2)$-resonance. As a consequence, the dynamic jump amplitudes will be smaller than the stationary amplitudes for these resonances. This statement holds for all resonant orbits with $s > 0$, irrespective of the perturber's orbital inclination and the values of the set $\{n, k, m, a, e, x\}$. The opposite statement holds for dynamic resonances with $s < 0$. They occur earlier during the inspiral, leading to larger jump amplitudes. Figure 21a also shows that the difference in the value of p between stationary and dynamic resonances increases for higher values of e, which explains the larger difference in the jump's amplitude for more eccentric orbits. This effect becomes even bigger for resonances that occur at larger p-values.

Since the $(3, 0, -2, 2)$-resonance occurs at a smaller value of p compared to its stationary counterpart, it also occurs at a later moment in time. This can be easily seen in Figs. 1 and 10a, where both stationary and dynamic jumps of this resonance are displayed. This time delay can even be so large that the sequence of resonances encountered during the inspiral differs in the stationary and dynamic model. An example of such a scenario is shown in Fig. 10b. In the stationary model, the orbit crosses the $(3, 0, -2)$-resonance before encountering the $(3, -2, 0)$-resonance. In the dynamic model, on the other hand, the $(3, 0, -2, 2)$-resonance is crossed after the $(3, -2, 0, 0)$-resonance. The difference in the time of resonance between the stationary and dynamic jumps also results in different phases of the resonant orbit, which in turn can cause significant differences in the total jump size between the stationary and dynamic jumps. For example, an orbit can experience a jump in its constants of motion at a resonance crossing in the stationary model, while it can pass through the corresponding resonance in the dynamic model without noticing anything at all.

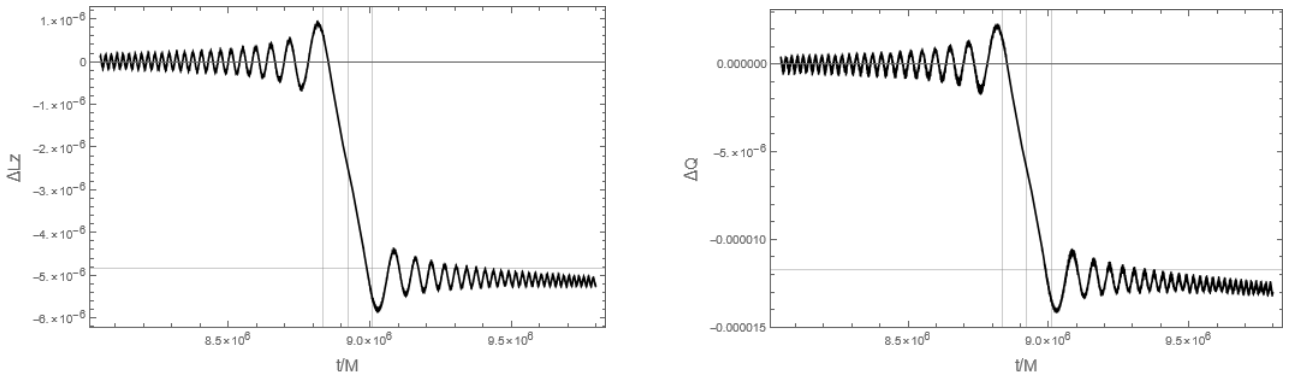

(a) $\Delta L_z = -4.83655 \times 10^{-6}$. (b) $\Delta Q = -1.17286 \times 10^{-5}$.

Figure 18: A closer look at the dynamic jumps in L_z and Q in Fig. 1.

We compare the numerical and analytical jump sizes in L_z and Q for the $(3, 0, -2, 2)$-resonance in Figs. 18 and 19. The phase at the resonance can now be obtained by numerically integrating Eq. (2.3.15) with respect to Boyer-Lindquist time t:

$$\chi_d = \int_0^{t_0} (n\omega_r(t) + k\omega_\theta(t) + m\omega_\phi(t) + s\Omega_\phi)\, dt. \tag{3.3.2}$$

We find that $\chi_d \mod 2\pi = 2.30$ for the jumps in Fig. 18 and $\chi_d \mod 2\pi = 5.99$ for the jumps in Fig. 19. The sine of the total phase again differs by a sign in both cases, resulting in negative jumps in Fig 18 and positive jumps in Fig 19. The total semi-analytical jump sizes are given below each figure and slightly underestimate the numerical jump sizes. The axis in Fig. 19b is shifted with the semi-analytical jump size of the $(3, -2, 0, 0)$-resonance, because this resonance is crossed first in the dynamic model. The jump in Q as a result of the $(3, -2, 0, 0)$-resonance is shown in Fig. 20.

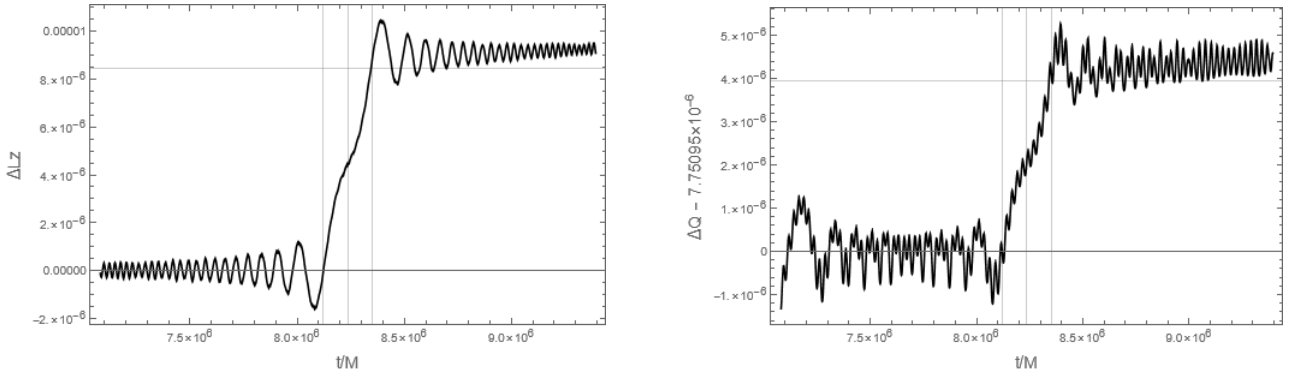

(a) $\Delta L_z = 8.43727 \times 10^{-6}$. (b) $\Delta Q = 3.93317 \times 10^{-6}$.

Figure 19: A closer look at the dynamic jumps in L_z and Q in Fig. 10, corresponding to the $(3, 0, -2)$-resonance. The vertical axis in the right plot is shifted, because the orbit crosses the $(3, -2, 0)$-resonance earlier in the inspiral.

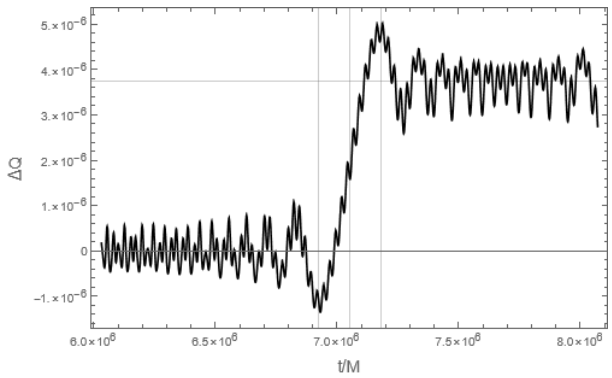

Figure 20: A closer look at the dynamic jump in Q in Fig. 10, corresponding to the $(3, -2, 0)$-resonance. The phase at the resonance is given by $\chi_s \mod 2\pi = 1.53$ and the jump size obtained from the semi-analytical analysis is given by $\Delta Q = 3.75095 \times 10^{-6}$.

3.3.2 General sky location of the perturber

We can again place the tidal perturber at an arbitrary location in the sky by rotating the tidal moments using the rotation matrices of Eq. (3.2.3). The rotated electric quadrupole moment is given by Eq. (3.2.2), and its magnetic counterpart can be constructed completely analogously as

$$\mathcal{B}_{ab}(t,\theta_y,\theta_z) = R_z(\theta_z)R_y(\theta_y)\mathcal{B}_{ab}(t)R_y(\theta_y)^T R_z(\theta_z)^T, \tag{3.3.3}$$

where $\mathcal{B}_{ab}(t)$ is given in Eq. (2.1.16b). As a result, the magnetic sector of the metric perturbation is also non-vanishing, and we can encounter tidal resonances with $m, s \in \{-2,-1,0,1,2\}$. The rates of Eq. (2.4.14) now also depend on θ_y and θ_z:

$$\left.\frac{dC}{d\lambda}\right|_{nkms}(a,e,x,\theta_y,\theta_z) = \sum_{-2\leq\mu,\sigma\leq 2} A_{nk\mu\sigma} z^\mu y^\sigma e^{-\mu\theta_z} f_{\mu\sigma}(\theta_y). \tag{3.3.4}$$

Analogous to Eq. (3.2.5), the jump amplitudes are then given as

$$\left\langle\frac{dC}{dt}\right\rangle\Big|_{nkms}(a,e,x,\theta_y,\theta_z) = \left\langle\frac{dC}{dt}\right\rangle\Big|_{nkms}^{\theta_{ms}}(a,e,x)\, e^{-m\theta_z} f_{ms}(\theta_y). \tag{3.3.5}$$

The dependence on θ_y is incorporated in the functions $f_{ms}(\theta_y)$, which depend on m and s in the dynamic model. The amplitudes $\left\langle\frac{dC}{dt}\right\rangle\big|_{nkms}^{\theta_{ms}}(a,e,x)$ are calculated for $\theta_z = 0$ and $\theta_y = \theta_{ms}$. The reference angle θ_{ms} also depends on both m and s and must be chosen such that $f_{ms}(\theta_{ms})$ is nonzero. Table 5 displays θ_{ms} and $f_{ms}(\theta_y)$ for all combinations of m and s. As these modes both correspond to azimuthal motion, we have $f_{ms}(\theta_y) = f_{sm}(\theta_y)$. Additionally we find that $f_{ms}(\theta_y) = f_{-m-s}(\theta_y)$. As a result, there are nine distinct functions of θ_y in the dynamic model. Similarly to the stationary case, it's possible to choose another reference angle $\tilde{\theta}_{ms}$ provided that $f_{ms}(\tilde{\theta}_{ms}) \neq 0$. The jump amplitude is then obtained as

$$\left\langle\frac{dC}{dt}\right\rangle\Big|_{nkms}(a,e,x,\theta_y,\theta_z) = \frac{1}{f_{ms}(\tilde{\theta}_{ms})}\left\langle\frac{dC}{dt}\right\rangle\Big|_{nkms}^{\tilde{\theta}_{ms}}(a,e,x)\, e^{-m\theta_z} f_{ms}(\theta_y). \tag{3.3.6}$$

The dependence on θ_z is equivalent to the stationary case and only depends on m. It can be included in the total phase of the jump, which is then given by $2\sin\left(\pm\frac{\pi}{4} - \chi_d + m\theta_z\right)$.

When the perturber is taken off the equatorial plane, the EMRI's secondary mass can cross all the resonances as displayed in the resonance contours in Figs. 21 and 22. These contours show all the places in the (e,p)-plane where the dynamic resonance condition of Eq. (2.3.15) is satisfied for given values of $a = 0.9M$ and $x = \cos 50°$. The set of numbers denotes the values of (n,k,m), whereas the value of s is specified by the type of line. These resonance contours show all low order dynamic resonances for which $k+m+s =$ even, since resonances with $k+m+s =$ odd vanish. This third selection rule is derived in Appendix D.3. The locations of the dynamic resonances with $s = 0$ in Fig. 21 coincide with the corresponding stationary resonances in Fig. 11. The dynamic contours in Fig 21 complement the stationary resonance contour by also including the dynamic $s = \pm 2$ resonances. So for each resonance crossed in the stationary model, an orbit potentially crosses three resonances in the dynamic model. Furthermore, an orbit also encounters the resonances displayed in Fig. 22 in the dynamic model. In the stationary model, these resonances vanished because they have $k+m =$ odd. These resonances are present in the dynamic model since we can take $s = \pm 1$, leading to $k+m+s =$ even.

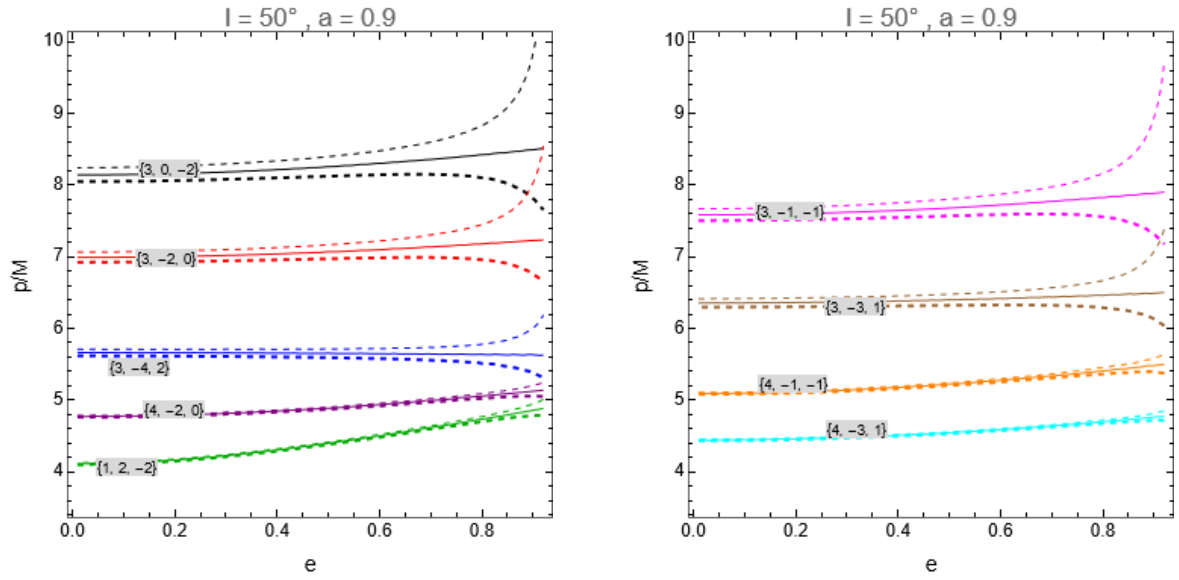

(a) Resonances with m even.

(b) Resonances with m odd.

Figure 21: Resonance contours of low order dynamic resonances for $a = 0.9M$, $x = \cos 50°$ and $k + m =$ even. The dynamic resonance condition of Eq. (2.3.15) is satisfied at each line. The set of numbers corresponds to the values of the set $\{n, k, m\}$, while the value of s is specified by the type of the line. The solid lines denote resonances with $s = 0$, the thickly dashed lines represent $s = 2$ resonances while $s = -2$ for the other dashed lines.

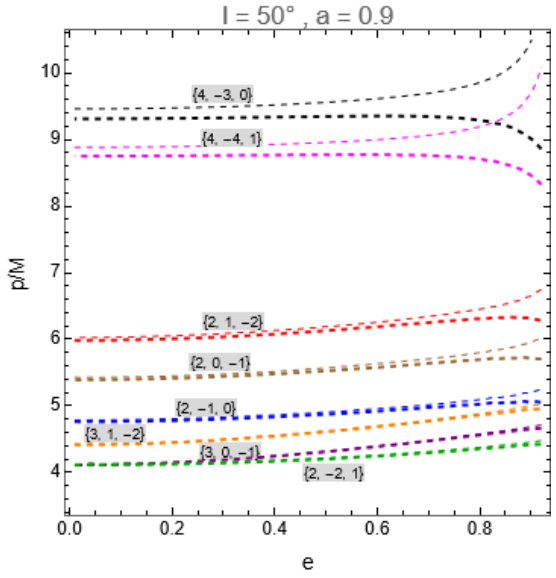

Figure 22: Resonance contour of low order dynamic resonances for $a = 0.9M$, $x = \cos 50°$ and $k + m =$ odd. The set of numbers corresponds to the values of the set $\{n, k, m\}$, while the value of s is specified by the type of the line. The thickly dashed lines represent $s = 1$ resonances while $s = -1$ for the other dashed lines.

To illustrate the many crossings of dynamic tidal resonances, we analyzed an orbit's inspiral where the perturber is inclined with an angle of $\theta_y = \frac{\pi}{4}$. The results are obtained using the osculating elements method and are displayed in Fig. 23. The jumps caused by the resonances are smaller compared to the jumps in Figs. 1 and 10, because they occur at lower values of p and e. Nevertheless, each jump in Fig. 23 has an impact on the gravitational waveform and can convey valuable

information on the environment close to the central BH. The biggest jumps are caused by the low order resonances and are displayed in Table 6, together with their time of resonance t_0 and sign of the jump. The other resonances that occur are of higher order, and therefore do not induce a large jump in L_z and Q.

As discussed below Eq. (2.3.15), the model of a dynamic perturber introduces additional resonances where $n, k, m \geq 0$ and $s < 0$. In practice, however, only a select group of these resonances manifests in the region of validity as displayed in Fig. 5. Other resonances occur in the regime where $p > b$, thereby violating the weak-field approximation. We find that highly eccentric orbits experience the extra resonances at a lower p-value. The $(1, 0, 0, -2)$-resonance is crossed closest to the central BH. An example of its resonant parameters are $\{a, p, e, x\} = \{0.5M, 29.9228M, 0.9, \cos 30°\}$ for a perturber inclination of $\theta_y = \frac{\pi}{4}$. From these conditions we can then calculate the jump size in L_z and Q in the usual semi-analytical way. This results in jump sizes in the order of 10^{-5}, which is similar in size to the resonances we have encountered in this thesis. Unfortunately this resonance cannot be analyzed using the osculating elements method, because the amplitude of the oscillations in L_z and Q, corresponding to the orbital motion at these large p-values, is of order 10^{-2}. Therefore the $(1, 0, 0, -2)$-resonance cannot be identified using the numerical plots of ΔL_z and ΔQ. The orbital oscillations will even get bigger for higher values of p. Hence, the extra resonances cannot be studied numerically. A jump based on these resonances can still be induced, because it follows from the semi-analytical analysis that the jump amplitudes do not vanish. Moreover, the impact of these extra resonances on the gravitational waveform will be bigger, since they occur at higher p-values. However, because these extra resonances manifest at larger distances from the central BH, the radiation reaction is so slow that the EMRI's smaller mass can be thousands of years away from the plunge. For example, we have calculated that an orbit crossing the $(1, 0, 0, -2)$-resonance is at least 1.3×10^3 years away from becoming a plunge orbit, which is much larger than the maximum of ~ 10 years that an EMRI lies in LISA's observational frequency band. Resonances occurring at larger p-values will plunge at an even later moment in time. Therefore these extra resonances are not relevant for LISA.

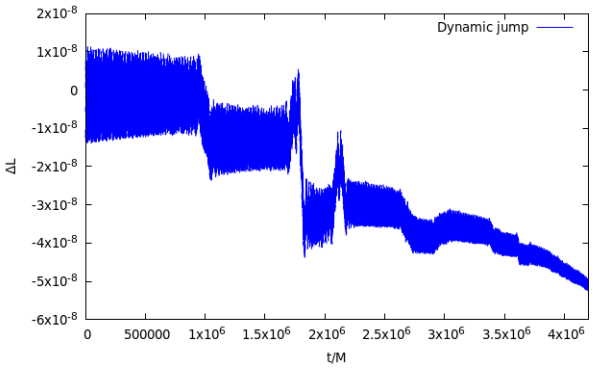

(a) The difference in L_z caused by a tidal perturber.

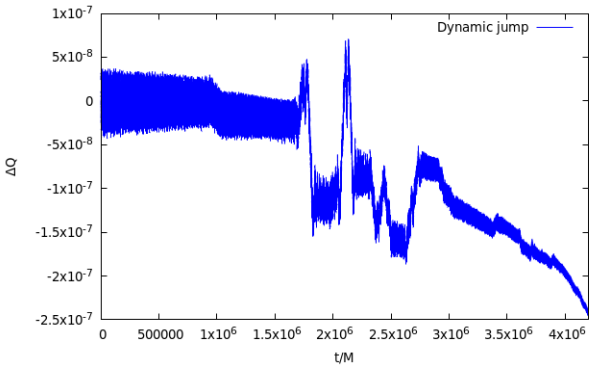

(b) The difference in Q caused by a tidal perturber.

Figure 23: The effect on an EMRI's orbital constants L_z and Q caused by a tidal perturber with mass $M_* = 30M_\odot$ at a distance $b = 10\,\text{AU}$ from the EMRI's central BH with mass $M = 4 \times 10^6 M_\odot$. The EMRI's mass ratio corresponds to $\eta = 7.5 \times 10^{-6}$ and the tidal perturber is inclined with $\frac{\pi}{4}$ rad with respect to the equatorial plane. The orbit's initial conditions are given by $\{a, p, e, x\} = \{0.5M, 8M, 0.4, \cos 70°\}$. Ten low order resonances take place. Their resonance times are given in Tab. 6.

The dephasing of the waveform can be studied using the same methods as discussed in section 3.2.5. The scaling relation of Eq. (3.2.8) is now given by

$$\Delta\Psi'_{nkms} = \Delta\Psi_{nkms}\left(\frac{M'}{M}\right)^{\frac{7}{2}}\left(\frac{\mu'}{\mu}\right)^{-\frac{3}{2}}\left(\frac{M'_*}{M_*}\right)\left(\frac{b'}{b}\right)^{-3}\left(\frac{f_{ms}(\theta'_y)}{f_{ms}(\theta_y)}\right). \tag{3.3.7}$$

However, this relation is now only approximately true, since M', M'_* and b' are also used to determine Ω'_ϕ. This frequency is used in the dynamic resonance condition to determine the resonant value of the semi-latus rectum (p'), which differs from the original resonant value p.

m	s	θ_{ms}	$f_{ms}(\theta_y)$
-2	-2	$\pi/2$	$(\cos\theta_y - 1)^2$
-2	-1	$\pi/2$	$(1-\cos\theta_y)\sin\theta_y$
-2	0	$\pi/2$	$\sin^2\theta_y$
-2	1	$\pi/2$	$(1+\cos\theta_y)\sin\theta_y$
-2	2	$\pi/2$	$(\cos\theta_y + 1)^2$
-1	-2	$\pi/2$	$(1-\cos\theta_y)\sin\theta_y$
-1	-1	$\pi/2$	$\cos\theta_y - \cos 2\theta_y$
-1	0	$\pi/4$	$\sin 2\theta_y$
-1	1	$\pi/2$	$-\cos\theta_y - \cos 2\theta_y$
-1	2	$\pi/2$	$(1+\cos\theta_y)\sin\theta_y$
0	-2	$\pi/2$	$\sin^2\theta_y$
0	-1	$\pi/4$	$\sin 2\theta_y$
0	0	$\pi/2$	$3\sin^2\theta_y - 2$
0	1	$\pi/4$	$\sin 2\theta_y$
0	2	$\pi/2$	$\sin^2\theta_y$
1	-2	$\pi/2$	$(1+\cos\theta_y)\sin\theta_y$
1	-1	$\pi/2$	$-\cos\theta_y - \cos 2\theta_y$
1	0	$\pi/4$	$\sin 2\theta_y$
1	1	$\pi/2$	$\cos\theta_y - \cos 2\theta_y$
1	2	$\pi/2$	$(1-\cos\theta_y)\sin\theta_y$
2	-2	$\pi/2$	$(\cos\theta_y + 1)^2$
2	-1	$\pi/2$	$(1+\cos\theta_y)\sin\theta_y$
2	0	$\pi/2$	$\sin^2\theta_y$
2	1	$\pi/2$	$(1-\cos\theta_y)\sin\theta_y$
2	2	$\pi/2$	$(\cos\theta_y - 1)^2$

Table 5: The functional dependence of the jumps on θ_y in the case of a dynamic perturber.

n	k	m	s	t_0/M	Sign of jump
2	1	-2	1	9.97×10^5	$-$
4	0	-2	0	1.72×10^6	$+$
2	0	-1	1	1.80×10^6	$-$
4	-1	-1	0	2.08×10^6	$+$
4	-1	-1	2	2.16×10^6	$-$
2	-1	0	-1	2.35×10^6	$-$
4	-2	0	0	2.41×10^6	$+$
2	-1	0	-1	2.48×10^6	$-$
4	-3	1	-2	2.66×10^6	$-\,(L_z),\ +\,(Q)$
4	-3	1	0	2.76×10^6	$-\,(L_z),\ +\,(Q)$

Table 6: Low order resonances of Fig. 23.

4 Summary and conclusion

In this thesis we constructed a semi-analytic framework to study tidal resonance effects in EMRIs for both a stationary and a dynamic tidal field. We focused on a tidal field consisting of a single stellar mass object with a similar mass as the EMRI's secondary. In the dynamic model, the perturber was allowed to move in a circular orbit around the central massive BH at the time of resonance. Our research mainly revolved around the calculation of the tidally induced jump amplitudes in the EMRI's orbital constants of motion in both the stationary and the dynamic model. In doing so, we focused on keeping the computational costs as low as possible. This was firstly achieved in the computation of the metric perturbation due to the tidal perturber. We used Schwarzschild perturbation theory to calculate this perturbation in the metric, thereby neglecting spin effects of the EMRI's central BH. We found that this approach was approximately 15 times faster than using Kerr perturbation theory, as was done in previous research [22, 24]. Yet, the results remained accurate within 1.0%. We could fully characterize the metric perturbation on the basis of so-called tidal quadrupole moments, whose functional form was determined using a metric matching procedure. We then formulated a metric ansatz of the total spacetime as a function of these tidal moments, spherical harmonics and radial functions. The functional form of the radial functions could be determined by solving the linearized Einstein Equations in vacuum, and the metric perturbation was found by subtracting the Schwarzschild metric from the metric of the total spacetime.

When we modelled for the motion of the EMRI's secondary mass, we allowed the massive central BH to rotate again. To lowest order, the orbital motion could be described by the geodesic equations in Kerr spacetime. We described the EMRI's smaller mass' four-velocity in a Mino time formalism, and were able to reformulate the geodesic orbital motion in terms of fundamental orbital frequencies, which played a key role in describing tidal resonances. The tidal force was accounted for in the orbital motion by using an action-angle formalism. We made an adiabatic approximation, after which we rewrote the tidal force in its Fourier components. This led to the resonance condition and the resonant tidal force terms in both the stationary and dynamic model.

We used the metric perturbation and the EMRI's four-velocity to find the tidally induced acceleration, which in turn led us to the general evolution in the constants L_z and Q induced by a tidal perturbation. We calculated the change in these constants, as caused by a tidal resonance, by performing an averaging integral. We managed to do this integral semi-analytically, in contrast to the full numerical integral used in previous research [22, 24]. This enhanced computational times by at least 20 times in the stationary model and almost 400 times in the dynamic model. Ultimately, we constructed fitting formulae of these jump amplitudes across the whole parameter space, allowing for efficient future jump calculations.

In the stationary model, we first studied low order tidal resonances for a tidal perturber situated on the equatorial plane. We found that only resonances with $m \in \{-2, 0, 2\}$ contributed to shifts in the orbital constants of motion, which could be explained from the functional form of the electric quadrupole moment. Additionally, we found that resonances with $m = 0$ do not induce a jump in L_z, as the axisymmetry of the EMRI spacetime is preserved in this case. We further characterized stationary resonances on the basis of resonance contours and the first selection rule, i.e., only resonances with $k =$ even contribute to the shifts in the orbital constants of motion. Moreover, we used the numerical method of forced osculating elements as a consistency check on our semi-analytical calculations, and found a great match between the numerical and semi-analytical jump sizes. Next, we moved the tidal perturber off the equatorial plane, and exploited the functional dependence on the perturber's sky location analytically. This also allowed the manifestation of resonances with $m = \pm 1$, which required a new selection rule, stating that tidal resonances with

$k + m =$ odd are suppressed. Lastly, we discussed the impact of tidal resonances on the GWs radiated by an EMRI. In the end, we calculated jump sizes that matched to great extent with the jump sizes from previous research, while we computed them using less computationally expensive methods.

In the dynamic model, we first analyzed tidal resonance effects for a perturber moving in a circular orbit in the equatorial plane. We found that only tidal resonances with $m = -s$ alter the orbit of the EMRI's smaller mass in this case. Moreover, we compared stationary and dynamic jump amplitudes, discovering that they only differ by a few percent for general orbits with eccentricities below $e = 0.7$. This difference could be as big as 30% for highly eccentric orbits. We were able to study this effect of the orbital eccentricity on the jump amplitudes by comparing stationary and dynamic resonance contours. They deviated most in the highly eccentric regime. Consequently, dynamic resonances for highly eccentric orbits could be encountered much earlier/later in the inspiral, leading to significantly larger/smaller jump amplitudes compared to the stationary model. In general, we found that the difference in the time of resonance between dynamic and stationary models does have a noticeable impact on the total jump size. Firstly, this led to different orbital phases at the time of resonance in both models. In an extreme case, an orbit's constants of motion experience a jump by crossing a tidal resonance in the stationary model, while the same orbit did not feel a resonance effect in the dynamic model (and vice versa). Secondly, the order in which tidal resonances appear during the inspiral could even differ in both models. The order of resonance crossings is extremely important in the construction of EMRI waveform templates. Therefore, if we do not model for the perturber's dynamics, incorrect EMRI waveform templates may be constructed. This can ultimately lead to the estimation of wrong parameters of the EMRI spacetime, or even the conclusion that GR is an incorrect theory of gravity.

Next, we placed the tidal perturber at an arbitrary sky location in the dynamic model, thereby allowing it to move on an inclined circular orbit. We discovered that the functional dependence of this inclination angle on the total jump size is completely determined by the values of m and s. We found this functional dependence explicitly by using a full analytical analysis. Furthermore, we also found tidal resonances with $m, s = \pm 1$ when the perturber was not situated on the equatorial plane. Consequently, we formulated the most general selection rule, stating that only resonances with $k + m + s =$ even lead to jumps in the orbital constants of motion. Lastly, we discussed the dynamic resonance contours in greater detail. We found that, for given values of the set (n, k, m) with $n > 0$, resonances with a positive value of s are encountered earlier in the inspiral than resonances with negative s. If $n = 0$, the same statement holds if $k > 0$. Moreover, we discovered that an orbit crosses several more tidal resonances in the dynamic model compared to the stationary model. As each resonance crossing can lead to a phase shift in the radiated GWs, a gravitational waveform constructed from the dynamic model would potentially be even more dephased than a waveform obtained from the stationary model. To conclude, the inclusion of the perturber's dynamics in EMRI modeling may significantly impact the analysis on LISA's data in the future, while the maximal jump sizes are generally not altered much compared to the model of a stationary perturber.

5 Discussion and outlook

The framework provided in this thesis can be used to efficiently analyze tidal resonance effects in EMRIs for both stationary and dynamic tidal perturbations. In our studies, we only considered the tidal perturbation to be due to a single pointlike stellar mass object. In practice, an EMRI can be accompanied by several of such objects, each having the potential to cause tidal resonance effects. Even an accretion disk around an EMRI's central massive BH can impact the waveform of the emitted GWs. If we could calculate the perturbation in the metric arising from an accretion disk, we could study its impact on the EMRI's orbital motion by applying the same methods as presented in this work. We can learn useful information about the accretion disk by identifying the induced tidal resonances correctly. Additionally, an accretion disk can also secularly impact the orbit of the EMRI's secondary mass. Future studies may point out the magnitude of this secular effect, and compare it with the impact through resonances.

Our work has been based on the the weak field approximation, which allowed for a Keplerian treatment of the tidal perturber. In our numerical analysis, we have assumed that EMRI's central BH is significantly larger than the perturber. Thereby we have shown the minimal impact of tidal resonances, as the jump size in the orbital constants of motion scales linearly with the perturber's mass. In practice, the tidal perturber could have a mass in the same order of magnitude as the central BH's mass. If the distance between both bodies remains sufficiently large, the weak field approximation stays valid, so that the framework provided in this thesis can also be applied to study tidal resonance effects for such scenarios. Furthermore, we have assumed that the perturber is on a circular orbit around the central massive BH, which can be generalized to an elliptic orbit in future research. This scenario is automatically accounted for in the stationary model, as only the distance between central BH and perturber could be different. In the dynamic model, on the other hand, the tidally induced jump sizes will be impacted.

We only constructed the metric perturbation from the quadrupole moments of the lowest post-Newtonian order. This may be insufficient when we place the perturber closer to the central BH, as this causes the perturber's orbital velocity to increase. Consequently, we will have to take higher order terms into account through the whole derivation of the metric perturbation. Firstly, we will have to add terms of first post-Newtonian order to the quadrupole moments and the perturber's orbital frequency. Secondly, we have to take the octupole moments into account as well, which will introduce new tidal resonances with $m, s = \pm 3$. As the perturber is situated closer to the EMRI system, these resonances cannot be neglected anymore. Lastly, we will need to consider the time derivatives of all tidal moments too.

If the perturber is relatively close to the central massive BH, we also cannot neglect the latter's spin in the calculation of the metric perturbation. Moreover, we can allow the tidal perturber to be rotating as well, which can have a small effect on the tidally induced jumps. The spin effects of both bodies can be incorporated as perturbative terms in the metric of the total spacetime [36]. The perturbation in the metric can then still be calculated in the framework of Schwarzschild perturbation theory. At some particular distance between perturber and central BH, however, it is expected that the central BH's spin effects play such a big role that one has to consult to Kerr perturbation theory again to compute the metric perturbation. Moreover, we cannot place the perturber too close to the central BH, as this violates the weak field approximation. This breaks the perturbative treatment of our analysis, and we have to regard the total system as a three-body problem. As a consequence, we can only study resonance effects in this case using full numerical relativity, which at this stage even cannot handle isolated EMRIs, let alone three-body systems with such mass differences.

The stationary and dynamic models for computing tidally induced jump sizes in an EMRI's orbital constants of motion serve as input for the creation of fast EMRI waveform templates. We have motivated the importance of including the tidal perturber's dynamics in the modelling of an EMRI's orbital evolution. A next step in this research field would be to construct these waveforms based on a dynamic tidal perturbation. These waveforms can subsequently be compared to the waveforms constructed from the stationary resonance model as described in [24]. Ultimately, these more realistic EMRI waveforms based on a dynamic tidal perturbation can be used to extract information from the data gathered by LISA in the future. By modelling for the tidal perturbation's dynamics, we retain the ability to perform high precision tests of GR, and we will be able to infer valuable information about the EMRI, as well as its tidal environment.

References

[1] Black Hole Perturbation Toolkit. (bhptoolkit.org).

[2] B. Abbott, R. Abbott, T. Abbott, et al. Observation of gravitational waves from a binary black hole merger. *Physical Review Letters*, 116(6), feb 2016.

[3] R. Abbott, T. D. Abbott, S. Abraham, et al. Population properties of compact objects from the second LIGO–virgo gravitational-wave transient catalog. *The Astrophysical Journal Letters*, 913(1):L7, may 2021.

[4] P. Amaro-Seoane, H. Audley, S. Babak, et al. Laser interferometer space antenna, 2017.

[5] A. Askar, C. Belczynski, G. Bertone, et al. Black holes, gravitational waves and fundamental physics: a roadmap. *Classical and Quantum Gravity*, 36(14):143001, jun 2019.

[6] S. Babak, J. Gair, A. Sesana, E. Barausse, C. F. Sopuerta, C. P. L. Berry, E. Berti, P. Amaro-Seoane, A. Petiteau, and A. Klein. Science with the space-based interferometer lisa. v. extreme mass-ratio inspirals. *Phys. Rev. D*, 95:103012, May 2017.

[7] L. Barack and A. Pound. Self-force and radiation reaction in general relativity. *Reports on Progress in Physics*, 82(1):016904, nov 2018.

[8] C. P. L. Berry, S. A. Hughes, C. F. Sopuerta, A. J. K. Chua, A. Heffernan, K. Holley-Bockelmann, D. P. Mihaylov, M. C. Miller, and A. Sesana. The unique potential of extreme mass-ratio inspirals for gravitational-wave astronomy, 2019.

[9] B. Bonga, H. Yang, and S. A. Hughes. Tidal resonance in extreme mass-ratio inspirals. *Physical Review Letters*, 123(10), sep 2019.

[10] D. Bronicki, A. Cárdenas-Avendaño, and L. C. Stein. Tidally-induced nonlinear resonances in emris with an analogue model, 2023.

[11] F. Camilloni, G. Grignani, T. Harmark, R. Oliveri, M. Orselli, and D. Pica. Tidal deformations of a binary system induced by an external kerr black hole. *Physical Review D*, 107(8), apr 2023.

[12] B. D. Carter. Global structure of the kerr family of gravitational fields. *Physical Review*, 174:1559–1571, 1968.

[13] A. J. Chua, M. L. Katz, N. Warburton, and S. A. Hughes. Rapid generation of fully relativistic extreme-mass-ratio-inspiral waveform templates for LISA data analysis. *Physical Review Letters*, 126(5), feb 2021.

[14] S. Drasco, É . É. Flanagan, and S. A. Hughes. Computing inspirals in kerr in the adiabatic regime: I. the scalar case. *Classical and Quantum Gravity*, 22(15):S801–S846, jul 2005.

[15] S. Drasco and S. A. Hughes. Rotating black hole orbit functionals in the frequency domain. *Physical Review D*, 69(4), feb 2004.

[16] S. Drasco and S. A. Hughes. Gravitational wave snapshots of generic extreme mass ratio inspirals. *Physical Review D*, 73(2), jan 2006.

[17] É . É. Flanagan and T. Hinderer. Transient resonances in the inspirals of point particles into black holes. *Physical Review Letters*, 109(7), aug 2012.

[18] R. Fujita and W. Hikida. Analytical solutions of bound timelike geodesic orbits in kerr spacetime. *Classical and Quantum Gravity*, 26(13):135002, jun 2009.

[19] R. Fujita and M. Shibata. Extreme mass ratio inspirals on the equatorial plane in the adiabatic order. *Phys. Rev. D*, 102:064005, Sep 2020.

[20] J. R. Gair, É . É. Flanagan, S. Drasco, T. Hinderer, and S. Babak. Forced motion near black holes. *Physical Review D*, 83(4), feb 2011.

[21] R. H. Gowdy. Affine projection tensor geometry: Decomposing the curvature tensor when the connection is arbitrary and the projection is tilted. *Journal of Mathematical Physics*, 35(3):1274–1301, mar 1994.

[22] P. Gupta, B. Bonga, A. J. Chua, and T. Tanaka. Importance of tidal resonances in extreme-mass-ratio inspirals. *Physical Review D*, 104(4), aug 2021.

[23] P. Gupta, T. Kakehi, and T. Tanaka. Resonant jumps induced by stationary tidal perturbation: a two-for-one deal. *Classical and Quantum Gravity*, 39(24):245005, nov 2022.

[24] P. Gupta, L. Speri, B. Bonga, A. J. Chua, and T. Tanaka. Modeling transient resonances in extreme-mass-ratio inspirals. *Physical Review D*, 106(10), nov 2022.

[25] T. Hinderer and É . É. Flanagan. Two-timescale analysis of extreme mass ratio inspirals in kerr spacetime: Orbital motion. *Physical Review D*, 78(6), sep 2008.

[26] C. Hopman. Astrophysics of extreme mass ratio inspiral sources. In *AIP Conference Proceedings*. AIP, 2006.

[27] S. A. Hughes, S. Drasco, É . É. Flanagan, and J. Franklin. Gravitational radiation reaction and inspiral waveforms in the adiabatic limit. *Physical Review Letters*, 94(22), jun 2005.

[28] M. L. Katz, A. J. Chua, L. Speri, N. Warburton, and S. A. Hughes. Fast extreme-mass-ratio-inspiral waveforms: New tools for millihertz gravitational-wave data analysis. *Physical Review D*, 104(6), sep 2021.

[29] M. Kerachian, L. Polcar, V. Skoupý, C. Efthymiopoulos, and G. Lukes-Gerakopoulos. Action-angle formalism for extreme mass ratio inspirals in kerr spacetime, 2023.

[30] J. Kevorkian and J. D. Cole. Multiple scale and singular perturbation methods. 1996.

[31] P. Lynch, M. van de Meent, and N. Warburton. Eccentric self-forced inspirals into a rotating black hole. *Classical and Quantum Gravity*, 39(14):145004, jun 2022.

[32] K. Martel and E. Poisson. Gravitational perturbations of the schwarzschild spacetime: A practical covariant and gauge-invariant formalism. *Physical Review D*, 71(10), may 2005.

[33] Y. Mino. Perturbative approach to an orbital evolution around a supermassive black hole. *Physical Review D*, 67(8), apr 2003.

[34] Z. Nasipak. Adiabatic evolution due to the conservative scalar self-force during orbital resonances. *Physical Review D*, 106(6), sep 2022.

[35] E. Poisson. Metric of a tidally distorted nonrotating black hole. *Physical Review Letters*, 94(16), apr 2005.

[36] E. Poisson. Tidal deformation of a slowly rotating black hole. *Physical Review D*, 91(4), feb 2015.

[37] E. Poisson and E. Corrigan. Nonrotating black hole in a post-newtonian tidal environment. II. *Physical Review D*, 97(12), jun 2018.

[38] E. Poisson, A. Pound, and I. Vega. The motion of point particles in curved spacetime. *Living Reviews in Relativity*, 14(1), sep 2011.

[39] E. Poisson and I. Vlasov. Geometry and dynamics of a tidally deformed black hole. *Physical Review D*, 81(2), jan 2010.

[40] A. Pound and E. Poisson. Osculating orbits in schwarzschild spacetime, with an application to extreme mass-ratio inspirals. *Physical Review D*, 77(4), feb 2008.

[41] A. Pound and B. Wardell. Black hole perturbation theory and gravitational self-force. In *Handbook of Gravitational Wave Astronomy*, pages 1–119. Springer Singapore, 2021.

[42] N. Sago, L. Barack, and S. Detweiler. Two approaches for the gravitational self-force in black hole spacetime: Comparison of numerical results. *Physical Review D*, 78(12), dec 2008.

[43] N. Sago and R. Fujita. Calculation of radiation reaction effect on orbital parameters in Kerr spacetime. *Progress of Theoretical and Experimental Physics*, 2015(7), 07 2015. 073E03.

[44] W. Schmidt. Celestial mechanics in kerr spacetime. *Classical and Quantum Gravity*, 19(10):2743–2764, apr 2002.

[45] M. Silva and C. Hirata. Dynamical perturbations around an extreme mass ratio inspiral near resonance. *Physical Review D*, 106(8), oct 2022.

[46] A. D. A. M. Spallicci, P. Ritter, and S. Aoudia. Self-force driven motion in curved spacetimes, 2014.

[47] L. Speri and J. R. Gair. Assessing the impact of transient orbital resonances. *Physical Review D*, 103(12), jun 2021.

[48] S. Taylor and E. Poisson. Nonrotating black hole in a post-newtonian tidal environment. *Physical Review D*, 78(8), oct 2008.

[49] S. A. Teukolsky. Perturbations of a rotating black hole. 1. Fundamental equations for gravitational electromagnetic and neutrino field perturbations. *Astrophys. J.*, 185:635–647, 1973.

[50] S. A. Teukolsky. The kerr metric. *Classical and Quantum Gravity*, 32(12):124006, jun 2015.

[51] R. M. Wald. *General Relativity*. Chicago Univ. Pr., Chicago, USA, 1984.

[52] C. M. Will. *Gravity: Newtonian, Post-Newtonian, and General Relativistic*. 2016.

[53] H. Yang and M. Casals. General relativistic dynamics of an extreme mass-ratio binary interacting with an external body. *Physical Review D*, 96(8), oct 2017.

[54] N. Yunes and J. A. González. Metric of a tidally perturbed spinning black hole. *Physical Review D*, 73(2), jan 2006.

[55] C. Zhang, W.-B. Han, and S.-C. Yang. Analytical effective one-body formalism for extreme-mass-ratio inspirals with eccentric orbits. *Communications in Theoretical Physics*, 73(8):085401, jun 2021.

[56] X.-H. Zhang. Multipole expansions of the general-relativistic gravitational field of the external universe. *Phys. Rev. D*, 34:991–1004, Aug 1986.

A Radial functions

In this appendix we will solve the linearized Einstein equations in vacuum to retrieve the functional form of the radial functions e^{q}_{tt}, e^{q}_{rr} and e^{q} appearing in the tidally deformed Schwarzschild metric in Eq. (2.1.13). So we restrict ourselves to metric perturbations due to quadrupolar electric tidal perturbations. Therefore we will only focus on the even-parity sector of the metric perturbation, which is decoupled from the odd-parity sector. The derivation of these radial functions is most easily done in Eddington-Finkelstein (EF) coordinates. Therefore we perform a coordinate transformation from the usual (t, r, θ, ϕ)-coordinates to EF coordinates using

$$v = t + r + 2M \ln\Big(\frac{r}{2M} - 1\Big). \tag{A.0.1}$$

The even-parity sector of the tidally deformed Schwarzschild metric in EF coordinates looks like

$$\tilde{g}_{vv} = -f + r^2 e^{\mathrm{q}}_{vv} \mathcal{E}^{\mathrm{q}}, \tag{A.0.2a}$$
$$\tilde{g}_{vr} = 1 + r^2 e^{\mathrm{q}}_{vr} \mathcal{E}^{\mathrm{q}}, \tag{A.0.2b}$$
$$\tilde{g}_{rr} = r^2 \tilde{e}^{\mathrm{q}}_{rr} \mathcal{E}^{\mathrm{q}}, \tag{A.0.2c}$$
$$\tilde{g}_{tA} = 0, \tag{A.0.2d}$$
$$\tilde{g}_{rA} = 0, \tag{A.0.2e}$$
$$\tilde{g}_{AB} = r^2 \Omega_{AB} \left(1 + r^2 e^{\mathrm{q}} \mathcal{E}^{\mathrm{q}}\right). \tag{A.0.2f}$$

The radial functions are now given by e^{q}_{vv}, e^{q}_{vr}, $\tilde{e}^{\mathrm{q}}_{rr}$ and e^{q}. Here, $\tilde{e}^{\mathrm{q}}_{rr}$ is not equivalent to e^{q}_{rr} in Tab. 3. The function e^{q} is equivalent in both Eqs. (2.1.13) and (A.0.2), because the angular coordinates are not altered by the coordinate transformation of Eq. (A.0.1). We will now solve the linearized Einstein equations for the new radial functions. The functional form of the original radial functions e^{q}_{tt}, e^{q}_{rr} and e^{q} is then found by transforming the total metric back to (t, r, θ, ϕ)-coordinates.

The linearized Einstein equations in vacuum are given by

$$G_{\mu\nu} := R_{\mu\nu} - \frac{1}{2}\tilde{g}_{\mu\nu} R = 0. \tag{A.0.3}$$

Here, $R_{\mu\nu}$ is the Ricci tensor, which can be determined from the perturbed metric $\tilde{g}_{\mu\nu}$ as given in Eq. (A.0.2). The Ricci scalar is given by $R = \tilde{g}^{\mu\nu} R_{\mu\nu}$, where $\tilde{g}^{\mu\nu}$ is the inverse perturbed metric. Hence, the Einstein tensor $G_{\mu\nu}$ can purely be determined from the functional form of $\tilde{g}_{\mu\nu}$. We now substitute this metric in Eq. (A.0.3), where we substitute $\mathcal{E}^{\mathrm{q}}$ as given in Eq. (2.1.9). The harmonic components $\mathcal{E}^{\mathrm{q}}_m$ are only given in their general form as displayed in Tab. 1, meaning that the nature of the tidal perturber is not specified yet. By solving the equation $G_{\theta\phi} = 0$, we find that

$$\tilde{e}^{\mathrm{q}}_{rr} = -2 f^{-1} e^{\mathrm{q}}_{vr}. \tag{A.0.4}$$

We now eliminate $\tilde{e}^{\mathrm{q}}_{rr}$ by substituting this expression in the other Einstein equations. If we then solve for $G_{vv} + f\, G_{vr} = 0$, we find

$$e^{\mathrm{q}}_{vr} = -f^{-1} e^{\mathrm{q}}_{vv}. \tag{A.0.5}$$

This equation is again substituted in $G_{\mu\nu}$ to eliminate e^{q}_{vr}. The Einstein equations are now only a function of e^{q}_{vv}, e^{q}, their derivatives with respect to r and the angular coordinates θ^A. The angular part is completely decoupled from the radial part, as can easily be seen from the metric in Eq. (A.0.2). To this end, we define the tensor $\mathfrak{R}_{\mu\nu}$ as the radial part of the Einstein tensor $G_{\mu\nu}$. We can then solve the linearized Einstein equations in vacuum by solving

$$\mathfrak{R}_{\mu\nu} = 0. \tag{A.0.6}$$

Three nonzero components of the radial tensor are given by

$$\mathfrak{R}_{rr} = -6e^{\mathrm{q}} + r\left(-r\ddot{e}^{\mathrm{q}} - 6\dot{e}^{\mathrm{q}} + \frac{6r}{(-2M+r)^2}e^{\mathrm{q}}_{vv}\right), \tag{A.0.7a}$$

$$\mathfrak{R}_{r\theta} = -f^{-1}\left((-4M+2r)e^{\mathrm{q}} + r\left(-2e^{\mathrm{q}}_{vv} + (-2M+r)\dot{e}^{\mathrm{q}} - r\dot{e}^{\mathrm{q}}_{vv}\right)\right), \tag{A.0.7b}$$

$$\mathfrak{R}_{\theta\theta} = -\frac{1}{16}r\left((-8M+6r)e^{\mathrm{q}} + r\left(-6e^{\mathrm{q}}_{vv} + (-10M+6r)\dot{e}^{\mathrm{q}} + r\left(-6\dot{e}^{\mathrm{q}}_{vv} + (-2M+r)\ddot{e}^{\mathrm{q}} - r\ddot{e}^{\mathrm{q}}_{vv}\right)\right)\right). \tag{A.0.7c}$$

Here, a dot denotes a derivative with respect to the radial coordinate r, and all three components should vanish according to Eq. (A.0.6). We can eliminate all dependence on e^{q} and its derivatives by adding the three components in a clever way:

$$0 = \frac{(-2M+r)^2}{r}\mathfrak{R}_{rr} - \frac{2M(2M-r)}{r^2}\mathfrak{R}_{r\theta} + \frac{16(2M-r)}{r^2}\mathfrak{R}_{\theta\theta} \tag{A.0.8a}$$

$$= r^2(2M-r)\ddot{e}^{\mathrm{q}}_{vv} + r(14M-6r)\dot{e}^{\mathrm{q}}_{vv} + 16Me^{\mathrm{q}}_{vv}. \tag{A.0.8b}$$

The resulting equation is a second order differential equation for e^{q}_{vv}. The corresponding solution can then be fully determined up to two integration constants. We can fix one of these constants by demanding that the solution is regular at the Schwarzschild event horizon of $r = 2M$. The other integration constant is then resolved by demanding that e^{q}_{vv} evaluates to 1 in the limit of $r \to \infty$ [39]. As a result, we find the solution

$$e^{\mathrm{q}}_{vv} = -f^2. \tag{A.0.9}$$

We now substitute this value and its derivative in Eq. (A.0.7b), which should vanish, resulting in a first order differential equation for e^{q}. The solution of this equation is then determined up to one constant of integration. This constant can be found by substituting the solution of e^{q}, as well as the solution of e^{q}_{vv} as given in Eq. (A.0.9), in the equation $\mathfrak{R}_{vv} = 0$. We then solve for the integration constant, which in turn leads to the solution

$$e^{\mathrm{q}} = -1 + \frac{2M^2}{r^2}. \tag{A.0.10}$$

Finally, we substitute Eq. (A.0.9) in Eq. (A.0.4) to find

$$e^{\mathrm{q}}_{vr} = f, \tag{A.0.11}$$

which we subsequently substitute in Eq. (A.0.5) to find the last radial function

$$\tilde{e}^{\mathrm{q}}_{rr} = -2. \tag{A.0.12}$$

The resulting four radial functions can then be substituted back in Eq. (A.0.2) to find the tidally deformed Schwarzschild metric in EF coordinates. Lastly, we use the transformation of Eq. (A.0.1) to find the perturbed Schwarzschild metric in (t, r, θ, ϕ)-coordinates again. We retrieve the metric as displayed in Eq. (2.1.13), where the corresponding radial functions e^{q}_{tt}, e^{q}_{rr} and e^{q} now have the functional form as shown in Tab. 3. The functional form of the radial function b^{q}_t can be found by performing a similar analysis on the odd-parity sector of the metric perturbation.

B Induced acceleration

In this appendix we will derive Eq. (2.4.3), which states the acceleration a^α of a test particle in a Kerr background $g_{\mu\nu}$, induced by a given metric perturbation $h_{\mu\nu}$. The full metric $\tilde{g}_{\mu\nu}$ is given by Eq. (2.1.1). We will first introduce the normal projection operator, as this operator serves as a powerful tool in the derivation. Secondly, we will derive the connection between the covariant derivatives in the Kerr spacetime $\left(\nabla_\alpha\right)$ and the full spacetime $\left(\tilde{\nabla}_\alpha\right)$. Ultimately we will derive an equation for a^α up to first order in h. Therefore, we will neglect terms of $\mathcal{O}(h^2)$ or higher in the whole derivation.

B.1 Normal projection operator

First we will introduce the so-called normal projection operator P. This operator provides the projection of an arbitrary vector onto the vector's tangent space. Projection operators are idempotent, which means they have to satisfy $P^2 = P$. The normal projection operator is defined as $P_\alpha{}^\beta = \delta_\alpha{}^\beta + u_\alpha u^\beta$. Here, $u^\alpha = \frac{dx^\alpha}{d\tau}$ is the four-velocity of the test particle in the Kerr background, and τ is its proper time. [21]

The normal projection onto the four-velocity itself should vanish, because u^α is defined to be the unit vector tangent to the worldline of the test particle. This is can be easily verified:

$$\begin{aligned} P_\alpha{}^\beta u^\alpha &= (\delta_\alpha{}^\beta + u_\alpha u^\beta)u^\alpha \\ &= u^\beta + u_\alpha u^\alpha u^\beta \\ &= u^\beta - u^\beta \\ &= 0. \end{aligned} \tag{B.1.1}$$

In the third line of this calculation, the normalization of the four velocity is used:

$$u_\alpha u^\alpha = -1. \tag{B.1.2}$$

The idempotence of $P_\alpha{}^\beta$ can be easily shown as well:

$$\begin{aligned} P_\alpha{}^\beta P_\beta{}^\gamma &= (\delta_\alpha{}^\beta + u_\alpha u^\beta)(\delta_\beta{}^\gamma + u_\beta u^\gamma) \\ &= \delta_\alpha{}^\gamma + u_\alpha u^\gamma + u_\alpha u^\gamma + u_\alpha u^\beta u_\beta u^\gamma \\ &\overset{B.1.2}{=} \delta_\alpha{}^\gamma + u_\alpha u^\gamma \\ &= P_\alpha{}^\gamma. \end{aligned} \tag{B.1.3}$$

In the derivation of the induced acceleration we will need its projection. In the Kerr background spacetime, the acceleration is defined as $a^\alpha = \frac{du^\alpha}{d\tau} = u^\gamma \nabla_\gamma u^\alpha$. We notice that the particle's four-velocity and four-acceleration are orthogonal:

$$u_\alpha a^\alpha = u_\alpha u^\gamma \nabla_\gamma u^\alpha = \frac{1}{2} u^\gamma \nabla_\gamma \left(u^\alpha u_\alpha\right) \overset{B.1.2}{=} \frac{1}{2} u^\gamma \nabla_\gamma \left(-1\right) = 0. \tag{B.1.4}$$

The normal projection of a^α is then given by

$$P_\alpha{}^\beta a^\alpha = (\delta_\alpha{}^\beta + u_\alpha u^\beta)a^\alpha = a^\beta + u_\alpha a^\alpha u^\beta \overset{B.1.4}{=} a^\beta. \tag{B.1.5}$$

B.2 Covariant derivative connection

Because $\tilde{\nabla}_\alpha$ and ∇_α are both derivative operators, there exists a connection between both operators when acted on any tensor field $T^{\alpha\ldots\beta}_{\gamma\ldots\delta}$ in the Kerr background. This connection is given by [51]

$$\tilde{\nabla}_\nu T^{\alpha\ldots\beta}_{\gamma\ldots\delta} = \nabla_\nu T^{\alpha\ldots\beta}_{\gamma\ldots\delta} + C^\alpha_{\nu\mu} T^{\mu\ldots\beta}_{\gamma\ldots\delta} + \ldots + C^\beta_{\nu\mu} T^{\alpha\ldots\mu}_{\gamma\ldots\delta} - C^\mu_{\nu\gamma} T^{\alpha\ldots\beta}_{\mu\ldots\delta} - \ldots - C^\mu_{\nu\delta} T^{\alpha\ldots\beta}_{\gamma\ldots\mu}, \tag{B.2.1}$$

where $C^{\alpha}_{\mu\nu}$ is a tensor field in the Kerr background, symmetric in its two lower indices. This tensor field can be constructed in terms of $\tilde{g}_{\mu\nu}$ by exploiting the metric connection

$$\tilde{\nabla}_\rho \tilde{g}_{\mu\nu} = 0. \tag{B.2.2}$$

We state this connection three times:

$$\begin{aligned} \tilde{\nabla}_\rho \tilde{g}_{\mu\nu} &= \nabla_\rho \tilde{g}_{\mu\nu} - C^{\sigma}_{\rho\mu}\tilde{g}_{\sigma\nu} - C^{\sigma}_{\rho\nu}\tilde{g}_{\mu\sigma} = 0, \\ -\tilde{\nabla}_\mu \tilde{g}_{\nu\rho} &= -\nabla_\mu \tilde{g}_{\nu\rho} + C^{\sigma}_{\mu\nu}\tilde{g}_{\sigma\rho} + C^{\sigma}_{\mu\rho}\tilde{g}_{\nu\sigma} = 0, \\ -\tilde{\nabla}_\nu \tilde{g}_{\rho\mu} &= -\nabla_\nu \tilde{g}_{\rho\mu} + C^{\sigma}_{\nu\rho}\tilde{g}_{\sigma\mu} + C^{\sigma}_{\nu\mu}\tilde{g}_{\rho\sigma} = 0. \end{aligned} \tag{B.2.3}$$

By adding these equations and making use of the symmetric properties of $C^{\sigma}_{\mu\nu}$ and $\tilde{g}_{\mu\nu}$, we find

$$\nabla_\rho \tilde{g}_{\mu\nu} - \nabla_\mu \tilde{g}_{\nu\rho} - \nabla_\nu \tilde{g}_{\rho\mu} + 2C^{\sigma}_{\mu\nu}\tilde{g}_{\sigma\rho} = 0. \tag{B.2.4}$$

Now we multiply by the inverse metric $\tilde{g}^{\lambda\rho}$ and write for the tensor field

$$C^{\lambda}_{\mu\nu} = \frac{1}{2}\tilde{g}^{\lambda\rho}\left(\nabla_\mu \tilde{g}_{\nu\rho} + \nabla_\nu \tilde{g}_{\rho\mu} - \nabla_\rho \tilde{g}_{\mu\nu}\right). \tag{B.2.5}$$

To make sure that we only include first order terms in h, we write the metric according to Eq. (2.1.1). Additionally we use the metric connection in the background spacetime. We find

$$\begin{aligned} C^{\lambda}_{\mu\nu} &= \frac{1}{2}\left(g^{\lambda\rho} - h^{\lambda\rho}\right)\left(\nabla_\mu\left(g_{\nu\rho} + h_{\nu\rho}\right) + \nabla_\nu\left(g_{\rho\mu} + h_{\rho\mu}\right) - \nabla_\rho\left(g_{\mu\nu} + h_{\mu\nu}\right)\right) \\ &= \frac{1}{2}\left(g^{\lambda\rho} - h^{\lambda\rho}\right)\left(\nabla_\mu h_{\nu\rho} + \nabla_\nu h_{\rho\mu} - \nabla_\rho h_{\mu\nu}\right) \\ &= \frac{1}{2}g^{\lambda\rho}\left(\nabla_\mu h_{\nu\rho} + \nabla_\nu h_{\rho\mu} - \nabla_\rho h_{\mu\nu}\right) + \mathcal{O}(h^2). \end{aligned} \tag{B.2.6}$$

We will now proceed with the last part of the derivation, where we will need the connection coefficient to calculate $\tilde{\nabla}_\nu u^\mu$.

B.3 Acceleration derivation

The motion of the test mass in the total spacetime can be described by the geodesic equation [38]

$$\tilde{a}^\mu = \tilde{u}^\nu \tilde{\nabla}_\nu \tilde{u}^\mu = 0. \tag{B.3.1}$$

Here, $\tilde{u}^\mu = \frac{dx^\mu}{d\tilde{\tau}}$ is the four-velocity of the particle and $\tilde{\tau}$ is the proper time in the total spacetime. Notice that we use the same coordinates x^μ in the Kerr background and the actual spacetime. We can relate both proper times by writing out the line element

$$d\tilde{\tau}^2 = -\tilde{g}_{\mu\nu}dx^\mu dx^\nu \overset{2.1.1}{=} -\left(g_{\mu\nu} + h_{\mu\nu}\right)dx^\mu dx^\nu = d\tau^2 - h_{\mu\nu}dx^\mu dx^\nu. \tag{B.3.2}$$

We divide this expression by $d\tau^2$ and use the definition of the four-velocity to find

$$\left(\frac{d\tilde{\tau}}{d\tau}\right)^2 = 1 - h_{\mu\nu}u^\mu u^\nu. \tag{B.3.3}$$

Next, we take the square root and use a Taylor expansion to keep the lowest order terms only:

$$\frac{d\tilde{\tau}}{d\tau} = \sqrt{1 - h_{\mu\nu}u^\mu u^\nu} = 1 - \frac{1}{2}h_{\mu\nu}u^\mu u^\nu + \mathcal{O}(h^2). \tag{B.3.4}$$

The inverse of this expression is then given by [42]

$$\frac{d\tau}{d\tilde{\tau}} = 1 + \frac{1}{2}h_{\mu\nu}u^\mu u^\nu + \mathcal{O}(h^2). \tag{B.3.5}$$

This expression can be used to relate the four-velocity in the background and actual spacetime:

$$\tilde{u}^\mu = \frac{dx^\mu}{d\tilde{\tau}} = \frac{dx^\mu}{d\tau}\frac{d\tau}{d\tilde{\tau}} \overset{B.3.5}{=} (1 + \frac{1}{2}h_{\rho\sigma}u^\rho u^\sigma)u^\mu + \mathcal{O}(h^2). \tag{B.3.6}$$

Substituting this in Eq. (B.3.1) results in

$$0 = \tilde{u}^\nu \tilde{\nabla}_\nu \tilde{u}^\mu = (1 + \frac{1}{2}h_{\alpha\beta}u^\alpha u^\beta)u^\nu \tilde{\nabla}_\nu \left((1 + \frac{1}{2}h_{\rho\sigma}u^\rho u^\sigma)u^\mu\right) + \mathcal{O}(h^2). \tag{B.3.7}$$

As the multiplication by the first term of this expression will only lead to terms of higher order in h, we can neglect it. If we then expand, and write $\tilde{\nabla}_\nu$ in terms of ∇_ν using $C^\mu_{\nu\beta}$, we obtain

$$\begin{aligned}
0 &= u^\nu \tilde{\nabla}_\nu (u^\mu + \frac{1}{2}h_{\rho\sigma}u^\rho u^\sigma u^\mu) + \mathcal{O}(h^2) \\
&= u^\nu \tilde{\nabla}_\nu u^\mu + \frac{1}{2}u^\nu \tilde{\nabla}_\nu (h_{\rho\sigma}u^\rho u^\sigma u^\mu) + \mathcal{O}(h^2) \\
&\overset{B.2.1}{=} u^\nu \nabla_\nu u^\mu + u^\nu C^\mu_{\nu\beta}u^\beta + \frac{1}{2}u^\nu \nabla_\nu (h_{\rho\sigma}u^\rho u^\sigma u^\mu) + \mathcal{O}(h^2) \\
&\overset{B.2.6}{=} a^\mu + \frac{1}{2}g^{\mu\gamma}\left(\nabla_\nu h_{\beta\gamma} + \nabla_\beta h_{\gamma\nu} - \nabla_\gamma h_{\nu\beta}\right)u^\nu u^\beta \\
&\quad + \frac{1}{2}u^\nu(\nabla_\nu h_{\rho\sigma})u^\rho u^\sigma u^\mu + \frac{1}{2}h_{\rho\sigma}(a^\mu u^\rho u^\sigma + a^\rho u^\sigma u^\mu + a^\sigma u^\rho u^\mu) + \mathcal{O}(h^2).
\end{aligned} \tag{B.3.8}$$

Collecting terms proportional to a^μ gives

$$\begin{aligned}
\left(1 + \frac{1}{2}h_{\rho\sigma}u^\rho u^\sigma\right)a^\mu = &-\frac{1}{2}g^{\mu\gamma}\left(\nabla_\nu h_{\beta\gamma} + \nabla_\beta h_{\gamma\nu} - \nabla_\gamma h_{\nu\beta}\right)u^\nu u^\beta \\
&- \frac{1}{2}\left(u^\nu(\nabla_\nu h_{\rho\sigma})u^\rho u^\sigma + h_{\rho\sigma}a^\rho u^\sigma + h_{\rho\sigma}a^\sigma u^\rho\right)u^\mu + \mathcal{O}(h^2).
\end{aligned} \tag{B.3.9}$$

We will now a perform a normal projection by acting with $P_\mu{}^\alpha$ on both sides of Eq. (B.3.9). The left-hand side of the equation is evaluated using Eq. (B.1.5), as $P_\mu{}^\alpha$ only acts on a^μ. In addition, the term proportional to u^μ on the right-hand side of the equation vanishes because of Eq. (B.1.1). We use the definition of $P_\mu{}^\alpha$ to evaluate the remaining part of the right-hand side [46]:

$$\begin{aligned}
\left(1 + \frac{1}{2}h_{\rho\sigma}u^\rho u^\sigma\right)a^\alpha &= -\frac{1}{2}\left(\delta_\mu{}^\alpha + u_\mu u^\alpha\right)g^{\mu\gamma}\left(\nabla_\nu h_{\beta\gamma} + \nabla_\beta h_{\gamma\nu} - \nabla_\gamma h_{\nu\beta}\right)u^\nu u^\beta + \mathcal{O}(h^2) \\
&= -\frac{1}{2}\left(g^{\gamma\alpha} + u^\gamma u^\alpha\right)\left(\nabla_\nu h_{\beta\gamma} + \nabla_\beta h_{\gamma\nu} - \nabla_\gamma h_{\nu\beta}\right)u^\nu u^\beta + \mathcal{O}(h^2).
\end{aligned} \tag{B.3.10}$$

The expression on the right-hand side should not change when interchanging indices β and ν. Therefore we can rewrite the total equation as

$$\left(1 + \frac{1}{2}h_{\rho\sigma}u^\rho u^\sigma\right)a^\alpha = -\frac{1}{2}\left(g^{\gamma\alpha} + u^\gamma u^\alpha\right)\left(2\nabla_\nu h_{\beta\gamma} - \nabla_\gamma h_{\nu\beta}\right)u^\nu u^\beta + \mathcal{O}(h^2). \tag{B.3.11}$$

Lastly we divide by the prefactor of a^α, and make sure that we only keep terms of first order in h. This leaves us with the final expression of the induced acceleration, which is equivalent to Eq. (2.4.3):

$$\begin{aligned}
a^\alpha &= -\frac{1}{2}\left(1 - \frac{1}{2}h_{\rho\sigma}u^\rho u^\sigma\right)\left(g^{\gamma\alpha} + u^\gamma u^\alpha\right)\left(2\nabla_\nu h_{\beta\gamma} - \nabla_\gamma h_{\nu\beta}\right)u^\nu u^\beta + \mathcal{O}(h^2) \\
&= -\frac{1}{2}\left(g^{\gamma\alpha} + u^\gamma u^\alpha\right)\left(2\nabla_\nu h_{\beta\gamma} - \nabla_\gamma h_{\nu\beta}\right)u^\nu u^\beta + \mathcal{O}(h^2).
\end{aligned} \tag{B.3.12}$$

C Fitting formulas

Here we provide fitting formulas for several resonance combinations in both the stationary and the dynamic model. We also included the dependence on the perturber's inclination angle θ_y. Expressions for a perturber in the equatorial plane can be retrieved by substituting $\theta_y = 0$ in the formulas. The dependence on θ_z is not stated, as this can be incorporated in the total phase of the jump. In the stationary model we distinguish between fitting formulas determined from a Schwarzschild-like and a Kerr-like metric perturbation. The dynamic formulae are purely constructed from a Schwarzschild-like metric perturbation.

In both models, the fitting formulae are computed by making a polynomial ansatz of the type

$$\left\langle \frac{dC}{dt} \right\rangle \Big|_{nkm(s)} (a, e, x, \theta_y) = \frac{e^2}{(1-e)^2} \sum_{i=1}^{N_i} \sum_{j=1}^{N_j} \sum_{i=k}^{N_k} C_{ijk} a^i e^j x^k f_{m(s)}(\theta_y) \tag{C.0.1}$$

for $C \in \{L_z, Q\}$. We have included the prefactor $\frac{e^2}{(1-e)^2}$ to make sure that the amplitudes vanish for circular orbits, which have $e = 0$. In order to determine the coefficients C_{ijk}, we first calculated jump amplitudes using the semi-analytical averaging integrals. We did this for different values of a, e and x, thereby covering the whole parameter space. After that, we used Mathematica's fitting procedure to find the coefficients C_{ijk} for given fitting orders N_i, N_j and N_k.

C.1 Stationary - Schwarzschild

Fitting formulas for the (3,0,−2)-resonance, based on a Schwarzschild-like metric perturbation:

$$\begin{aligned}\left\langle \frac{dL_z}{dt} \right\rangle\Big|_{30-2}(a,e,x,\theta_y) = \frac{e^2}{(1-e)^2} i\Big(& e^4\big((-32.4381a^2+82.5474a-22.3164)x^2 \\ & +(23.2914a^2-4.02486a-44.3466)x+1.02527a^2-4.05997a-22.2394\big) \\ & +e^3\big((94.5972a^2-238.919a+64.6126)x^2+(-68.0359a^2+11.6784a+128.415)x \\ & -2.66177a^2+11.8194a+64.3835\big)+e^2\big((-118.506a^2+292.893a-76.3404)x^2 \\ & +(84.5264a^2-16.1104a-151.596)x+2.62407a^2-15.3716a-76.01\big) \\ & +e\big((73.9985a^2-184.069a+48.6963)x^2+(-53.0538a^2+9.83736a+96.7252)x \\ & -1.8061a^2+9.48732a+48.4976\big)+(0.330326a^2-0.836528a+0.231949)x^2 \\ & +(-0.241884a^2+0.0424229a+0.45964)x-0.0103485a^2+0.0410217a+0.230342\Big)\cos^2\theta_y,\end{aligned} \tag{C.1.1}$$

$$\begin{aligned}\left\langle \frac{dQ}{dt} \right\rangle\Big|_{30-2}(a,e,x,\theta_y) = \frac{e^2}{(1-e)^2} i\Big(& \\ & e^5\Big((-350.303a^2+324.523a+1.77058)x^6+(997.632a^2-962.616a-18.085)x^5+(-1269.95a^2 \\ & +1251.04a+33.1021)x^4+(743.425a^2-382.529a-160.802)x^3+(-79.7357a^2-106.556a \\ & -144.551)x^2+(-22.0552a^2-165.183a+146.082)x-19.0792a^2+41.3918a+142.472\Big) \\ & +e^4\Big((843.714a^2-794.492a-10.0955)x^6+(-2322.02a^2+2350.16a+65.9228)x^5+(3122.45a^2 \\ & -3261.7a-111.017)x^4+(-1908.19a^2+739.306a+574.263)x^3+(101.06a^2+534.05a \\ & +512.585)x^2+(95.4933a^2+579.224a-520.372)x+67.6492a^2-146.732a-511.26\Big) \\ & +e^3\Big((-738.9a^2+712.284a+16.7901)x^6+(1875.1a^2-2102.59a-87.933)x^5+(-2887.61a^2 \\ & +3356.97a+139.319)x^4+(1936.44a^2-271.834a-878.968)x^3+(89.9658a^2-1037.73a \\ & -793.9)x^2+(-173.713a^2-881.421a+806.62)x-101.436a^2+224.504a+798.045\Big) \\ & +e^2\Big((277.294a^2-281.465a-11.6054)x^6+(-516.262a^2+834.747a+52.9907)x^5+(1287.18a^2 \\ & -1862.11a-80.2363)x^4+(-1070.25a^2-330.574a+745.28)x^3+(-239.536a^2+1077.13a \\ & +691.434)x^2+(177.408a^2+769.623a-700.812)x+84.233a^2-207.437a-697.039\Big) \\ & +e\Big((-36.6328a^2+44.9437a+3.37486)x^6+(-67.0153a^2-138.552a-13.9053)x^5+(-318.61a^2 \\ & +686.771a+20.4644)x^4+(388.599a^2+362.577a-407.257)x^3+(184.938a^2-642.257a \\ & -391.75)x^2+(-103.5a^2-427.826a+394.944)x-47.7934a^2+114.36a+394.127\Big) \\ & +(3.09102a^2-3.12318a-0.177352)x^6+(-9.07793a^2+8.34304a+0.944115)x^5+(8.91102a^2 \\ & -7.04705a-1.56844)x^4+(-3.82138a^2+3.7586a+0.382147)x^3+(1.22257a^2-1.48748a \\ & -0.8553)x^2+(-0.246704a^2-0.590026a+0.629687)x-0.0777528a^2+0.144901a+0.645359\Big)\cos^2\theta_y.\end{aligned} \tag{C.1.2}$$

C.2 Stationary - Kerr

Fitting formulas for the (3,0,−2)-resonance, based on a Kerr-like metric perturbation:

$$\begin{aligned}\left\langle \frac{dL_z}{dt} \right\rangle\Big|_{30-2}(a,e,x,\theta_y) = \frac{e^2}{(1-e)^2} i\Big(& e^4\big((-32.3879a^2 + 82.4572a - 22.3083)x^2 \\ & + (23.2491a^2 - 3.91293a - 44.3636)x + 1.05349a^2 - 4.08057a - 22.2342\big) \\ & + e^3\big((94.5435a^2 - 238.924a + 64.6023)x^2 + (-67.659a^2 + 11.6636a + 128.444)x \\ & - 2.63326a^2 + 11.9476a + 64.3733\big) + e^2\big((-118.477a^2 + 293.127a - 76.34)x^2 \\ & + (83.7703a^2 - 16.3509a - 151.612)x + 2.47939a^2 - 15.5658a - 76.0033\big) \\ & + e\big((73.9756a^2 - 184.208a + 48.6983)x^2 + (-52.6398a^2 + 9.98161a + 96.7283)x \\ & - 1.71971a^2 + 9.5751a + 48.4959\big) + (0.332485a^2 - 0.839281a + 0.23218)x^2 \\ & + (-0.244123a^2 + 0.0464889a + 0.459004)x - 0.00890793a^2 + 0.0395971a + 0.230579\Big)\cos^2\theta_y,\end{aligned} \tag{C.2.1}$$

$$\begin{aligned}\left\langle \frac{dQ}{dt} \right\rangle\Big|_{30-2}(a,e,x,\theta_y) = \frac{e^2}{(1-e)^2} i\Big(& \\ a^2\Big(& e^5\big(3083.2x^6 - 10377.2x^5 + 13254.4x^4 - 8160.38x^3 + 2550.55x^2 - 340.144x - 10.0236\big) \\ & + e^4\big(-7897.46x^6 + 26642.3x^5 - 33870.9x^4 + 20776.6x^3 - 6603.63x^2 + 907.278x + 44.6096\big) \\ & + e^3\big(7582.19x^6 - 25708.9x^5 + 32360.5x^4 - 19691.2x^3 + 6486.1x^2 - 948.83x - 78.7503\big) \\ & + e^2\big(-3347.6x^6 + 11509.1x^5 - 14093.8x^4 + 8377.65x^3 - 3034.46x^2 + 515.645x + 73.0184\big) \\ & + e\big(660.341x^6 - 2381.86x^5 + 2646.78x^4 - 1436.27x^3 + 724.611x^2 - 168.486x - 45.0386\big) \\ & + \big(-40.6976x^6 + 136.458x^5 - 177.67x^4 + 111.188x^3 - 33.0864x^2 + 4.01312x - 0.210877\big)\Big) \\ & + a\Big(e^5\big(-4350.13x^6 + 14506.3x^5 - 18462.6x^4 + 11659.1x^3 - 3638.15x^2 + 253.231x + 31.5923\big) \\ & + e^4\big(11213.4x^6 - 37374.x^5 + 47344.x^4 - 30157.6x^3 + 9591.26x^2 - 493.825x - 121.648\big) \\ & + e^3\big(-10844.9x^6 + 36120.5x^5 - 45318.6x^4 + 29433.1x^3 - 9742.32x^2 + 150.089x + 200.56\big) \\ & + e^2\big(4825.77x^6 - 16051.3x^5 + 19631.5x^4 - 13439.8x^3 + 4917.2x^2 + 314.363x - 197.074\big) \\ & + e\big(-957.047x^6 + 3172.43x^5 - 3523.9x^4 + 2927.79x^3 - 1393.09x^2 - 338.697x + 112.382\big) \\ & + \big(61.8665x^6 - 205.98x^5 + 264.857x^4 - 161.429x^3 + 46.7357x^2 - 6.33306x + 0.291156\big)\Big) \\ & + e^5\big(1570.78x^6 - 5161.41x^5 + 6509.6x^4 - 4055.x^3 + 973.716x^2 + 17.1006x + 145.478\big) \\ & + e^4\big(-4090.14x^6 + 13427.x^5 - 16915.2x^4 + 10666.x^3 - 2383.42x^2 - 185.962x - 518.95\big) \\ & + e^3\big(4010.25x^6 - 13148.5x^5 + 16540.5x^4 - 10713.2x^3 + 2025.65x^2 + 480.624x + 805.395\big) \\ & + e^2\big(-1818.74x^6 + 5951.92x^5 - 7471.29x^4 + 5166.37x^3 - 574.014x^2 - 554.314x - 700.237\big) \\ & + e\big(370.741x^6 - 1209.15x^5 + 1512.11x^4 - 1295.51x^3 - 138.408x^2 + 365.572x + 394.711\big) \\ & + \big(-25.516x^6 + 82.8209x^5 - 102.871x^4 + 60.0994x^3 - 17.7144x^2 + 2.57959x + 0.597364\big)\Big)\cos^2\theta_y.\end{aligned} \tag{C.2.2}$$

C.3 Dynamic

Fitting formulas for the (3,0,−2,2)-resonance, based on a Schwarzschild-like metric perturbation:

$$\begin{aligned}\left\langle \frac{dL_z}{dt} \right\rangle\Big|_{30-22}(a,e,x,\theta_y) = \frac{e^2}{(1-e)^2} i\Big(& e^4\big((-16.4015a^2+39.1014a-9.85389)x^2 \\ & +(11.565a^2-2.55902a-19.6348)x-0.00519701a^2-2.06224a-9.86451\big) \\ & +e^3\big((34.7861a^2-85.3948a+22.1898)x^2+(-24.9081a^2+5.18503a+44.1958)x \\ & -0.262398a^2+4.37238a+22.1933\big)+e^2\big((-34.8772a^2+85.7044a-22.0524)x^2 \\ & +(24.9507a^2-5.16425a-43.8988)x+0.447507a^2-4.52774a-22.0319\big) \\ & +e\big((18.978a^2-47.5157a+12.5594)x^2+(-13.707a^2+2.64862a+25.0004)x \\ & -0.416963a^2+2.44956a+12.5418\big)+(-0.00488119a^2-0.00919803a+0.0108231)x^2 \\ & +(0.0005391a^2-0.005918a+0.021342)x-0.005835a^2-0.0006785a+0.010522\Big)(\cos\theta_y+1)^2\,,\end{aligned} \tag{C.3.1}$$

$$\begin{aligned}\left\langle \frac{dQ}{dt} \right\rangle\Big|_{30-22}(a,e,x,\theta_y) = \frac{e^2}{(1-e)^2} i\Big(& \\ & e^4\Big((125.038a^2-323.6a+81.1229)x^3+(-191.742a^2+290.59a+83.6807)x^2 \\ & +(59.452a^2+58.9459a-82.6308)x+6.30343a^2-25.2159a-82.1798\Big) \\ & +e^3\Big((-266.124a^2+696.596a-178.542)x^3+(408.834a^2-623.497a-182.975)x^2 \\ & +(-125.694a^2-126.189a+181.175)x-15.0454a^2+51.5777a+180.354\Big) \\ & +e^2\Big((265.063a^2-678.982a+171.067)x^3+(-407.045a^2+611.924a+173.717)x^2 \\ & +(125.059a^2+118.511a-172.66)x+15.0869a^2-50.063a-172.131\Big) \\ & +e\Big((-148.565a^2+378.531a-96.8481)x^3+(228.373a^2-341.196a-97.5503)x^2 \\ & +(-69.4165a^2-64.6291a+97.2706)x-9.42566a^2+26.5603a+97.1285\Big) \\ & +(-0.117927a^2+0.101404a-0.0479041)x^3+(0.188465a^2-0.132458a-0.0138666)x^2 \\ & +(-0.040434a^2+0.068733a+0.027430)x-0.03226a^2-0.035929a+0.034214\Big)(\cos\theta_y+1)^2\,.\end{aligned} \tag{C.3.2}$$

D Selection rules

In this appendix we will derive the so-called selection rules. These rules state that a jump in the orbital constants of motion due to a tidal resonance can only occur for certain combinations of the resonant integers k, m and s. We will first derive these selection rules in the stationary model, where the perturber can be situated both on and off the equatorial plane. Lastly, we will derive the most general selection rule in the dynamic model, where the perturber moves in a circular orbit that is inclined with respect to the equatorial plane.

D.1 Stationary perturber on the equatorial plane

We will show that the tidally induced jump sizes in L_z and Q do not change under a reflection of the orbit in the equatorial plane. Therefore we rewrite the induced acceleration of Eq. (2.4.3) as

$$\begin{aligned} a_\alpha &= \left(g_\alpha{}^\beta + u_\alpha u^\beta\right) u^\lambda u^\rho \left(-\nabla_\rho h_{\beta\lambda} + \frac{1}{2}\nabla_\beta h_{\lambda\rho}\right) + \mathcal{O}(h^2) \\ &= u^\lambda u^\rho \left(-\nabla_\rho h_{\alpha\lambda} + \frac{1}{2}\nabla_\alpha h_{\lambda\rho}\right) + u_\alpha \left(-\underbrace{u^\beta u^\lambda u^\rho \nabla_\rho h_{\beta\lambda}}_{\beta\rightleftarrows\rho} + \frac{1}{2}u^\beta u^\lambda u^\rho \nabla_\beta h_{\lambda\rho}\right) + \mathcal{O}(h^2) \\ &= u^\lambda u^\rho \left(-\underbrace{\nabla_\rho h_{\alpha\lambda}}_{1} + \underbrace{\frac{1}{2}\nabla_\alpha h_{\lambda\rho}}_{2} - \underbrace{\frac{1}{2}u_\alpha u^\beta \nabla_\beta h_{\lambda\rho}}_{3}\right) + \mathcal{O}(h^2). \end{aligned} \tag{D.1.1}$$

We will now perform a reflection in the equatorial plane on all three terms as marked above. This will give us the full reflection of the induced acceleration. Under a reflection in the equatorial plane, the polar coordinate is shifted according to $\theta \to \pi - \theta$. Consequently, we have

- $u^\theta \to -u^\theta$,
- $\nabla_\theta \to -\nabla_\theta$,
- $q_\theta \to \pi - q_\theta$,

while all other quantities remain unchanged. We will now first focus on the rate of change in L_z, which is given by a_ϕ according to Eq. (2.4.4a). Therefore we take $\alpha = \phi$ in Eq. (D.1.1), and subsequently perform a reflection in the equatorial plane on each of the three terms individually. We find:

1. $\underline{u^\lambda u^\rho \nabla_\rho h_{\phi\lambda}}$: As $h_{\mu\nu}$ is diagonal, we must have $\lambda = \phi$ for a nonzero metric perturbation. If we perform a reflection, there only occur changes if $\rho = \theta$: $u^\phi u^\theta \nabla_\theta h_{\phi\phi} \to u^\phi(-u^\theta)(-\nabla_\theta)h_{\phi\phi} = u^\phi u^\theta \nabla_\theta h_{\phi\phi}$. As a result, this term does not change under a reflection in the equatorial plane.

2. $\underline{u^\lambda u^\rho \nabla_\phi h_{\lambda\rho}}$: We must have $\lambda = \rho$, as $h_{\mu\nu}$ is diagonal, so this term now looks like $u^\lambda u^\lambda \nabla_\phi h_{\lambda\lambda}$. Under a reflection, only changes occur if $\lambda = \theta$. We find: $u^\theta u^\theta \nabla_\phi h_{\theta\theta} \to (-u^\theta)(-u^\theta)\nabla_\phi h_{\theta\theta} = u^\theta u^\theta \nabla_\phi h_{\theta\theta}$. We notice that this term is not altered either.

3. $\underline{u^\lambda u^\rho u_\phi u^\beta \nabla_\beta h_{\lambda\rho}}$: Again, we must have $\lambda = \rho$ for a nonzero contribution of the metric perturbation. Changes under a reflection then occur if $\lambda = \theta$ or $\beta = \theta$. If $\lambda/\beta = \theta$, then you always get a double minus sign change under a reflection, irrespective of the index β/λ. Hence, this third term is also conserved under a reflection in the equatorial plane.

As a result, we find that the ϕ-component of the induced acceleration does not change under a reflection in the equatorial plane:

$$a_\phi(t, r, \theta, \phi) = a_\phi(t, r, \pi - \theta, \phi) \tag{D.1.2}$$

If we now perform a Fourier decomposition of the acceleration for the polar coordinate only, we can write Eq. (D.1.2) as

$$\begin{aligned}\sum_k a_{\phi,k}(t, r, \phi) e^{ikq_\theta} &= \sum_k a_{\phi,k}(t, r, \phi) e^{ik(\pi - q_\theta)} \\ &= \sum_k (-1)^k a_{\phi,k}(t, r, \phi) e^{-ikq_\theta} \\ &= \sum_k (-1)^k a_{\phi,k}(t, r, \phi) e^{ikq_\theta}.\end{aligned} \tag{D.1.3}$$

In the last step we could omit the minus sign in the exponential, as we sum over all possible $k \in \mathbb{Z}$. This k is the exact same k as used in the Fourier composition of the tidal force in Eq. (2.3.7), as it corresponds to the angle q_θ. Both the left- and right-hand side of Eq. (D.1.3) should be equivalent according to Eq. (D.1.2). This is only true if the coefficients $a_{\phi,k}$ are nonzero when

$$k = \text{even}. \tag{D.1.4}$$

This means that only terms with $k =$ even contribute to the induced acceleration in the azimuthal direction. Since $\frac{dL_z}{d\tau} = a_\phi$, the same reasoning applies to the rate of change in L_z, meaning that tidal resonances with $k =$ odd do not contribute to a change in L_z if the perturber is situated on the equatorial plane. According to the two-for-one deal in Eq. (2.4.20), the rate of change in Q can be determined from the rate of change in L_z, meaning that we also do not encounter a jump in Q for resonances with $k =$ odd. We refer to the statement in Eq. (D.1.4) as our first selection rule. An equivalent selection rule was also found in [45].

D.2 Stationary perturber off the equatorial plane

We will now consider the scenario where the tidal perturber has an arbitrary sky location, as discussed in section 3.2.4. As we have seen, this allows the manifestation of resonances with $m = \pm 1$, which in turn requests for an update of the first selection rule. To find this new selection rule, we first study the influence of the m-modes on the tidal potentials under the reflection $\theta \to \pi - \theta$. We find that we can rewrite the stationary electric tidal quadrupole potential as

$$\begin{aligned}\mathcal{E}^{\mathrm{q}}(0, \theta, \phi) &= \sum_{-2 \le m \le 2} \mathcal{E}^{\mathrm{q}}_m(0) Y^{2m}(\theta, \phi) \\ &= \sum_{-2 \le m \le 2} (-1)^m \mathcal{E}^{\mathrm{q}}_m(0) Y^{2m}(\pi - \theta, \phi).\end{aligned} \tag{D.2.1}$$

The stationary metric perturbation is linear in this potential. Consequently, the stationary metric perturbation can also be written as

$$\begin{aligned}h_{\mu\nu}(0, r, \theta, \phi) &= f^{\mathrm{el}}_{\mu\nu}(r) \mathcal{E}^{\mathrm{q}}(0, \theta, \phi) \\ &= f^{\mathrm{el}}_{\mu\nu}(r) \sum_{-2 \le m \le 2} (-1)^m \mathcal{E}^{\mathrm{q}}_m(0) Y^{2m}(\pi - \theta, \phi).\end{aligned} \tag{D.2.2}$$

Here we used Eq. (D.2.1) in the second line, and we denoted the electric radial functions of Tab. 3 by $f^{\mathrm{el}}_{\mu\nu}(r)$. We now use this form of the stationary metric perturbation as input for the tidally induced acceleration as given in Eq. (D.1.1). Under the reflection $\theta \to \pi - \theta$, Eq. (D.1.2) still

holds. This may not seem evident, since this operation corresponds to a reflection in the equatorial plane, where the perturber is not residing. However, the functional dependence on the perturber's inclination angle θ_y, as given by the function $f_m(\theta_y)$ in Tab. 4, is just a multiplicative factor in the jump's amplitudes, as can be seen in Eq. (3.2.5). Consequently, the tidal force has to be multiplied by the functions $f_m(\theta_y)$ as well, which means that they can be scaled out of Eq. (D.1.2). We will now decompose the induced acceleration in its Fourier modes again. Besides the polar mode, we also decompose in the mode corresponding to the azimuthal motion, because of the oscillating dependence on m in the tidal potential. Analogous to Eq. (D.1.3) we find

$$\begin{aligned}\sum_{k,m} a_{\phi,km}(0,r)e^{ikq_\theta}e^{imq_\phi} &= \sum_{k,m}(-1)^m a_{\phi,km}(0,r)e^{ik(\pi-q_\theta)}e^{imq_\phi}\\ &= \sum_{k,m}(-1)^{k+m} a_{\phi,km}(0,r)e^{-ikq_\theta}e^{imq_\phi}\\ &= \sum_{k,m}(-1)^{k+m} a_{\phi,km}(0,r)e^{ikq_\theta}e^{imq_\phi}.\end{aligned} \tag{D.2.3}$$

Both sides of this equation are only equivalent when

$$k+m = \text{even}. \tag{D.2.4}$$

We refer to this statement as the second selection rule. From the definition of the rate of change in L_z in Eq. (2.4.4a), we conclude that there is no jump induced in L_z for tidal resonances with $k+m =$ odd. This also means that we do not find a jump in Q, based on the two-for-one deal in Eq. (2.4.20). In principle, the analysis of this subsection is also valid for a perturber on the equatorial plane, meaning that the second selection rule of Eq. (D.2.4) applies to this case as well. However, as we only found resonances with $m \in \{-2,0,2\}$ in this case, this selection rule is equivalent to the first selection rule of Eq. (D.1.4).

D.3 Dynamic perturber off the equatorial plane

We need a new selection rule in the case of a dynamic tidal perturber, since the dynamic tidal resonance condition in Eq. (2.3.15) also contains an s-mode. To find this rule, we will first focus on the electric quadrupole potential. In the stationary model, the harmonic components $\mathcal{E}^{\mathrm{q}}_m(0)$ in Eq. (D.2.1) are constant. In the dynamic model, on the other hand, the harmonic components $\mathcal{E}^{\mathrm{q}}_m(t)$ determine the perturber's dynamics. So to derive a dynamic selection rule, we have to study these components under a reflection in the equatorial plane. Therefore we notice that we can write the harmonic components as

$$\mathcal{E}^{\mathrm{q}}_m(t) = \sum_{-2\leq s\leq 2} \mathcal{E}^{\mathrm{q}}_{ms} Y^{2s}(\pi/4, Q_\phi), \tag{D.3.1}$$

where $\mathcal{E}^{\mathrm{q}}_{ms}$ are constant coefficients. The angle Q_ϕ determines the motion of the perturber, and is given by $Q_\phi = \Omega_\phi t$. We chose a value of $\theta = \frac{\pi}{4}$ in the spherical harmonic functions. In principle, we could have chosen any value of $\theta \in [0,\pi]$, as long as $Y^{2s}(\theta, Q_\phi) \neq 0 \ \ \forall s \in \{-2,-1,0,1,2\}$. This would only change the values of the coefficients $\mathcal{E}^{\mathrm{q}}_{ms}$. We notice that $Y^{20}(\theta, Q_\phi)$ and $Y^{2\pm2}(\theta, Q_\phi)$ are symmetric in $\theta = \frac{\pi}{2}$, while $Y^{2\pm1}(\theta, Q_\phi) = -Y^{2\pm1}(\pi-\theta, Q_\phi)$. Hence, we can write the dynamic harmonic components as

$$\begin{aligned}\mathcal{E}^{\mathrm{q}}_m(t) &= \sum_{-2\leq s\leq 2} \mathcal{E}^{\mathrm{q}}_{ms} Y^{2s}(\pi/4, Q_\phi)\\ &= \sum_{-2\leq s\leq 2} (-1)^s \mathcal{E}^{\mathrm{q}}_{ms} Y^{2s}(3\pi/4, Q_\phi).\end{aligned} \tag{D.3.2}$$

Now, similar to the stationary case, we can rewrite the electric tidal quadrupole potential as

$$\begin{aligned}\mathcal{E}^{\mathrm{q}}(t,\theta,\phi) &= \sum_{-2\leq m\leq 2} \mathcal{E}^{\mathrm{q}}_m(t) Y^{2m}(\theta,\phi) \\ &= \sum_{-2\leq m,s\leq 2} \Big(\mathcal{E}^{\mathrm{q}}_{ms} Y^{2s}(\pi/4, Q_\phi)\Big) Y^{2m}(\theta,\phi) \\ &= \sum_{-2\leq m,s\leq 2} (-1)^m \Big((-1)^s \mathcal{E}^{\mathrm{q}}_{ms} Y^{2s}(3\pi/4, Q_\phi)\Big) Y^{2m}(\pi-\theta,\phi).\end{aligned} \tag{D.3.3}$$

In the dynamic model, we also need the magnetic quadrupole potentials. Using a similar analysis, we find

$$\begin{aligned}\mathcal{B}^{\mathrm{q}}_\theta(t,\theta,\phi) &= \frac{1}{2} \sum_{-2\leq m\leq 2} \mathcal{B}^{\mathrm{q}}_m(t) X^{2m}_\theta(\theta,\phi) \\ &= \frac{1}{2} \sum_{-2\leq m,s\leq 2} \Big(\mathcal{B}^{\mathrm{q}}_{ms} Y^{2s}(\pi/4, Q_\phi)\Big) X^{2m}_\theta(\theta,\phi) \\ &= \frac{1}{2} \sum_{-2\leq m,s\leq 2} (-1)^m \Big((-1)^s \mathcal{B}^{\mathrm{q}}_{ms} Y^{2s}(3\pi/4, Q_\phi)\Big) X^{2m}_\theta(\pi-\theta,\phi),\end{aligned} \tag{D.3.4}$$

and

$$\begin{aligned}\mathcal{B}^{\mathrm{q}}_\phi(t,\theta,\phi) &= \frac{1}{2} \sum_{-2\leq m\leq 2} \mathcal{B}^{\mathrm{q}}_m(t) X^{2m}_\phi(\theta,\phi) \\ &= \frac{1}{2} \sum_{-2\leq m,s\leq 2} \Big(\mathcal{B}^{\mathrm{q}}_{ms} X^{2s}_\phi(\pi/6, Q_\phi)\Big) X^{2m}_\phi(\theta,\phi) \\ &= \frac{1}{2} \sum_{-2\leq m,s\leq 2} (-1)^m \Big((-1)^s \mathcal{B}^{\mathrm{q}}_{ms} X^{2s}_\phi(5\pi/6, Q_\phi)\Big) X^{2m}_\phi(\pi-\theta,\phi).\end{aligned} \tag{D.3.5}$$

Similar to the stationary case, this behaviour under the reflection $\theta \to \pi - \theta$ translates directly to the metric perturbation, since $h_{\mu\nu}$ is linear in the potentials. If we then write out the acceleration on both sides of Eq. (D.1.2) in terms of Fourier components, we find

$$\begin{aligned}\sum_{k,m,s} a_{\phi,kms}(r) e^{ikq_\theta} e^{imq_\phi} e^{isQ_\phi} &= \sum_{k,m,s} (-1)^m (-1)^s a_{\phi,kms}(r) e^{ik(\pi-q_\theta)} e^{imq_\phi} e^{isQ_\phi} \\ &= \sum_{k,m,s} (-1)^{k+m+s} a_{\phi,kms}(r) e^{-ikq_\theta} e^{imq_\phi} e^{isQ_\phi} \\ &= \sum_{k,m,s} (-1)^{k+m+s} a_{\phi,kms}(r) e^{ikq_\theta} e^{imq_\phi} e^{isQ_\phi}.\end{aligned} \tag{D.3.6}$$

Both sides of this equation are then only equal when

$$k + m + s = \text{even}, \tag{D.3.7}$$

which we refer to as the third selection rule. This rule also agrees with an equivalent rule from [45]. So, no jumps in L_z and Q are induced for tidal resonances with $k+m+s = \text{odd}$. Eq. (D.3.7) applies at all times, since it reduces to Eq. (D.2.4) in the case of a stationary perturber, and to Eq. (D.1.4) for a perturber on the equatorial plane. Therefore, it is the most general selection rule.